AD-A041 212 SHARED APPLICATIONS INC ANN ARBOR MICH F/G 9/1
RADIAL BEAM TWT ELECTRON BEAM ANALYSIS.(U)
MAY 77 K CHANG, J E ROWE DAAB07-76-C-1360
UNCLASSIFIED ECOM-76-1360-F NL

1 OF 2
AD
A041212

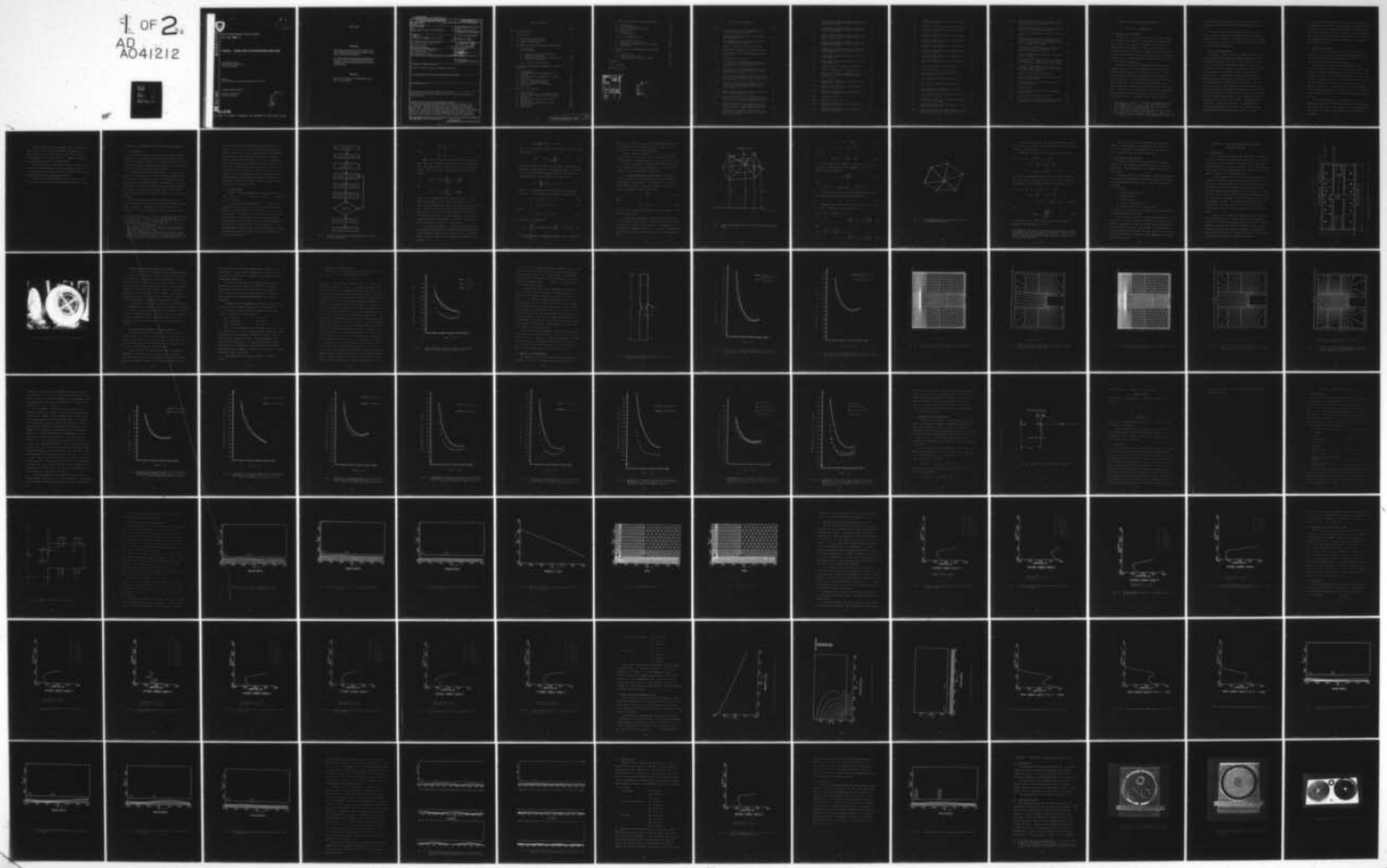

AD A041212

DDC FILE COPY

Research and Development Technical Report
ECOM – 76 - 1360 - F

RADIAL – BEAM TWT ELECTRON BEAM ANALYSIS

K. Chang and J. E. Rowe
SHARED APPLICATIONS, INC.
Ann Arbor, MI 48104

May 1977
FINAL REPORT for the period 30 April 1976 to 11 April 1977

DISTRIBUTION STATEMENT

Approved for public release;
distribution unlimited.

D D C
JUL 6 1977
D

ECOM
US ARMY ELECTRONICS COMMAND FORT MONMOUTH, NEW JERSEY 07703

NOTICES

Disclaimers

The findings in this report are not to be construed as an official Department of the Army position, unless so designated by other authorized documents.

The citation of trade names and names of manufacturers in this report is not to be construed as official Government indorsement or approval of commercial products or services referenced herein.

Disposition

Destroy this report when it is no longer needed. Do not return it to the originator.

UNCLASSIFIED

SECURITY CLASSIFICATION OF THIS PAGE (When Data Entered)

REPORT DOCUMENTATION PAGE

READ INSTRUCTIONS BEFORE COMPLETING FORM

1. REPORT NUMBER: ECOM-76-1360-F	2. GOVT ACCESSION NO.
3. RECIPIENT'S CATALOG NUMBER	
4. TITLE (and Subtitle): Radial Beam TWT Electron Beam Analysis.	5. TYPE OF REPORT & PERIOD COVERED: Final rept. 30 Apr 76 — 11 Apr 77
	6. PERFORMING ORG. REPORT NUMBER
7. AUTHOR(s): Dr. Kai Chang and Dr. Joseph E. Rowe	8. CONTRACT OR GRANT NUMBER(s): DAAB07-76-C-1360 New
9. PERFORMING ORGANIZATION NAME AND ADDRESS: Shared Applications, Inc. 611 Church Street Ann Arbor, MI 48104	10. PROGRAM ELEMENT, PROJECT, TASK AREA & WORK UNIT NUMBERS: DA Project No. 1L7 62705 AH 94 B1 11
11. CONTROLLING OFFICE NAME AND ADDRESS: US Army Electronics Command ATTN: DRSEL-TL-BM Fort Monmouth, NJ 07703	12. REPORT DATE: May 1977
	13. NUMBER OF PAGES: 120 p.
14. MONITORING AGENCY NAME & ADDRESS (if different from Controlling Office)	15. SECURITY CLASS. (of this report): Unclassified
	15a. DECLASSIFICATION/DOWNGRADING SCHEDULE

16. DISTRIBUTION STATEMENT (of this Report)

Approved for public release; distribution unlimited.

17. DISTRIBUTION STATEMENT (of the abstract entered in Block 20, if different from Report)

18. SUPPLEMENTARY NOTES

19. KEY WORDS (Continue on reverse side if necessary and identify by block number)

Traveling-wave tube, Radial electron beam, Radial beam traveling-wave tube computer analysis.

20. ABSTRACT (Continue on reverse side if necessary and identify by block number)

This study developed practical designs for prototype versions of an electromagnetic focusing structure and a radial beam traveling-wave tube electron gun. Computer simulations were used to develop both the electromagnetic focusing structure design and the electron gun design. A final design with a well focused beam has been recommended and an experimental tube for operation in the frequency range 500-1000 MHz has been built. The limited contract period did not allow time to carry out a successful experiment.

DD FORM 1 JAN 73 1473 EDITION OF 1 NOV 65 IS OBSOLETE

UNCLASSIFIED

SECURITY CLASSIFICATION OF THIS PAGE (When Data Entered)

406846

TABLE OF CONTENTS

		Page
LIST OF ILLUSTRATIONS		v
I.	INTRODUCTION	1
	A. Statement of the Problem	1
	B. Topics of Investigation	2
	C. Report Organization	3
II.	DEFORMABLE MESH ELECTRON GUN DESIGN PROGRAM	5
	A. Introduction	5
	B. General Method	6
	1. Generation of Deformable Mesh	6
	2. Potential Solution	8
	3. Cathode Current Density Calculations	10
	4. Trajectory Equations	10
	C. Description of the Program	15
III.	DESIGN AND FABRICATION OF MAGNETIC FOCUSING STRUCTURE	16
	A. Introduction	16
	B. Deformable Mesh Electromagnet Design Program	19
	C. Fabrication of the Magnetic Focusing Structure	19
	D. Shaping the Magnetic Fields	21
	E. Magnetic Field Measurements	23
	F. Cathode Curvature Calculation	41
	G. Conclusions	43
IV.	DESIGN OF ELECTRON GUN	45
	A. Introduction	45
	B. Beam-Filling Factor and Cathode Shape	47
	C. Voltage and Position of the Focusing Electrode	54
	D. Voltage and Position of the Anode	59
	E. Gun Design I	59
	F. Beam Focusing and Magnetic Field	66
	G. Gun Design II	80
	H. Conclusions	82

PRECEDING PAGE BLANK-NOT FILMED

V. FABRICATION OF RADIAL-BEAM ELECTRON GUN 84

A. Introduction 84
B. Cathode and Heater 84
C. Focusing Electrode and Anode 92
D. Ceramic Plates 94
E. Collector 95
F. Vacuum Chamber 97

VI. TEST OF EXPERIMENTAL TUBE 100

A. Experimental Setup 100
B. Discussion of the Problems 101
C. Recommended Solutions to the Problems 101
D. Conclusions 104

VII. CONCLUSIONS AND RECOMMENDATIONS FOR FUTURE STUDY 106

A. Introduction 106
B. Summary of this Study 106
C. Recommendations for Future Study 107

REFERENCES 108

LIST OF SYMBOLS 110

DISTRIBUTION LIST 113

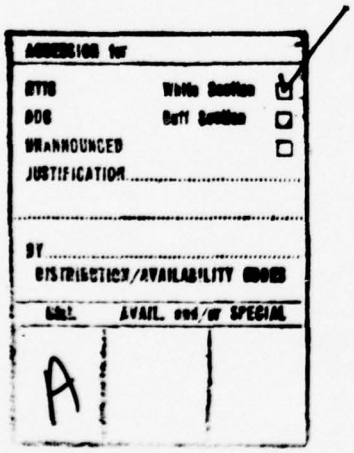

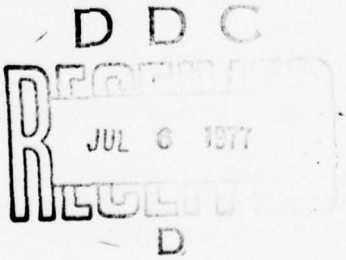

LIST OF ILLUSTRATIONS

Figure		Page
1	General Flow Chart for Deformable Mesh Electron Gun Design Program	7
2	Typical Mesh Node and Its Six Neighbors and Dodecagon Area	11
3	Mesh Node Nearest an Electron P and Its Six Neighboring Mesh Points	13
4a	Magnetic Focusing Structure of RBTWT	17
4b	Photograph of Magnetic Focusing Structure	18
5	Ideal Magnetic Field and Computed Magnetic Fields	22
6	Shaped Center Pole Piece	24
7a	The Effect of a Shaped Center Pole Piece with Current Levels at the Three Sections of Coil at 3.4 A, 3.8 A, 2.7 A	25
7b	The Effect of a Shaped Center Pole Piece with Current Levels at the Three Sections of Coil at 2.1 A, 2.1 A, 2.1 A	26
8a	Mesh Plot for a Magnetic Focusing Structure with an Unshaped Center Pole Piece and Coil Current Levels of 2.1 A, 2.1 A, 2.1 A	27
8b	Magnetic Flux Plot for a Magnetic Focusing Structure with an Unshaped Center Pole Piece and Coil Current Levels of 2.1 A, 2.1 A, 2.1 A	28
9a	Mesh Plot for a Magnetic Focusing Structure with a Shaped Center Pole Piece	29
9b	Magnetic Flux Plot for Current Levels of 1.7 A, 1.9 A, 1.35 A for a Magnetic Focusing Structure with a Shaped Center Pole Piece	30
9c	Magnetic Flux Plot for Current Levels of 3.4 A, 3.8 A, 0 A for a Magnetic Focusing Structure with a Shaped Center Pole Piece	31
10	Comparison of Computer Results with Experimental Measurements for Current Levels of 1.7 A, 1.9 A, 1.35 A	33

11	Comparison of Computer Results with Experimental Measurements for Current Levels of 2.9 A, 3.8 A, 0 A	34
12	Comparison of Computer Results with Experimental Measurements for Current Levels of 2.1 A, 2.1 A, 2.1 A	35
13	Comparison of Computer Results with Experimental Measurements for Current Levels of 2.9 A, 3.8 A, 2.1 A	36
14	Comparison of Computer Results with Experimental Measurements for Current Levels of 3.4 A, 3.8 A, 2.7 A	37
15	Comparison of Computer Results with Experimental Measurements for Current Levels of 5 A, 6 A, 2 A	38
16	Measurements for Center Pole Pieces of Different Materials	39
17	Measurements for Center Pole Pieces of Different Materials	40
18	Cathode Radius of Curvature Calculation	42
19	Geometric Parameters of Electron Gun	46
20	Trajectories Plot for a Cathode with Height h_c = 0.040 in., Radius of Curvature = 0.1 in.	48
21	Trajectories Plot for a Flat Cathode with Height = h_c = 0.040 in.	49
22	Trajectories Plot for a Flat Cathode of Height h_c = 0.025 in.	50
23	Magnetic Field Used for the Calculations in Figs. 20 through 22	51
24a	Mesh Plot of Fig. 20	52
24b	Mesh Plot of Fig. 22	53
25	Cathode Current Density as a Function of Z for d_1 = 0.01 in.	55
26	Cathode Current Density as a Function of Z for d_1 = 0.0075 in.	56

27	Cathode Current Density as a Function of Z for d_1 = 0 in.	57
28	Cathode Current Density as a Function of Z	58
29	Cathode Current Density as a Function of Z for V_e = 50 V	60
30	Cathode Current Density as a Function of Z for V_e = -50 V	61
31	Cathode Current Density as a Function of Z for d_2 = 0.1 in.	62
32	Cathode Current Density as a Function of Z for d_2 = 0.16 in.	63
33	Cathode Current Density as a Function of Z for V_a = 900 V	64
34	Cathode Current Density as a Function of Z for V_a = 1,100 V	65
35	Ideal RBTWT Magnetic Field as a Function of R	67
36	Equipotential Plot for Gun Design I	68
37	Trajectories Plot for Gun Design I	69
38	Cross-Section Beam Current Density at R = 1.05 in.	70
39	Cross-Section Beam Current Density at R = 1.1 in.	71
40	Cross-Section Beam Current Density at R = 1.2 in.	72
41	Beam Trajectories Plot with No Magnetic Field Applied to the Gun	73
42	Beam Trajectories Plot with Magnetic Field of 500 G at Cathode	74
43	Beam Trajectories Plot with Magnetic Field of 1,000 G at Cathode	75
44	Beam Trajectories Plot with Magnetic Field of 2,000 G at Cathode	76
45a	Beam Trajectories Plot for a Magnetic Field with Current Levels in Three Sections of Coil as 1.7 A, 1.9 A, 1.35 A	78

45b	Beam Trajectories Plot for a Magnetic Field with Current Levels in Three Sections of Coil as 3.4 A, 3.8 A, 2.7 A	79
46	Cathode Current Density as a Function of Z for a Strip Electrode and Anode	81
47	Trajectories Plot for a Strip Electrode and Anode	83
48	Photograph of a Cathode with Heater, Two Inner Ceramic Rings and a Four-Segment Collector. Each Ceramic Ring Contains a Focusing Electrode and an Anode	85
49	Ceramic Plate with One Surface Coated with a Conducting Layer to Simulate the Dc Effects of Spiral RF Circuit	86
50	Two Disk-Shaped Aluminum Pieces for Vacuum Chamber Assembly	87
51	View of Electron Gun with All Its Components in Alignment. A Symmetrical Ceramic Plate Will Rest on Top the Collector and Cathode	88
52	Assembled Vacuum Chamber Containing Electron Gun. Also Shown Are the Feedthroughs and the Heater Lead Posts	89
53	Cathode, Heater and Ceramic Rings	91
54	Sketch of Heater Showing Two Tungsten Wires Connected in Parallel	93
55	Cross Section of a Collector Ring Inside the Ceramic Plates	96
56	Vacuum Chamber	98
57	Electrical Configuration for Experimental Measurements	102
58	Photograph of Experimental Setup	103
59	Grooves in the Ceramic Disks Between Anode and Cathode to Mask Nickel Deposition	105

RADIAL-BEAM TWT ELECTRON BEAM ANALYSIS

SECTION I. INTRODUCTION

A. Statement of the Problem

Although it is still in the research stage, the radial-beam traveling-wave tube amplifier (RBTWT) has shown considerable promise as a compact, broadband, low voltage and high-gain microwave amplifier. The particular geometry of this device makes it possible to draw high current from the cathode at low cathode current density and to use the printed circuit type of slow-wave circuit to reduce the overall cost in even limited production.

Analytical studies of the RF behavior have been published assuming small-signal conditions by Savel'yev and Kushenko,[1] Molyavko et al.,[2] and Putz and Scott.[3] A large-signal computer simulation program has been developed by Kooyers and Shaw.[4] The experimental tube built by Savel'yev and Kushenko[1] has a low power output of 50-100 mW. The Varian tubes built by Putz and Scott[3] operated at much higher power. However, low beam transmission and oscillation problems prevented them from being able to operate the tubes at high current levels. Furthermore, the computer analyses

---

1. V. S. Savel'yev and G. I. Kushenko, Radio Eng. and Electronic Phys., vol. 15, No. 12, pp. 2267-2272; 1970.
2. V. I. Molyavko, et al., Radio Eng. and Electronic Phys. vol. 16, No. 8, pp. 1330-1335; 1971.
3. J. L. Putz and A. W. Scott, Report ECOM 73-0148-F, U.S. Army Electronics Command, Fort Monmouth, NJ; Sept. 1974.
4. G. P. Kooyers and E. K. Shaw, Final Report ECOM 74-0377-F, U.S. Army Electronics Command, Fort Monmouth, NJ; Nov. 1975.

used in these studies did not utilize the most up-to-date techniques available and so dielectric boundaries were neglected.

In order to avoid costly experiments later, there is a clear need to develop an electron gun analysis program to facilitate the design of a reliable electron gun and magnetic focusing structure. The study presented in this report is directed to that objective.

B. Topics of Investigation

The purpose of this study is to formulate designs for an electron gun and a companion magnetic focusing structure. A computer program has been utilized to solve for the magnetic field strength throughout the magnetic focusing structure. With this program, the required magnetic field can be shaped by varying the currents in sectionalized focusing coils. The magnetic field calculated is then confirmed by direct measurement and supplied as input to the Deformable Mesh Electron Gun Design Program. By the aid of the gun design program, the effect upon beam transmission by various distributions of magnetic fields can be easily investigated. The sensitivities of the total current and the cathode current density to the changes in the locations and the voltages of the cathode, anode and focusing electrodes can also be determined. By appropriately selecting the locations and voltages of electrodes, the desired beam current and beam power can be realized.

An experimental tube with spiral RF structure replaced by smooth metal conductors has been built based on the results of computer analysis. Measurements have been attempted to verify the theoretical results. However, the tube failed to operate due to fabrication problems before the final test at full beam power could be made. A redesign is recommended to overcome these problems.

C. Report Organization

This report is organized into several sections. In Section II, a brief discussion of the Deformable Mesh Electron Gun Design Program is presented. The details of this program can be found in the users' manual.

Section III is devoted to the description of the Deformable Mesh Electromagnet Design Program. This program is used to calculate the magnetic field strength within the focusing structure. This section also reports on the effort to shape the magnetic fields. Experimental results are found to agree closely with the theory in the low current, low magnetic field cases. For high magnetic field, saturation in the center pole piece reduces the accuracy. In a redesign the center pole piece will be changed to eliminate saturation effects.

Section IV outlines the design procedure. It offers methods to control the total beam current, the beam-filling factor and the cathode current density. It also investigates the effects of locations and voltages of the cathode and electrodes.

Section V describes the structure of the electron gun and explains the rationale behind the configuration. It also discusses some special features in the fabrication. The tube consists of three main parts: magnetic focusing structure, electron gun and vacuum chamber.

In Section VI, the experimental results are discussed in detail. Recommendations are made for modifications in the fabrication of the tube which will eliminate the problems encountered during the measurement program.

Finally, Section VII summarizes this study, sets out the conclusions and offers recommendations for future study.

SECTION II. DEFORMABLE MESH ELECTRON GUN DESIGN PROGRAM

A. Introduction

Shared Applications, Inc. (SAI) has developed advanced techniques for electron-gun design which are directly applicable to the RBTWT electron gun. The Deformable Mesh Electron Gun Design Program is capable of accurate and rapid evaluation of an initial design and its modifications.

The rudiments of electron gun analysis by digital computer are well documented.[5-9] Most programs map the geometry of the gun on a rectangular mesh by an overrelaxation technique and assume an initial charge distribution. Electron trajectories are then calculated from the computed potential distribution to obtain more accurate values of the space charge. This process is iterated to obtain a self-consistent solution.

The SAI Deformable Mesh Electron Gun Program uses a similar strategy to solve a space-charge-limited beam-forming system. However, an important and unique feature of this program is its use of a deformable mesh to accurately model

---

5. P. T. Kirstein and J. S. Hornsby, IEEE Trans. on Electron Devices, vol. ED-11, No. 5, pp. 196-204; May 1964.
6. V. Hamza and G. S. Kino, IEEE Trans. on Electron Devices, vol. ED-14, No. 4, pp. 195-201; Apr. 1967.
7. V. Hamza, IEEE Trans. on Electron Devices, vol. ED-13, No. 5, pp. 485-493; May 1966.
8. J. E. Boers, Tech. Report No. RADC-TR-68-175, Rome Air Development Center, Air Force Systems Command, Griffiss Air Force Base, NY; Apr. 1968.
9. R. B. True, "Space-Charge-Limited Beam Forming Systems Analyzed by the Method of Self-Consistent Fields with a Solution of Poisson's Equation on a Deformable Relaxation Mesh," Ph.D. Thesis, University of Connecticut; 1972.

the true physical configuration, an approach which has proven far superior to the conventional rectangular-mesh method. Accuracy is greatly increased because deformable mesh points are adjusted and so are readily placed on physical boundaries, not simply near them. Furthermore, mesh points can be concentrated in critical regions of the gun to give maximum accuracy where necessary. Because of the ability to use a high mesh density only where it is needed, a typical problem will require fewer points using the deformable mesh method rather than the rectangular mesh method. When this program is used, a curved cathode and grids may be analyzed easily.

B. General Method

The basic solution procedure is outlined in the flow chart shown in Fig. 1. The method of solution is summarized in the following.

1. Generation of Deformable Mesh. Before the simulation can be started, a mesh must be generated which outlines the geometry of the gun and defines the position of each node. The boundaries of the electron gun are given as input data. A satisfactory method can be derived by formulating the zoning problem as a potential problem, with the mesh line playing the role of an equipotential. The program computes the positions of interior points by solving the following Laplace's equations using the method of successive overrelaxation:

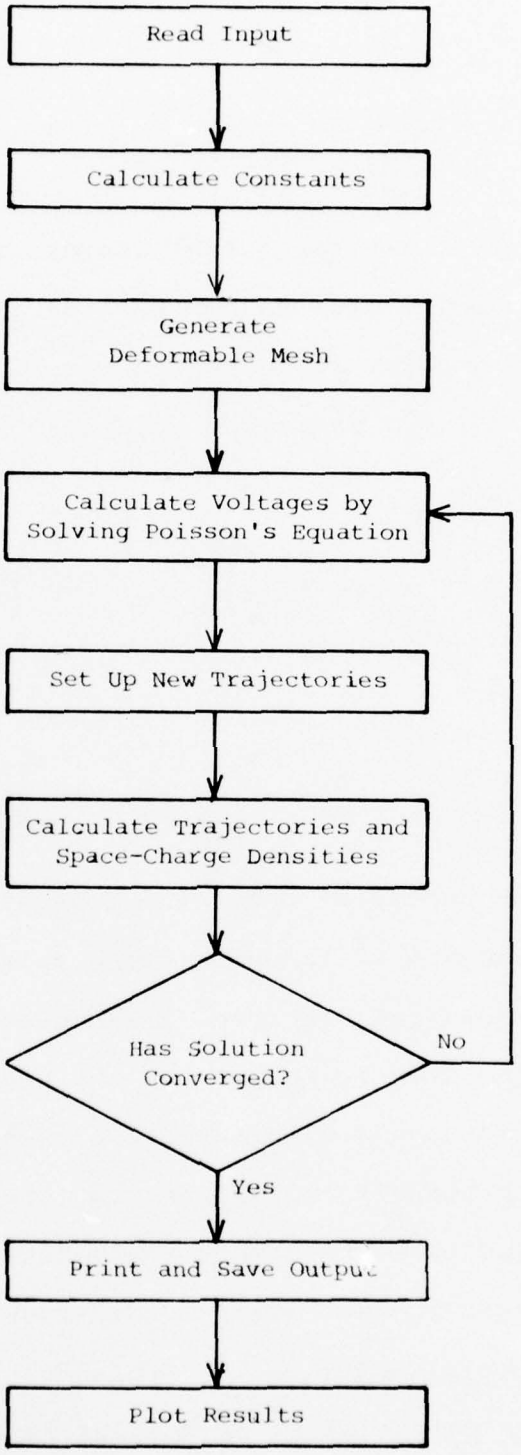

FIG. 1 GENERAL FLOW CHART FOR DEFORMABLE MESH ELECTRON GUN DESIGN PROGRAM.

$$\frac{\partial^2 r}{\partial i^2} + \frac{\partial^2 r}{\partial j^2} = 0 \qquad (1)$$

and

$$\frac{\partial^2 z}{\partial i^2} + \frac{\partial^2 z}{\partial j^2} = 0 \quad . \qquad (2)$$

Here r and z are the actual coordinates of each node and i and j are the indices of the node on the coordinate map. Each mesh point is connected to six neighboring mesh points. The terms r and z are obtained by repeated solution of

$$r_o^{n+1} = r_o^n + \alpha\left(\sum_{i=1}^{6} r_i - 6r_o\right)\Big/6 \qquad (3)$$

and

$$z_o^{n+1} = z_o^n + \alpha\left(\sum_{i=1}^{6} z_i - 6z_o\right)\Big/6 \quad , \qquad (4)$$

where n is the number of the relaxation steps, r_o and z_o are the coordinates of the node being relaxed, r_i, i=1, ..., 6 are six surrounding nodes and α is an overrelaxation parameter. When the difference between the nth and (n+1)th calculations is less than a certain tolerance for all nodes, the solution procedure is assumed complete. Because of the averaging property of solutions to Laplace's equations, a mesh constructed in this way is quite smooth.

2. Potential Solution. Poisson's equation can be solved for the potential at each point given the potentials on the boundaries and the space-charge density at each mesh point. Poisson's equation in cylindrical coordinates with constant θ is

$$\frac{1}{r}\frac{\partial}{\partial r}\left(r\frac{\partial V}{\partial r}\right) + \frac{\partial^2 V}{\partial z^2} = -S(r,z) \quad , \tag{5}$$

where V is the potential and S is the source. The overrelaxation equation is

$$V_o^{n+1} = V_o^n + \alpha_o G_o \Big/ \sum_{i=1}^{6} W_i \quad , \tag{6}$$

where the o represents the point at which the calculation is made and i represents the six neighboring points. The term α_o is an overrelaxation parameter and n is the number of relaxation steps. The residual G_o is defined as[9]

$$G_o = \sum_{i=1}^{6} W_i (V_i - V_o) + S_o \quad . \tag{7}$$

Here W_i is a weighting factor between neighboring points P_o and P_i. Its definition can be found from Winslow[10] as

$$W_i = \frac{1}{2}(r^+ \cot \theta^+ + r^- \cot \theta^-) \quad , \tag{8a}$$

$$r^+ = \frac{1}{3}(r_o + r_i + r_{i+1})\varepsilon_r \tag{8b}$$

and

$$r^- = \frac{1}{3}(r_o + r_i + r_{i-1})\varepsilon_r \quad . \tag{8c}$$

The term S_o is defined as[10]

$$S_o = \sum_{i=1}^{6} a_{i+(1/2)}\left[\rho_{i+(1/2)}/\varepsilon_o\right]\left(\frac{7}{12}\, r^+ + \frac{5}{12}\, r_o\right) \quad , \tag{9}$$

---

10. A. M. Winslow, J. Computational Phys., vol. 2, pp. 149-172; 1967.

where $a_{i+(1/2)}$ and $\rho_{i+(1/2)}$ are the quadrilateral area and space-charge density, respectively, for triangle i+(1/2). The term S_o is negative for electrons.

Figure 2 shows the quantities θ^+, θ^-, r_o, r_i, r_{i+1}, r_{i-1}, P_o and P_i. The term ε_r is the relative dielectric constant for the triangle defined by r_o, r_i and r_{i+1} or r_{i-1}.

Poisson's equation is solved by successive overrelaxation at each point until the residual G_o is smaller than a preset value for every point of the mesh.

3. Cathode Current Density Calculation. Near the cathode surface, a thin rectangular mesh is established by the program. The rectangles are assumed to be essentially parallel plate diodes. Thus, the cathode current density can be calculated by using Child's law:

$$J = \frac{kV^{3/2}}{d^2} , \tag{10}$$

where

$$k = \frac{4}{9} \varepsilon_o \sqrt{2\eta} . \tag{11}$$

In Eq. 11, ε_o is the permittivity of free space and η is the charge-to-mass ratio.

4. Trajectory Equations. Given the electric and magnetic fields, the trajectories of sample electrons are found by solving the Lorentz force equation. The equation in a cylindrical coordinate system (r, θ, z) with an azimuthal magnetic field can be expressed in terms of the field components as[8]

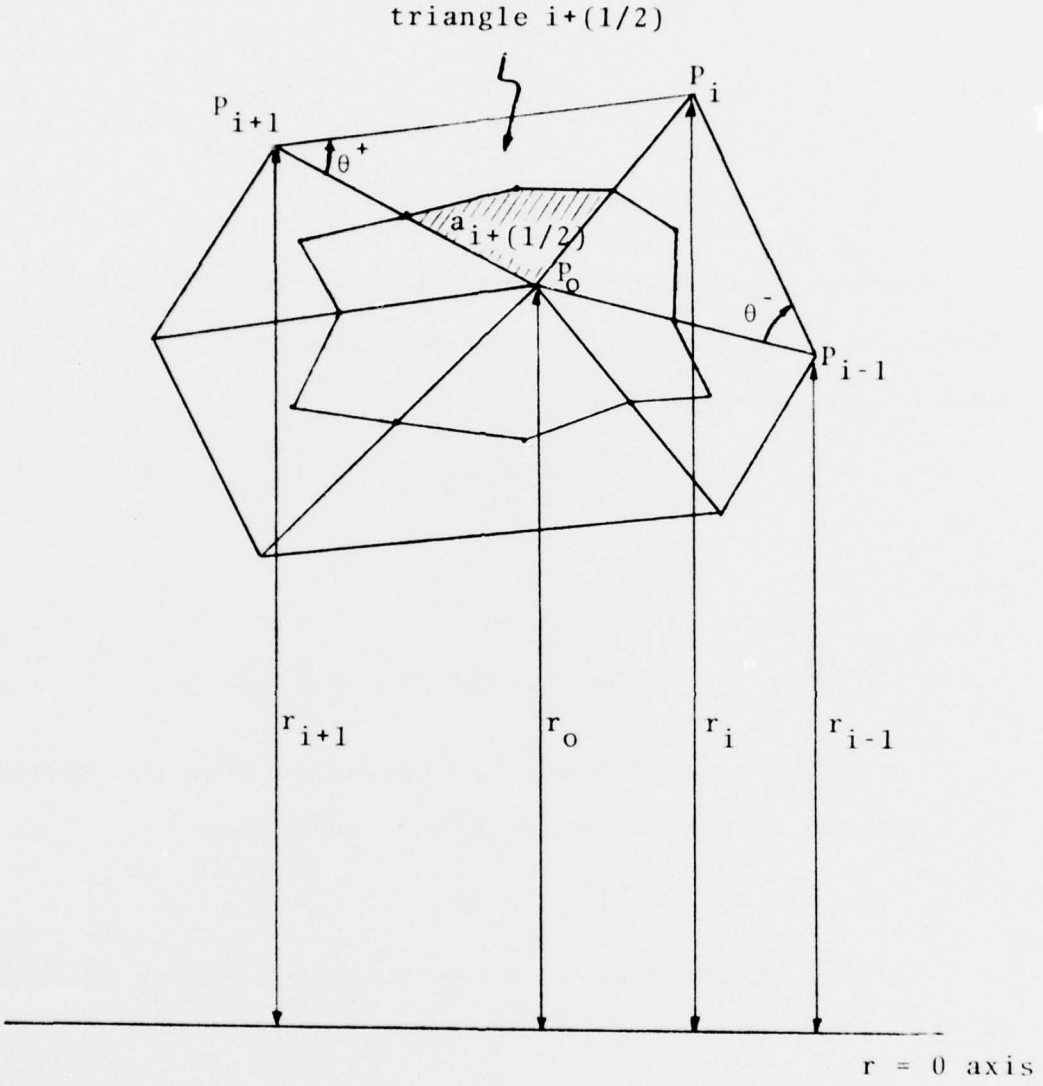

FIG. 2 TYPICAL MESH NODE AND ITS SIX NEIGHBORS AND DODECAGON AREA.

$$\ddot{z} = -\eta(E_z - r\dot{\theta}B_r) \quad , \tag{12}$$

$$\ddot{r} - r\dot{\theta}^2 = -\eta(E_r + r\dot{\theta}B_z) \tag{13}$$

and

$$\frac{d}{dt}(r^2\dot{\theta}) = \eta r(\dot{r}B_z - \dot{z}B_r) \quad . \tag{14}$$

The program accepts values of B_r on the $z = 0$ axis as input data from which B_z can be computed. If $\overline{B} = \nabla \times A$, then it can be shown that

$$B_z = \frac{1}{r}\frac{\partial(rA_\theta)}{\partial r} \tag{15}$$

and

$$A_\theta(r,z) = -\int_0^z B_r(r,z)dz \cong zB_r(r,0) \quad . \tag{16}$$

The electric fields can be calculated from the following equation given the potentials at each node:

$$\overline{E} = -\nabla V \quad . \tag{17}$$

Suppose an electron at P has a nearest node o as shown in Fig. 3. Equation 17 can be expressed as

$$E_r = -\frac{\partial V_p}{\partial r} = -\left[\frac{\partial V_o}{\partial r} + (r_p - r_o) \cdot \frac{\partial^2 V_o}{\partial r^2} + (z_p - z_o)\frac{\partial^2 V_o}{\partial r \partial z}\right] \tag{18a}$$

and

$$E_z = -\frac{\partial V_p}{\partial z} = -\left[\frac{\partial V_o}{\partial z} + (z_p - z_o) \cdot \frac{\partial^2 V_o}{\partial z^2} + (r_p - r_o)\frac{\partial^2 V_o}{\partial r \partial z}\right] \quad . \tag{18b}$$

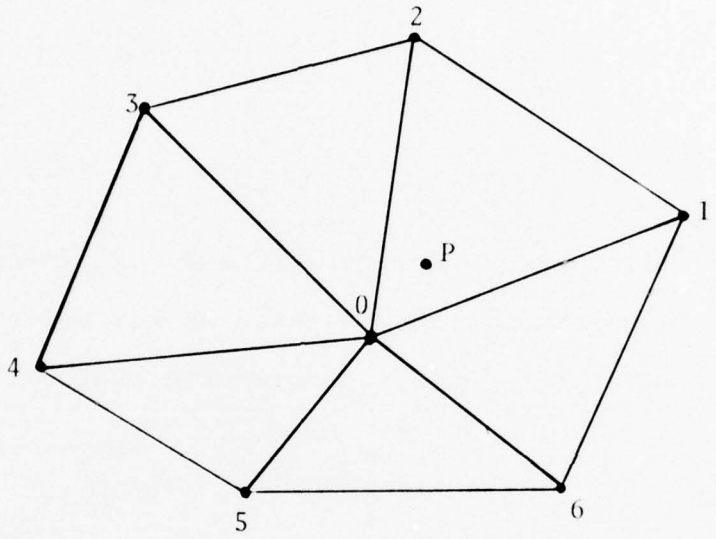

FIG. 2.3 MESH NODE NEAREST AN ELECTRON P AND ITS SIX NEIGHBORING MESH POINTS.

The five derivatives in Eqs. 18 can be found by solving a Taylor series together with the minimization of the Euclidean norm of a residual vector.

Expanding the potential in a Taylor series results in

$$V_i - V_o = (r_i - r_o)\frac{\partial V_o}{\partial r} + (z_i - z_o)\frac{\partial V_o}{\partial z} + \frac{(r_i - r_o)^2}{2!}\frac{\partial^2 V_o}{\partial r^2} + \frac{(z_i - z_o)^2}{2!}\frac{\partial^2 V_o}{\partial z^2} + (z_i - z_o)(r_i - r_o)\frac{\partial^2 V_o}{\partial r \partial z} + \ldots ; \quad i=1, \ldots, 6 \quad (19)$$

There are five unknown derivatives and six linear equations. The least squares solution is taken as the set of derivatives which minimizes the Euclidean norm of a residual vector:

$$\xi_i = V_i - V_o - (r_i - r_o)\frac{\partial V_o}{\partial r} - (z_i - z_o)\frac{\partial V_o}{\partial z} - \frac{(r_i - r_o)^2}{2!}\frac{\partial^2 V_o}{\partial r^2} - \frac{(z_i - z_o)^2}{2!}\frac{\partial^2 V_o}{\partial z^2} - (z_i - z_o)(r_i - r_o)\frac{\partial^2 V_o}{\partial r \partial z} ; \quad i=1, \ldots, 6 \quad (20a)$$

and

$$\|R\|_{min} = \sqrt{\sum_{i=1}^{6} \xi_i^2} \quad . \quad (20b)$$

This procedure can be found in the Scientific Subroutine Package of the IBM computer system.*

*The reader is referred to subroutine MLSQ which can be found in International Business Machines Corporation "IBM System/360 Operating System Pl/I Language Specifications," S360-27, C28-6571-4, IBM Programming Systems Publications, Avenue of the America, New York; 1966.

After the force on the electron has been computed, Newton's second law may be integrated to give the next position of the electron. Continuation of this procedure produces the trajectories of the electron beam.

C. Description of the Program.

To run the program the user must supply as input the voltages of the cathode and electrodes as well as the tube dimensions. The coordinates of all boundary points have to be assigned.

The output consists of lineprinter output for numerical results and incremental plotter output to aid visualization and interpretation of these results. The plots display the following:

1. Mesh
2. Electron trajectories
3. Equipotentials
4. Magnetic field
5. Cathode current density
6. Current densities at selected radii.

For details, an example run is included in the users' manual prepared along with this report.

The results of a run may be saved on and later read from a disk file. The positions and velocities of electrons from the gun program may be saved to provide initial conditions to an RF interaction program. An effective RF interaction program must treat both RF fields and space-charge fields as well as the actual radially varying r- and z-components of the magnetic focusing field.

SECTION III. DESIGN AND FABRICATION OF MAGNETIC FOCUSING STRUCTURE

A. Introduction

The radial-beam traveling-wave tube requires a magnetic field in the direction of motion in the same way as a linear-beam tube in order to prevent spreading and RF-circuit interception through space-charge repulsion. This section outlines the design of an electromagnet that will produce the necessary magnetic field in the experimental tube.

A radial magnetic field will be produced in the beam region by two opposing coils, as illustrated in Figs. 4a and b. Each coil is wound in three electrically insulated sections. The magnetic field can be shaped by adjusting the currents in three segments and by shaping the center pole piece. The two coils will be built identically and corresponding segments will be connected externally in series so that each pair will be operated as a unit. A cylindrical pole piece around the circumference and large disks at each end of the cylinder section hold the coils in place and provide the desired flux paths.

To solve for the magnetic fields inside this structure would be impractical if not impossible to do analytically. Therefore, a numerical technique based on the finite-difference method is used for the solution of magnetic fields. In the following sections, the computer program for electromagnet design will be described. Comparisons between the theoretical results and the measurements will be presented.

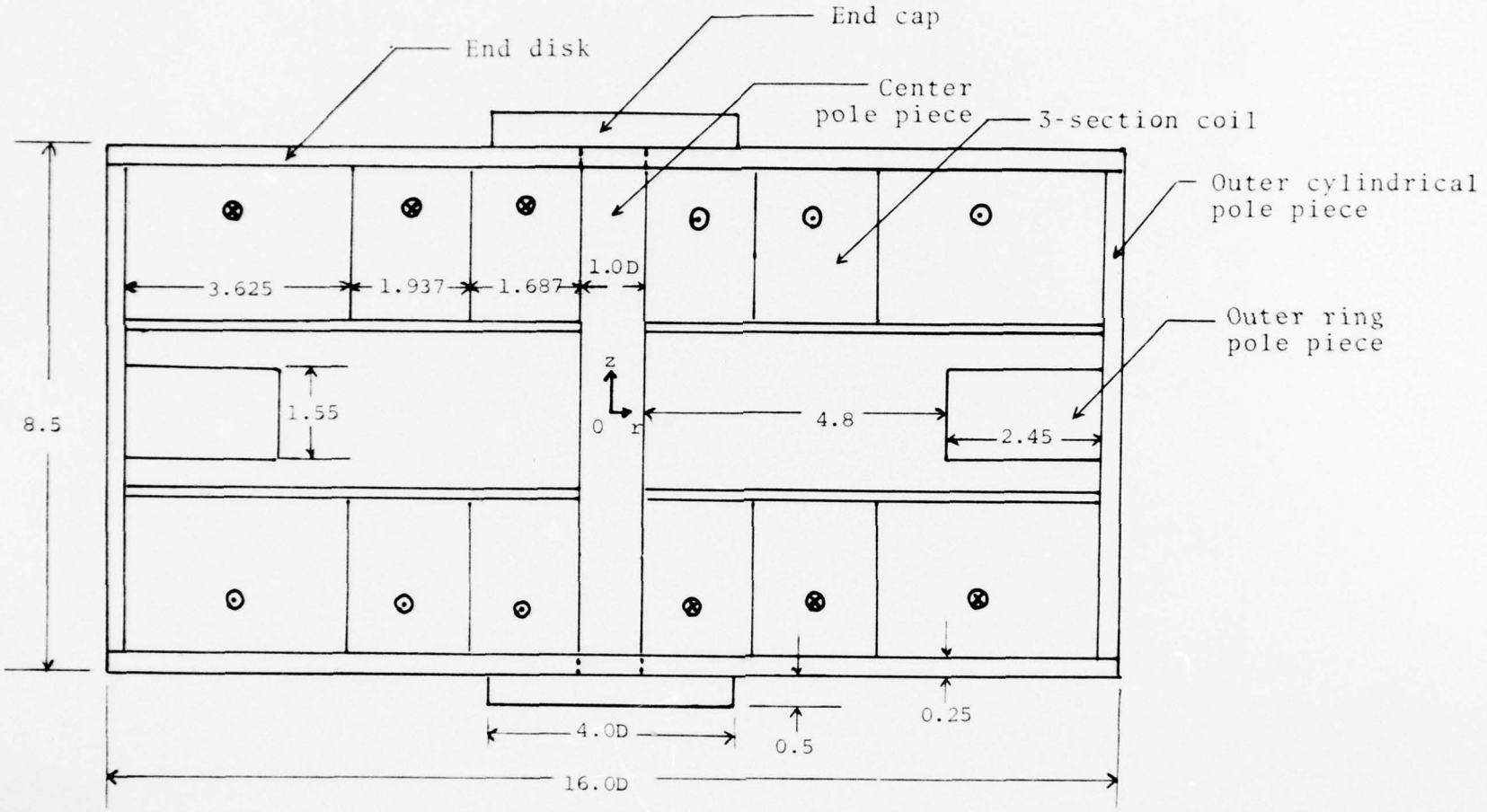

FIG. 4a MAGNETIC FOCUSING STRUCTURE OF RBTWT. (NOT TO SCALE, ALL DIMENSIONS IN INCHES)

FIG. 4b PHOTOGRAPH OF MAGNETIC FOCUSING STRUCTURE.

B. Deformable Mesh Electromagnet Design Program

A Deformable Mesh Electromagnet Design Program developed by Holsinger of Los Alamos Scientific Laboratory, University of California, is used here to solve the magnetic fields for different current levels in the three coil segments. The program is based on a finite-difference method to solve Poisson's equation as described by Winslow.[10] The basic technique of solving Poisson's equation is quite similar to the electron gun program in Section II if all the electrostatic symbols are replaced with their corresponding magnetostatic symbols.

The program is divided into three parts: generation of the deformable mesh, solution of Poisson's equation and plotting of the results. The physical boundaries and currents in the coils are supplied as input. The output consists of computer printouts of magnetic fields and Calcomp plots of mesh and magnetic flux. The results can be saved on tape or disk for restart.

C. Fabrication of the Magnetic Focusing Structure

An outline drawing of the magnetic focusing structure is shown in Fig. 4a. It consists of a center pole piece, an outer cylinder pole piece, two end disks, an outer ring pole piece, two end caps for the center pole piece and three pairs of stainless steel spools to hold the coils.

The pole pieces and end disks were made from magnetic materials. Hot rolled steel was used for its reasonable price and high permeability and saturation. Since saturation would be expected to occur first at the center pole piece, an

annealed iron with very high saturation was chosen for its fabrication. A small slot was machined at the outer cylinder pole piece to allow access of a magnetic field probe and the vacuum pump connection.

The wire for the coils was 16 gauge copper magnet wire. Between the layer of wire and the stainless steel spool, a mylar sheet was inserted for better electric insulation. Mylar sheets were also placed between successive layers of wire to improve the alignment and guarantee the electric insulation.

A thermocouple was embedded at the center of the second coil to allow the operating temperature to be monitored.

The number of turns and the resistance in the three sections of each coil are as follows:

N_1 = 930 turns $\qquad$ R_1 = 2.3 Ω

N_2 = 1,280 turns $\qquad$ R_2 = 8.0 Ω

N_3 = 2,350 turns $\qquad$ R_3 = 29.0 Ω

Later, it will be shown that a current level of I_1 = 3.4 A, I_2 = 3.8 A and I_3 = 2.7 A is suitable for tube operation. With this current level, the power dissipation is about 707 watts for the entire focusing structure. The temperature at the center of the second coil (i.e., the location of the thermocouple) remains below 60°C for at least a half-hour without additional cooling apparatus. However, the coils were designed to operate safely up to 200°C.

A photograph of the focusing structure is shown in Fig. 4b.

D. Shaping the Magnetic Fields

Theoretically, the minimum radial magnetic focusing field B_r is given from the Brillouin flow condition[9]

$$\omega_c = \sqrt{2}\,\omega_p \quad , \tag{21}$$

where ω_p is the beam-plasma frequency and ω_c is the magnetic cyclotron frequency ($\omega_c = \eta B_r$). This condition applies to radial flow under the assumption that each electron "sees" the local radial direction as its axis of rotation. In practice, a confined-flow field of twice the Brillouin field or greater should be used for better focusing, particularly under RF conditions. As the ideal beam spreads radially, its density falls in proportion to 1/R (R is the radius and identical to r in the previous sections), ω_p falls as $1/\sqrt{R}$ and thus a magnetic field falling as $1/\sqrt{R}$ will maintain balanced flow. The Brillouin field requried to focus a beam of voltage V_b and current density $J(A/cm^2)$ is $1{,}472\ J^{1/2}/V_b^{1/4}$ G. For a 1.2 kW and 1,000 V beam, this is 225 G at the cathode surface. Thus, our goal to design a nominal maximum of 2,000 G at cathode is an ample overdesign. The actual minimum magnetic field required to focus the beam will be determined by computer simulation using the design program, as will be seen in the next section.

Figure 5 shows an ideal magnetic field falling as $1/\sqrt{R}$ with a flux density of 2,000 G at the cathode (i.e., at R = 1 inch). Also shown in this figure are the results of the magnetic field calculations for coils with different current levels in three segments (3.4 A, 3.8 A, 2.7 A) and for coils with the same current levels in three sections (2.1 A, 2.1 A,

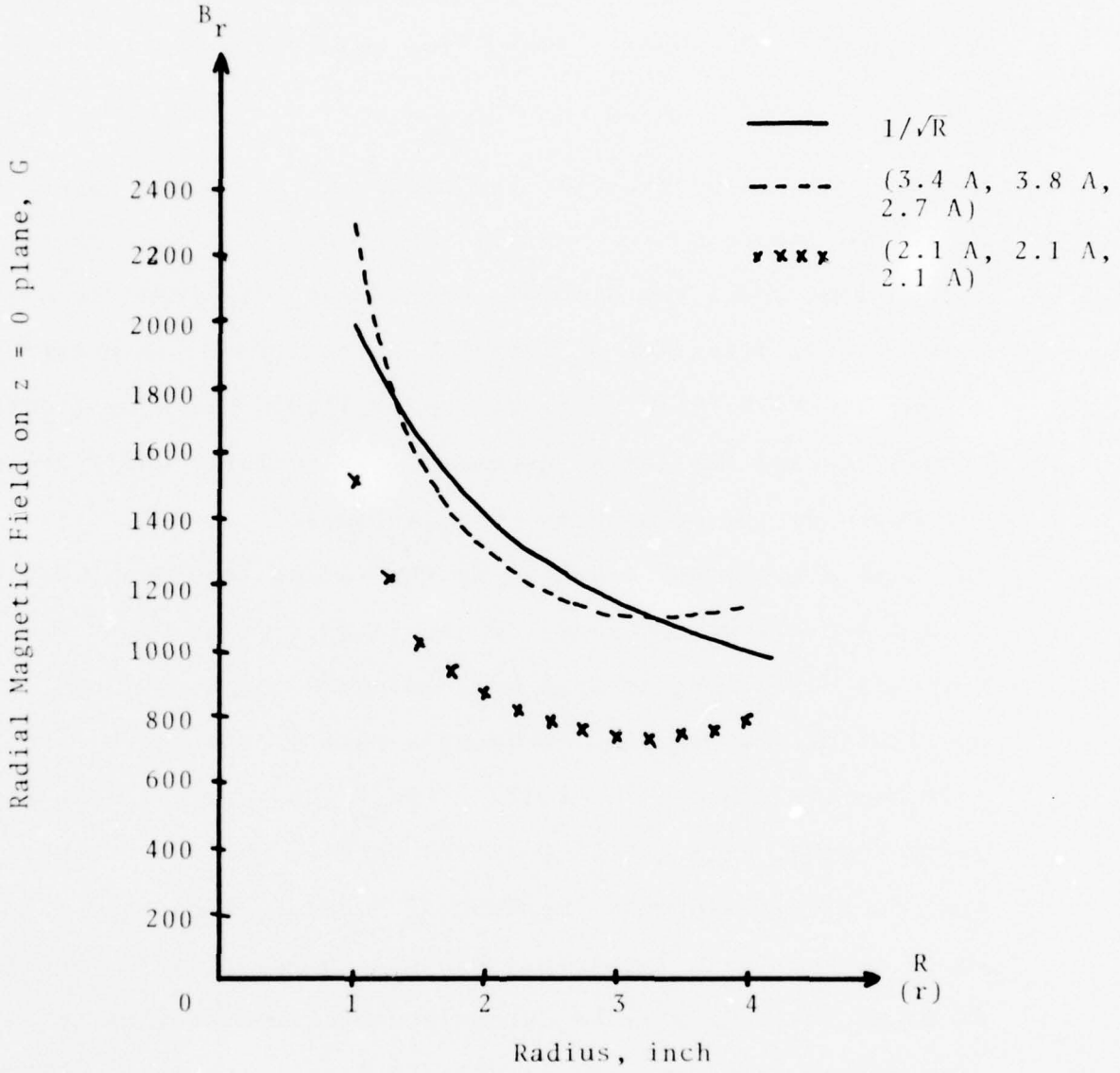

FIG. 5 IDEAL MAGNETIC FIELD (SOLID LINE) AND COMPUTED MAGNETIC FIELDS (CROSSES, BROKEN LINE).

2.1 A). The first value inside the parenthesis is the current level in the coil segment closest to the center pole piece. The center pole piece is not shaped for these calculations. Unless otherwise mentioned, all the calculations are made under the assumption that $\mu = \infty$, where μ is the permeability of the magnetic material.

To investigate the effect of shaping the center pole piece, a concave surface of radius of curvature 0.8 inch is machined in the position behind the cathode, as shown in Fig. 6. The computer results are shown in Fig. 7a for current levels of 3.4 A, 3.8 A, 2.7 A as well as the results with an unshaped pole piece for comparison. Figure 7b shows the comparison for current levels of 2.1 A, 2.1 A, 2.1 A. It is interesting to note that shaping the center pole piece lowers the magnetic field in the cathode region but does not significantly affect the far zone field. In order to maintain a high magnetic field at the cathode region, it was decided not to shape the center pole piece.

The mesh plot and the magnetic flux plot for an unshaped center pole piece at current levels of 2.1 A, 2.1 A, 2.1 A are shown in Figs. 8 Figure 9a shows a mesh plot for a shaped center pole piece. The magnetic flux plots are shown in Fig. 9b for current levels of 1.7 A, 1.9 A, 1.35 A and in Fig. 9c for current levels of 3.4 A, 3.8 A, 0 A.

E. Magnetic Field Measurements

The magnetic field at the center line of the focusing structure (i.e., the $z = 0$ plane) can be measured easily by

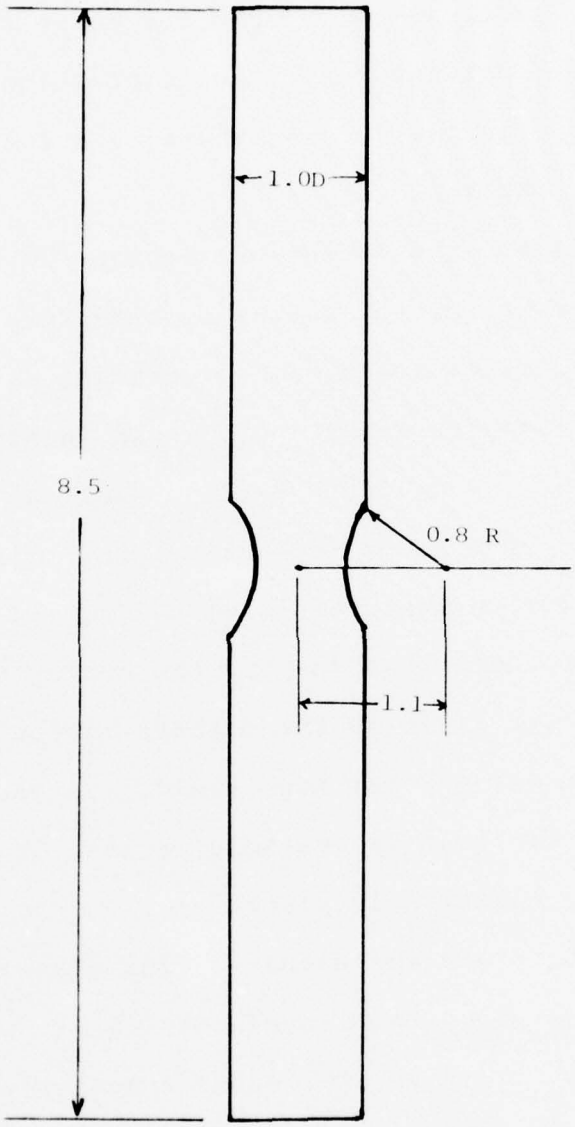

FIG. 6 SHAPED CENTER POLE PIECE (NOT TO SCALE, ALL DIMENSIONS IN INCHES)

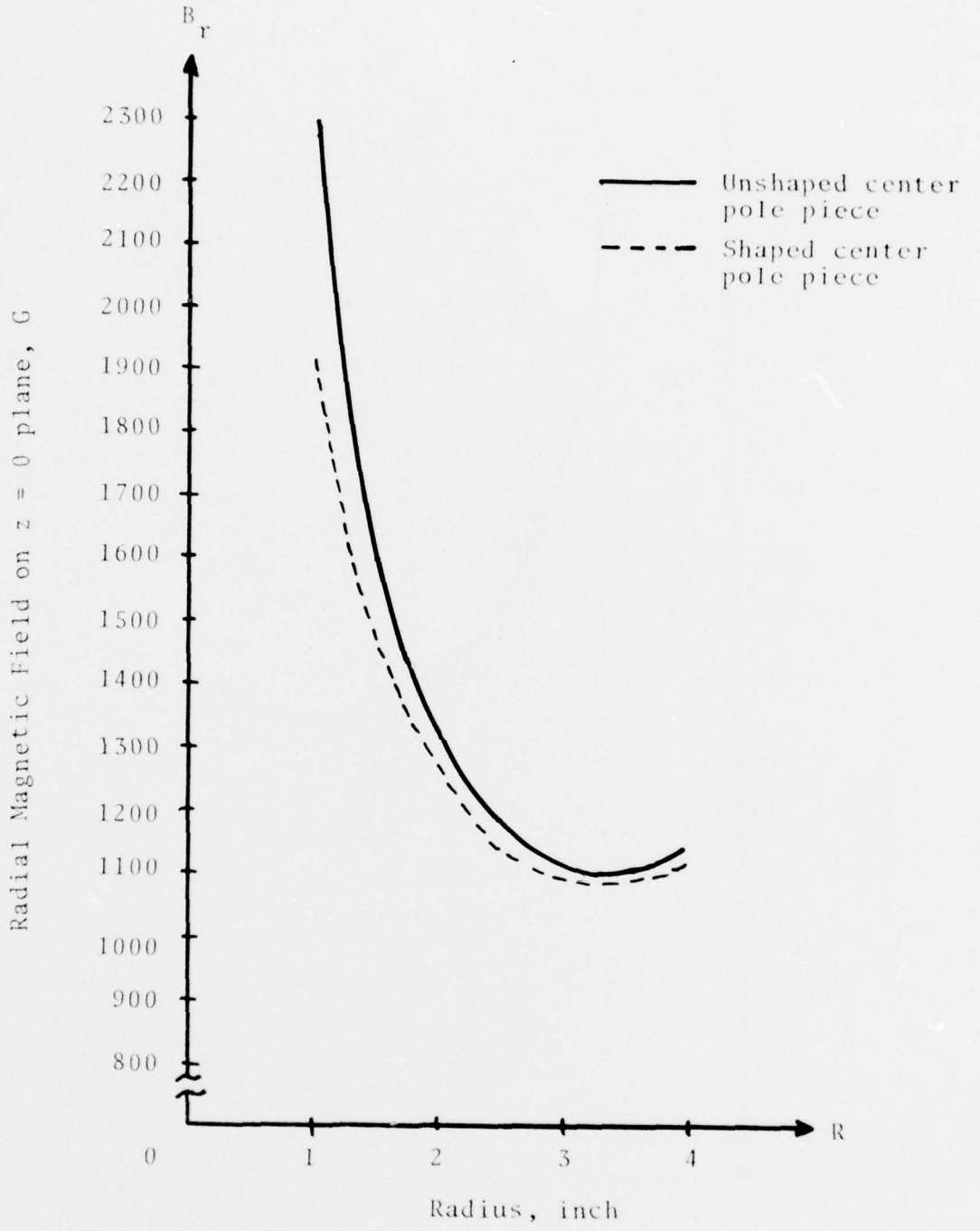

FIG. 7a THE EFFECT OF A SHAPED CENTER POLE PIECE WITH CURRENT LEVELS AT THE THREE SECTIONS OF COIL AT 3.4 A, 3.8 A, 2.7 A.

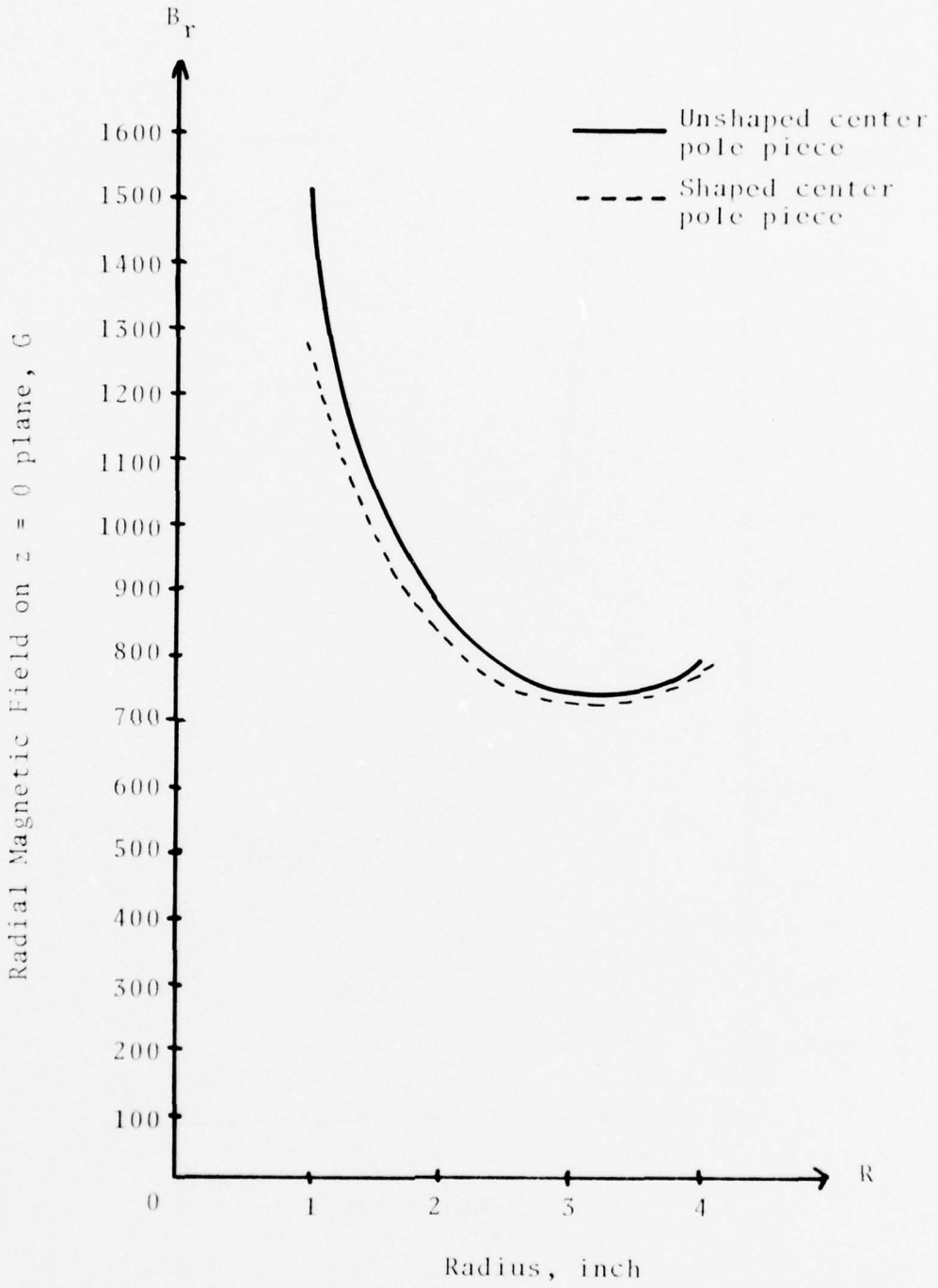

FIG. 7b THE EFFECT OF A SHAPED CENTER POLE PIECE WITH CURRENT LEVELS AT THE THREE SECTIONS OF COIL AT 2.1 A, 2.1 A, 2.1 A.

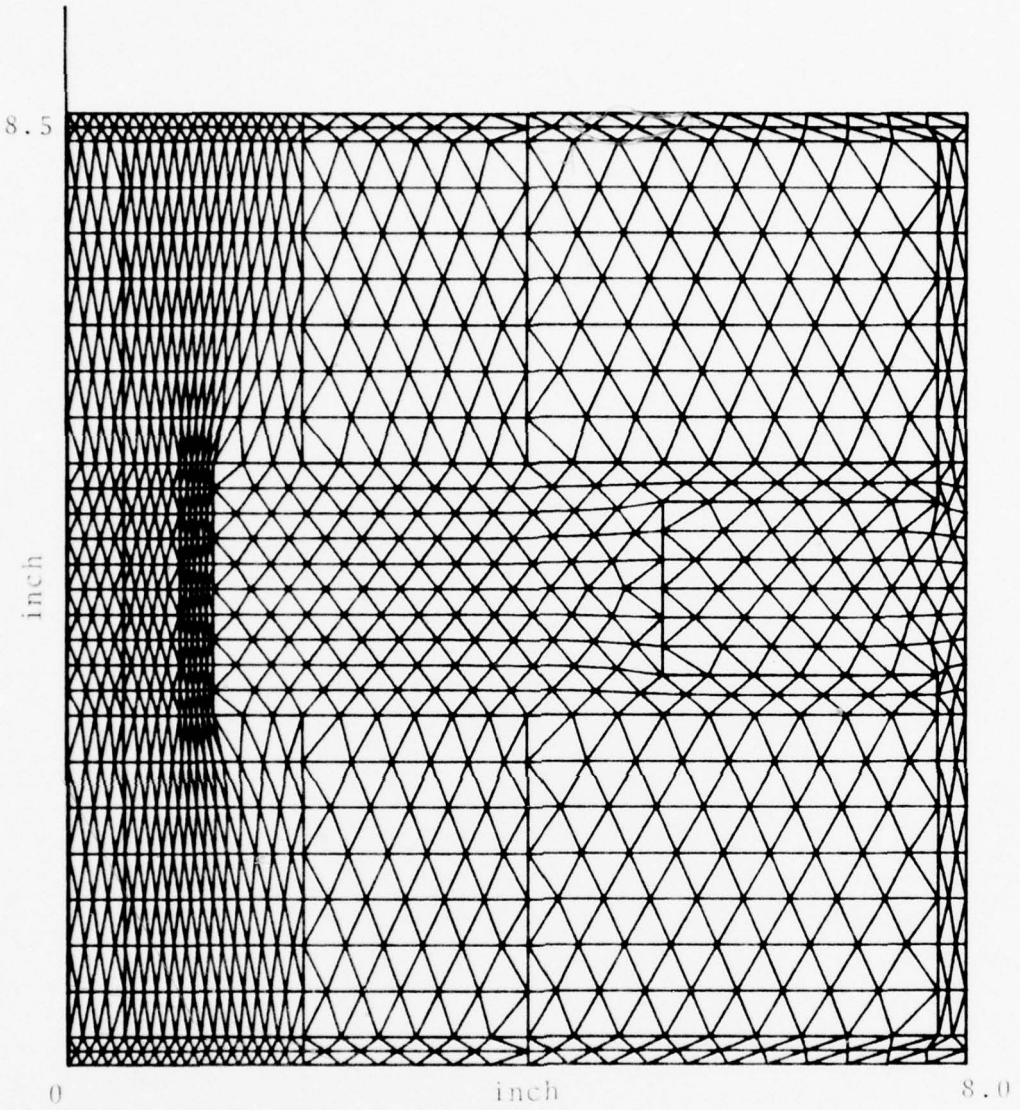

a. Mesh Plot

FIG. 8a MESH PLOT FOR A MAGNETIC FOCUSING STRUCTURE WITH AN UNSHAPED CENTER POLE PIECE AND COIL CURRENT LEVELS OF 2.1 A, 2.1 A, 2.1 A.

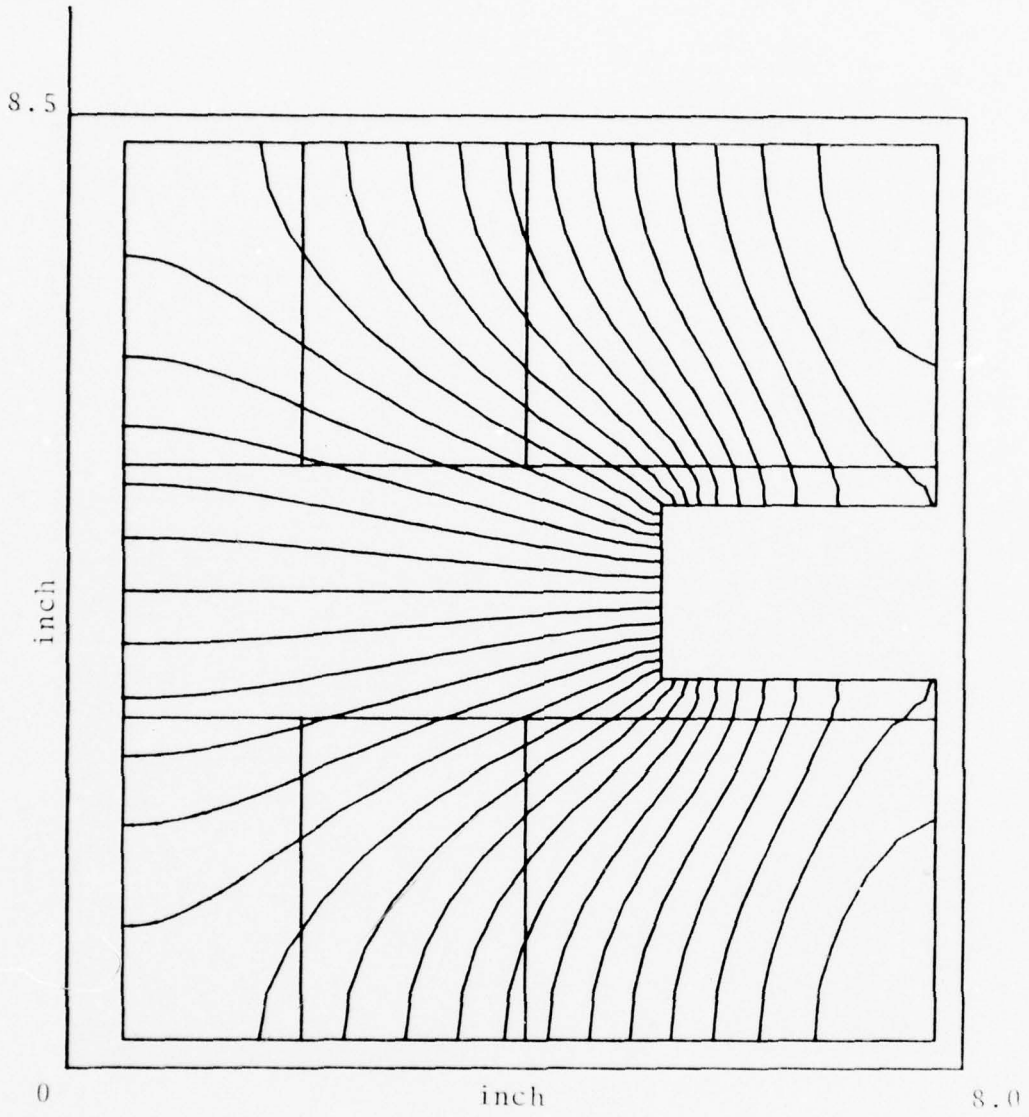

b. Magnetic Flux Plot

FIG. 8b MAGNETIC FLUX PLOT FOR A MAGNETIC FOCUSING STRUCTURE WITH AN UNSHAPED CENTER POLE PIECE AND COIL CURRENT LEVELS OF 2.1 A, 2.1 A, 2.1 A.

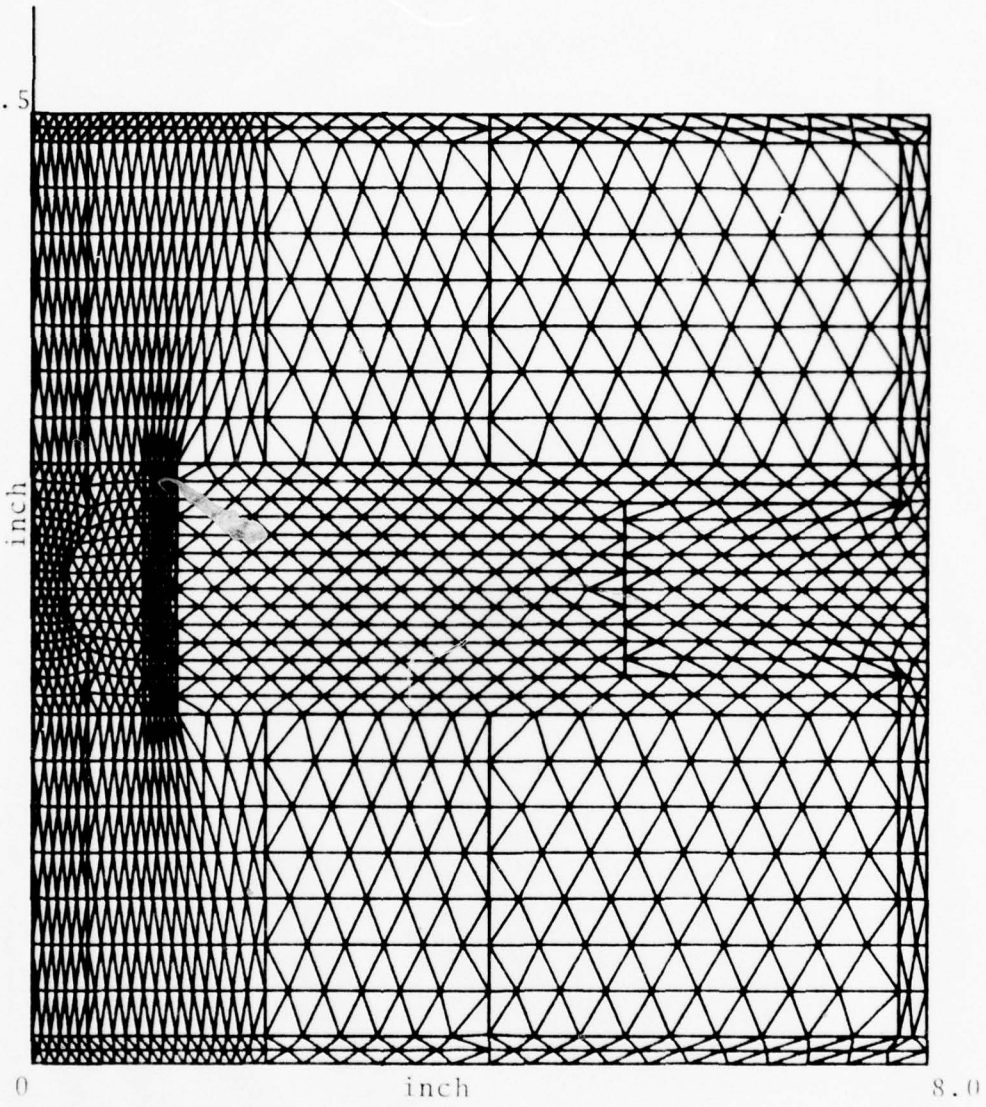

a. Mesh Plot

FIG. 9a MESH PLOT FOR A MAGNETIC FOCUSING STRUCTURE WITH A SHAPED CENTER POLE PIECE.

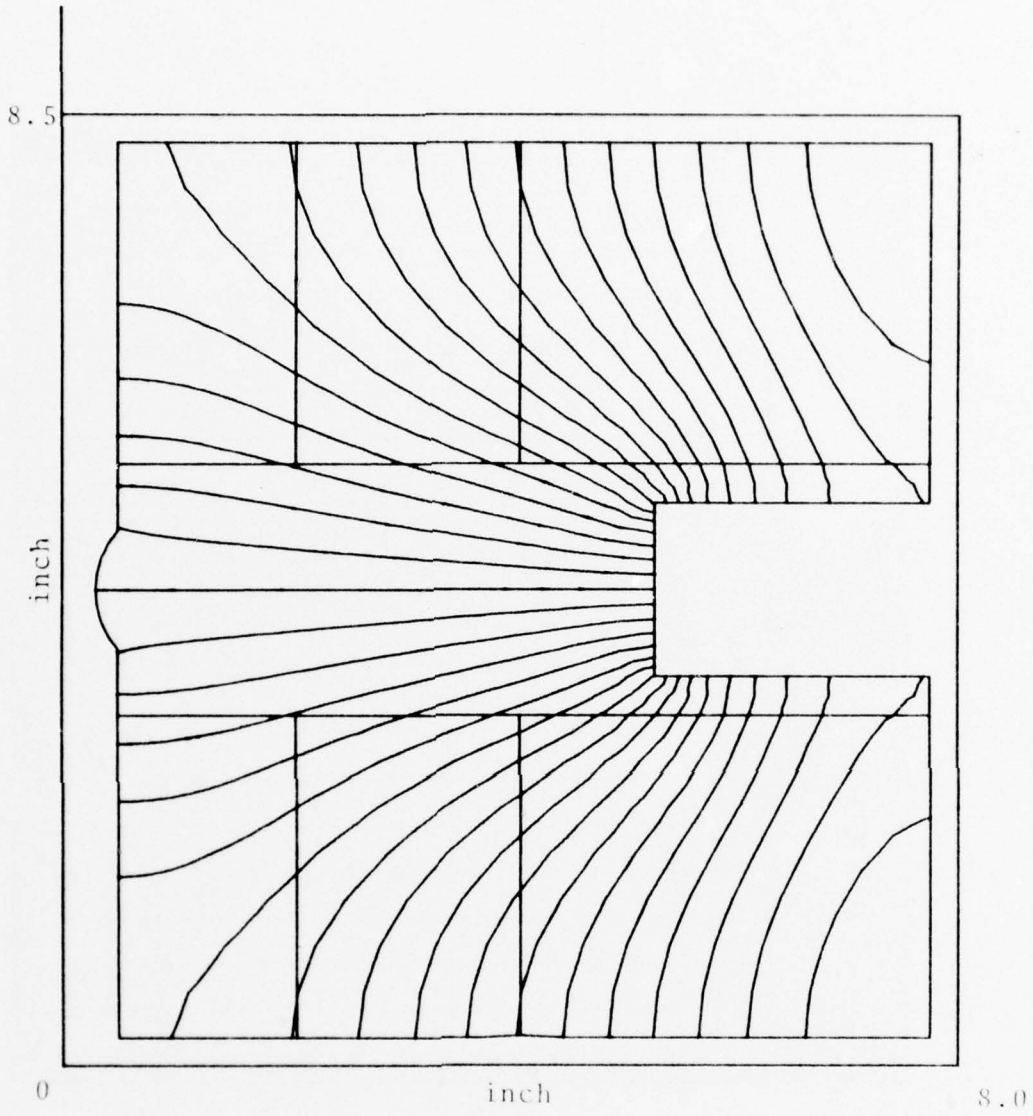

b. Magnetic Flux Plot for Current Levels of 1.7 A, 1.9 A, 1.35 A

FIG. 9b MAGNETIC FLUX PLOT FOR CURRENT LEVELS OF 1.7 A, 1.9 A, 1.35 A FOR A MAGNETIC FOCUSING STRUCTURE WITH A SHAPED CENTER POLE PIECE.

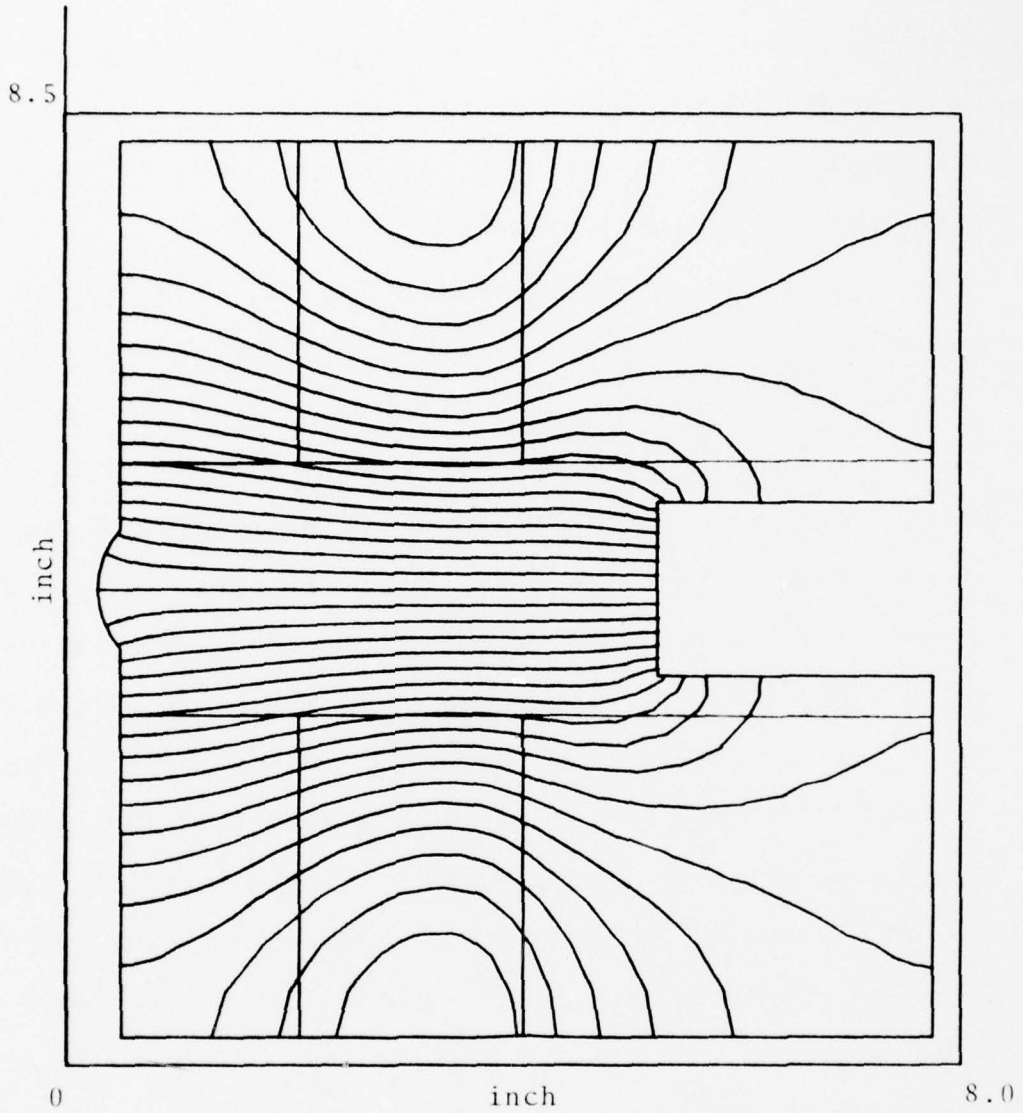

c. Magnetic Flux Plot for Current Levels of 3.4 A, 3.8 A, 0 A.

FIG. 9c MAGNETIC FLUX PLOT FOR CURRENT LEVELS OF 3.4 A, 3.8 A, 0 A FOR A MAGNETIC FOCUSING STRUCTURE WITH A SHAPED CENTER POLE PIECE.

inserting a Hall-effect probe through the slot at the outer cylinder pole piece. With the annealed iron center pole piece to be used later in the experimental tube, experimental results are compared with theoretical calculations for different current levels in Figs. 10 through 15.

For low magnetic fields (low current levels), the agreement between the computer calculations and measurements is excellent. However, as the current levels increase, the gap between calculation and measurement widens. The reason is that saturation effects at the center pole piece inhibit the increase of magnetic field along the center line. For example, the theoretical calculation predicts that the magnetic field strength should double in magnitude as the current levels increase by a factor of two, as shown in Figs. 10 and 14. But the measured data show that the increase is by a factor much less than two. If the annealed iron center pole piece is replaced by mu-metal, the saturation effect is more pronounced, since the mu-metal has a much lower saturation magnetic field than annealed iron. Figures 16 and 17 show the measurements with the center pole piece of different materials: the mu-metal, the hot-rolled steel and the annealed iron. The results show that the hot-rolled steel and annealed iron have almost the same saturation value, but the mu-metal has a much lower saturation.

To avoid saturation, it is important to begin with a high saturation material for the center pole piece. The results may be improved further by increasing the cross-sectional area

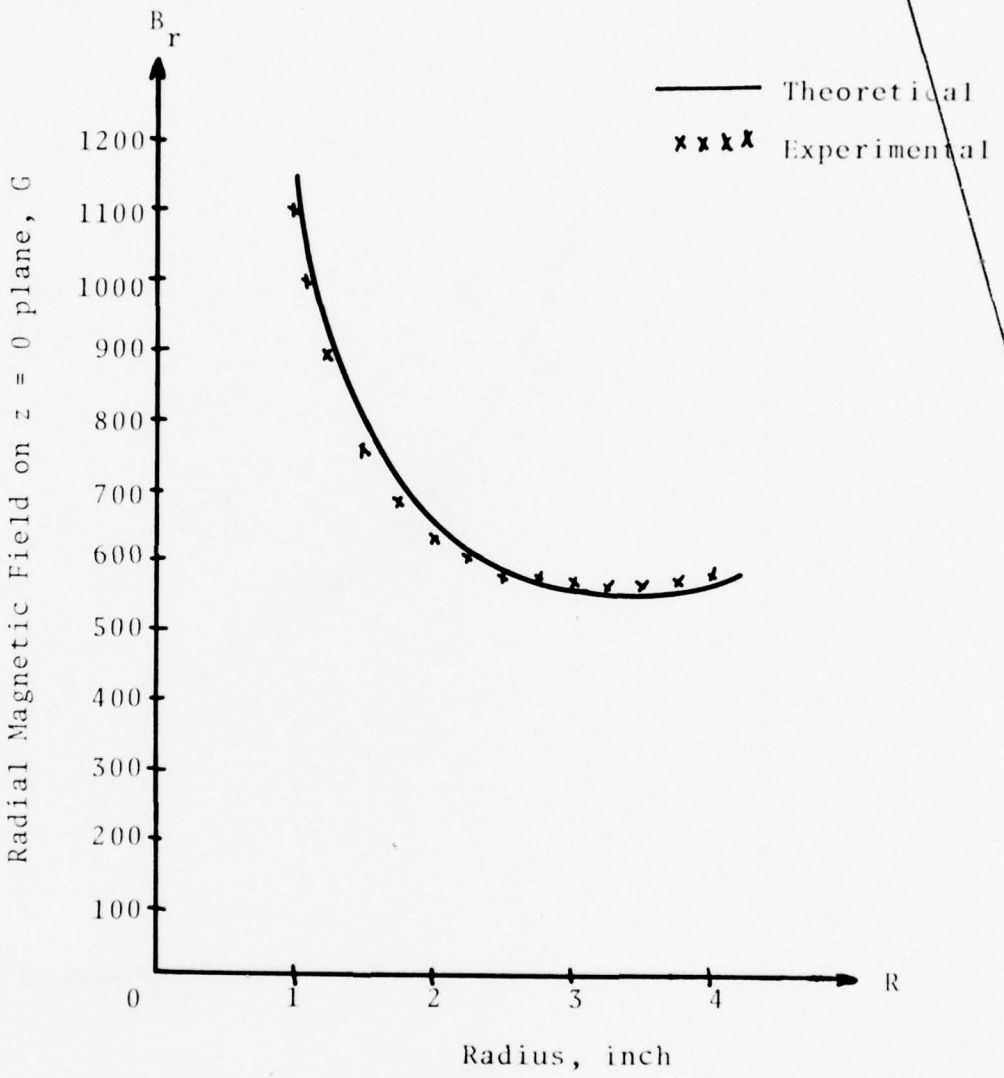

FIG. 10 COMPARISON OF COMPUTER RESULTS WITH EXPERIMENTAL MEASUREMENTS FOR CURRENT LEVELS OF 1.7 A, 1.9 A, 1.35 A. (SOLID LINE SHOWS THE COMPUTER RESULTS)

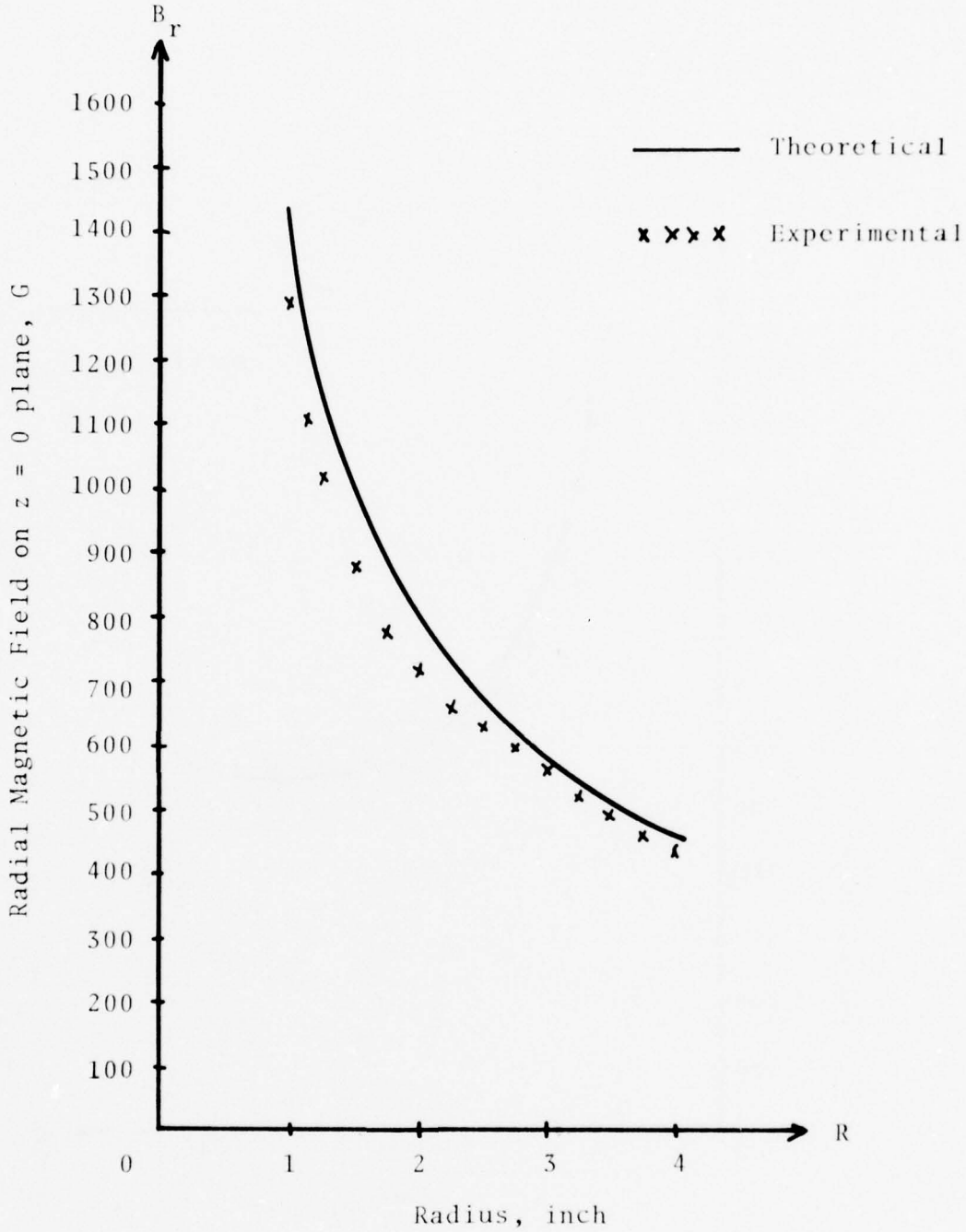

FIG. 11 COMPARISON OF COMPUTER RESULTS WITH EXPERIMENTAL MEASUREMENTS FOR CURRENT LEVELS OF 2.9 A, 3.8 A, 0 A. (SOLID LINE SHOWS THE COMPUTER RESULTS)

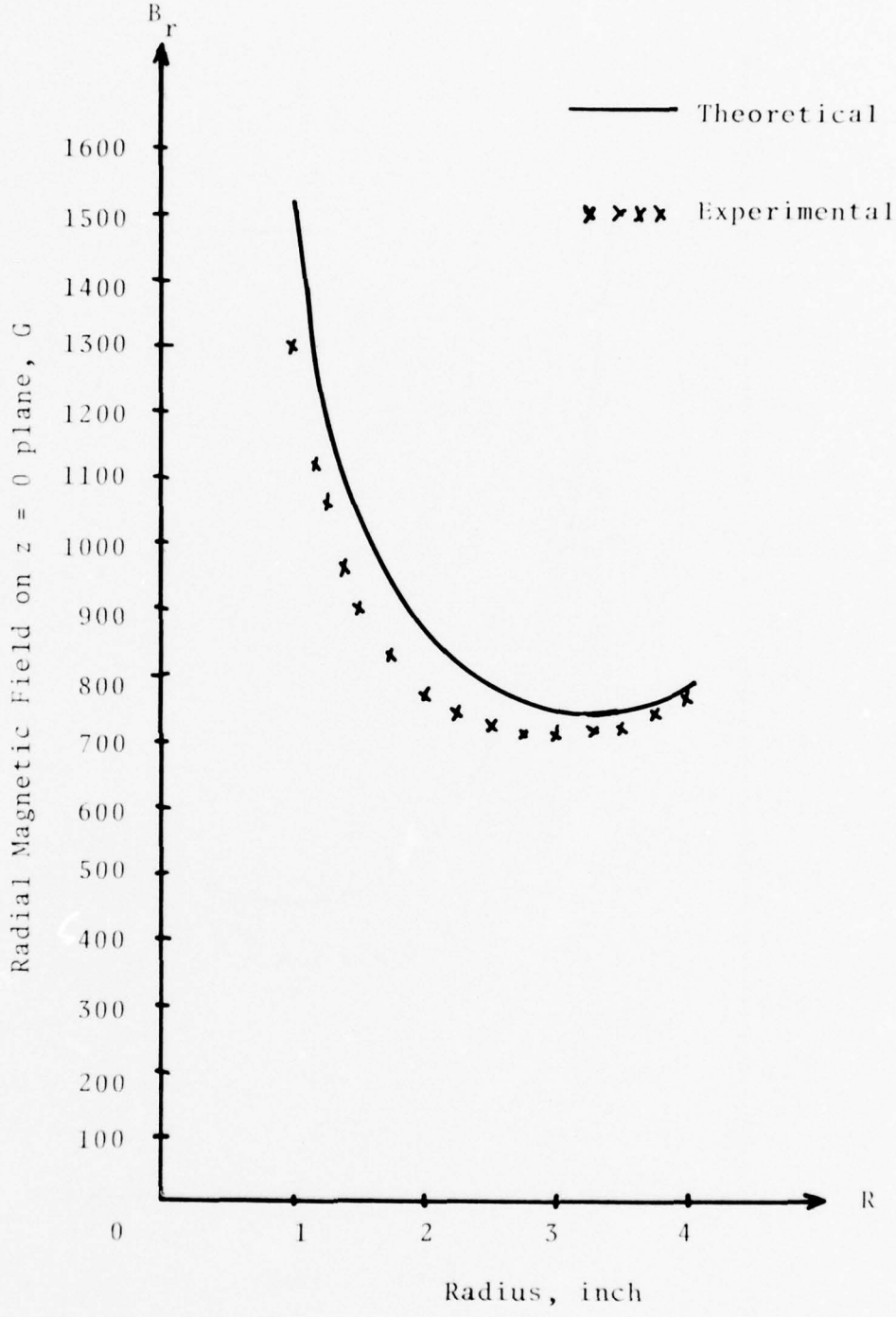

FIG. 12 COMPARISON OF COMPUTER RESULTS WITH EXPERIMENTAL MEASUREMENTS FOR CURRENT LEVELS OF 2.1 A, 2.1 A, 2.1 A. (SOLID LINE SHOWS THE COMPUTER RESULTS)

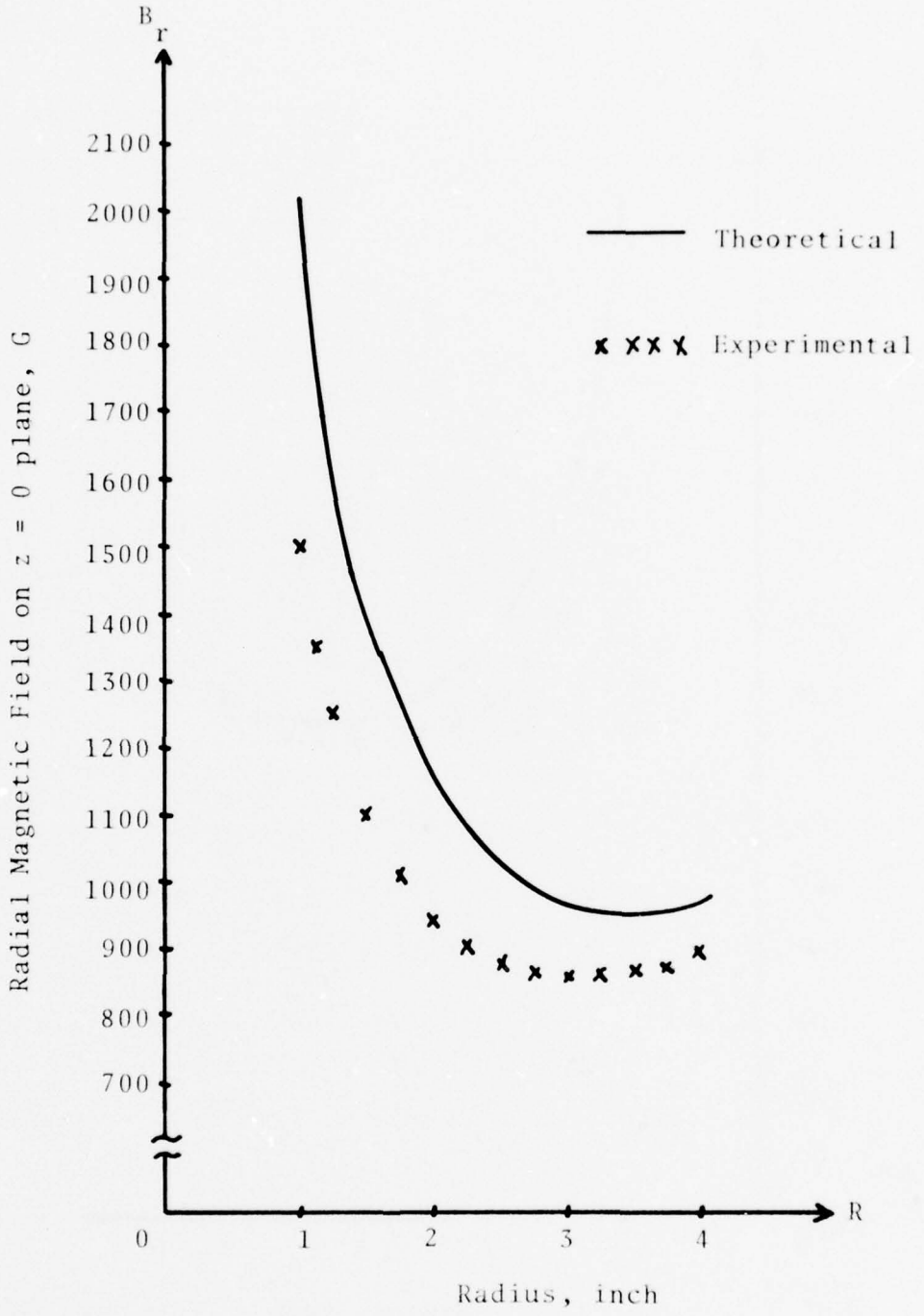

FIG. 13 COMPARISON OF COMPUTER RESULTS WITH EXPERIMENTAL MEASUREMENTS FOR CURRENT LEVELS OF 2.9 A, 3.8 A, 2.1 A. (SOLID LINE SHOWS THE COMPUTER RESULTS)

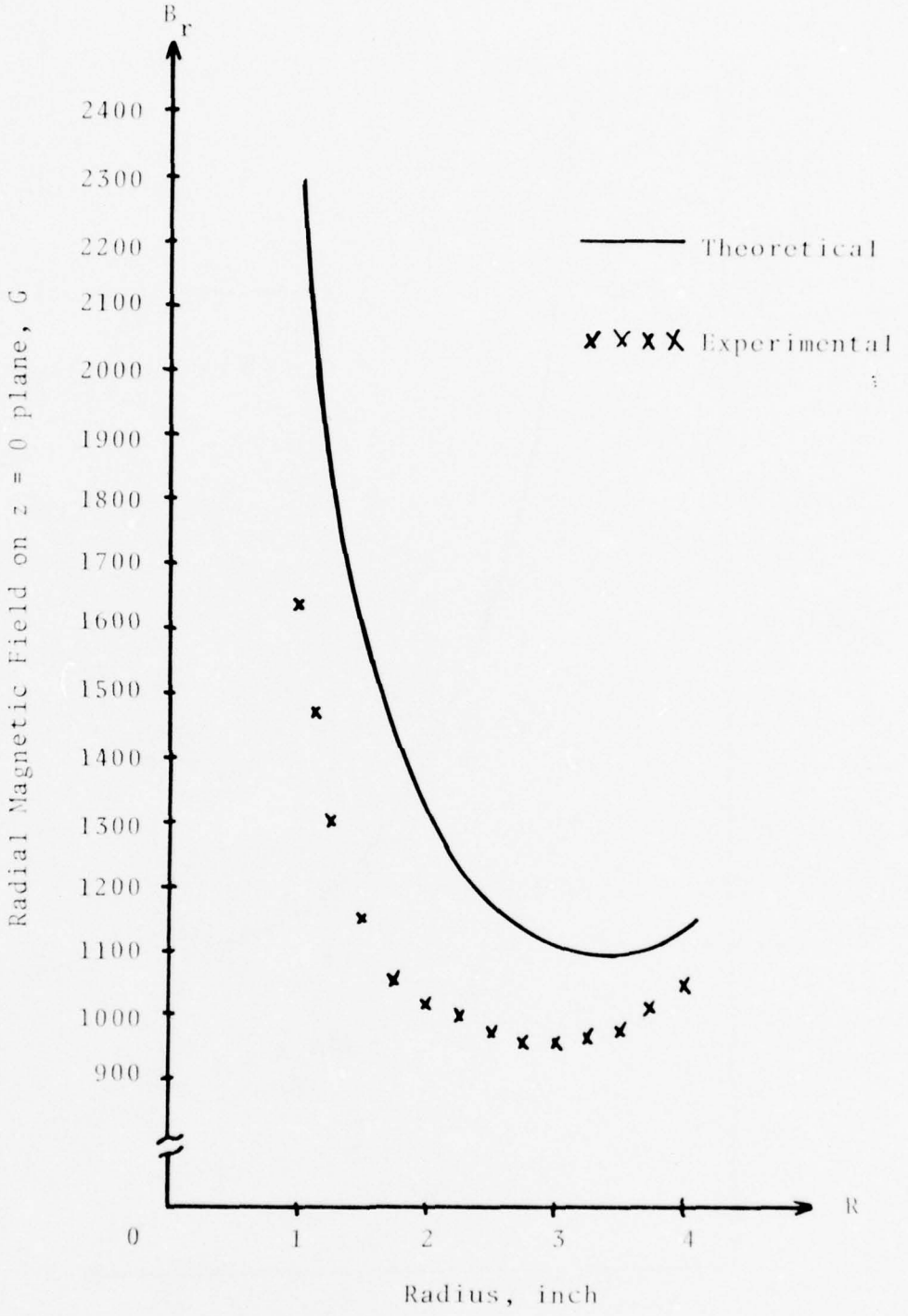

FIG. 14 COMPARISON OF COMPUTER RESULTS WITH EXPERIMENTAL MEASUREMENTS FOR CURRENT LEVELS OF 3.4 A, 3.8 A, 2.7 A. (SOLID LINE SHOWS THE COMPUTER RESULTS)

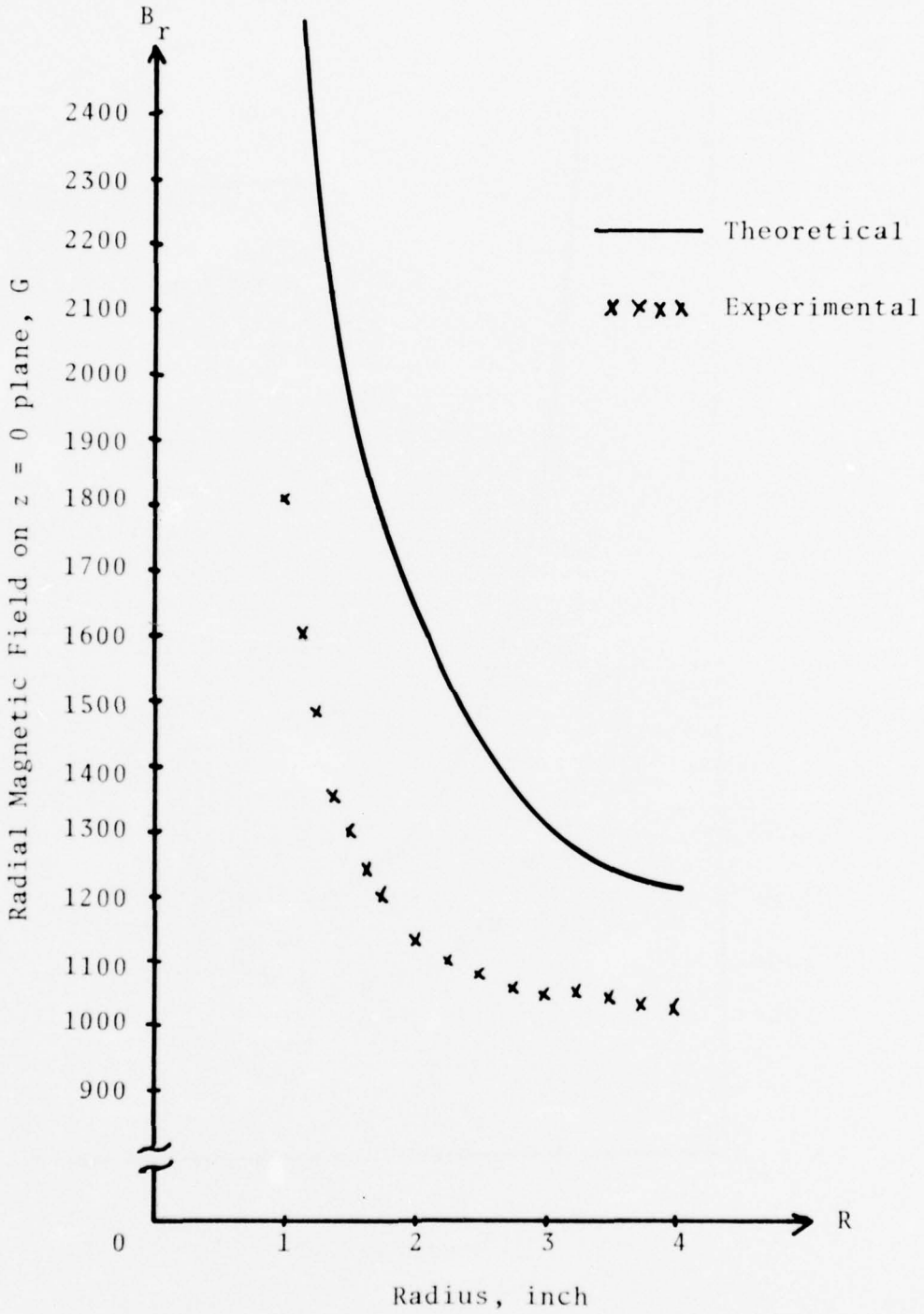

FIG. 15 COMPARISON OF COMPUTER RESULTS WITH EXPERIMENTAL MEASUREMENTS FOR CURRENT LEVELS OF 5 A, 6 A, 2 A. (SOLID LINE SHOWS THE COMPUTER RESULTS)

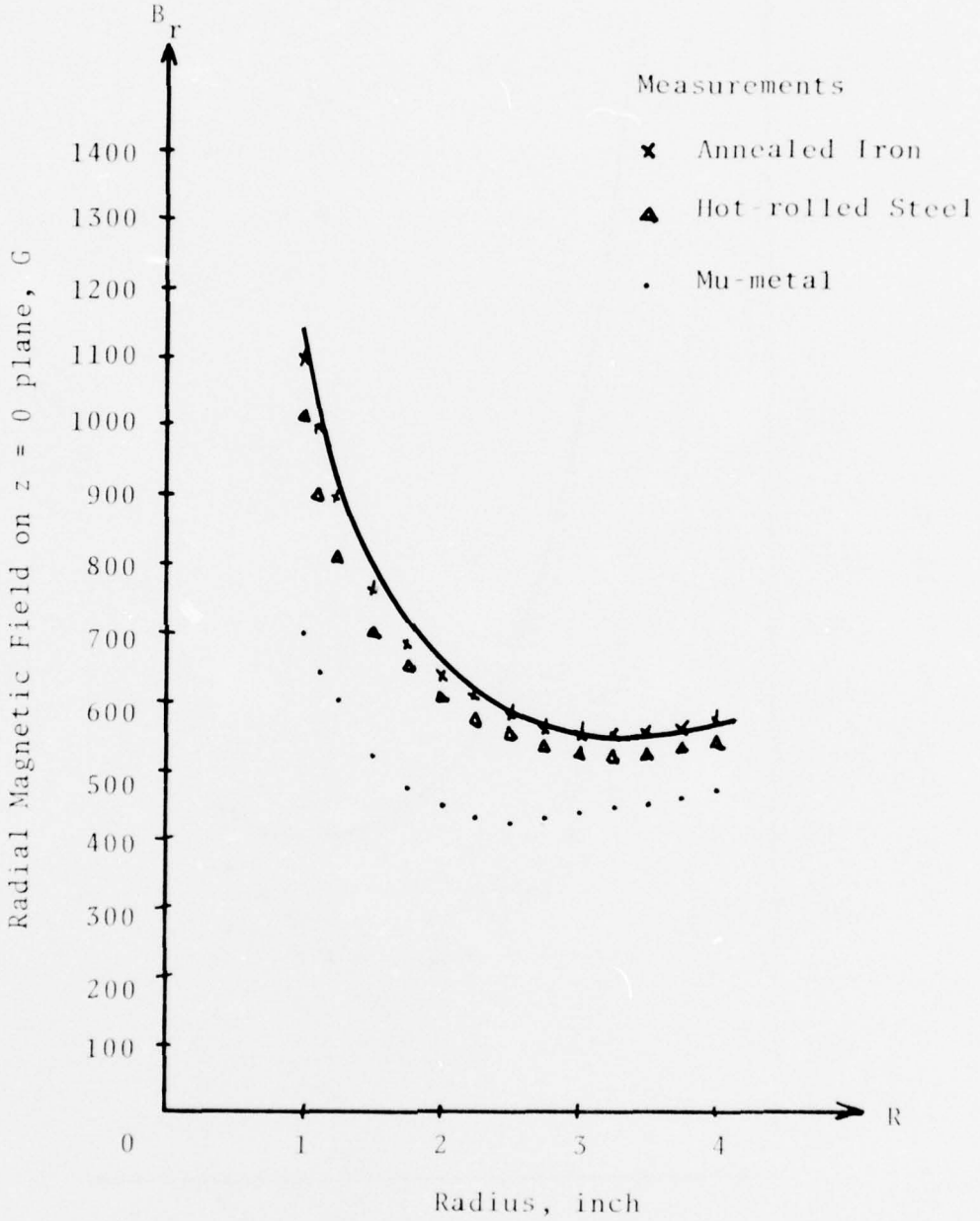

FIG. 16 MEASUREMENTS FOR CENTER POLE PIECES OF DIFFERENT MATERIALS. (SOLID LINE SHOWS THEORETICAL RESULTS; CURRENT LEVELS IN THE THREE SECTIONS OF COIL ARE 1.7 A, 1.9 A, 1.35 A)

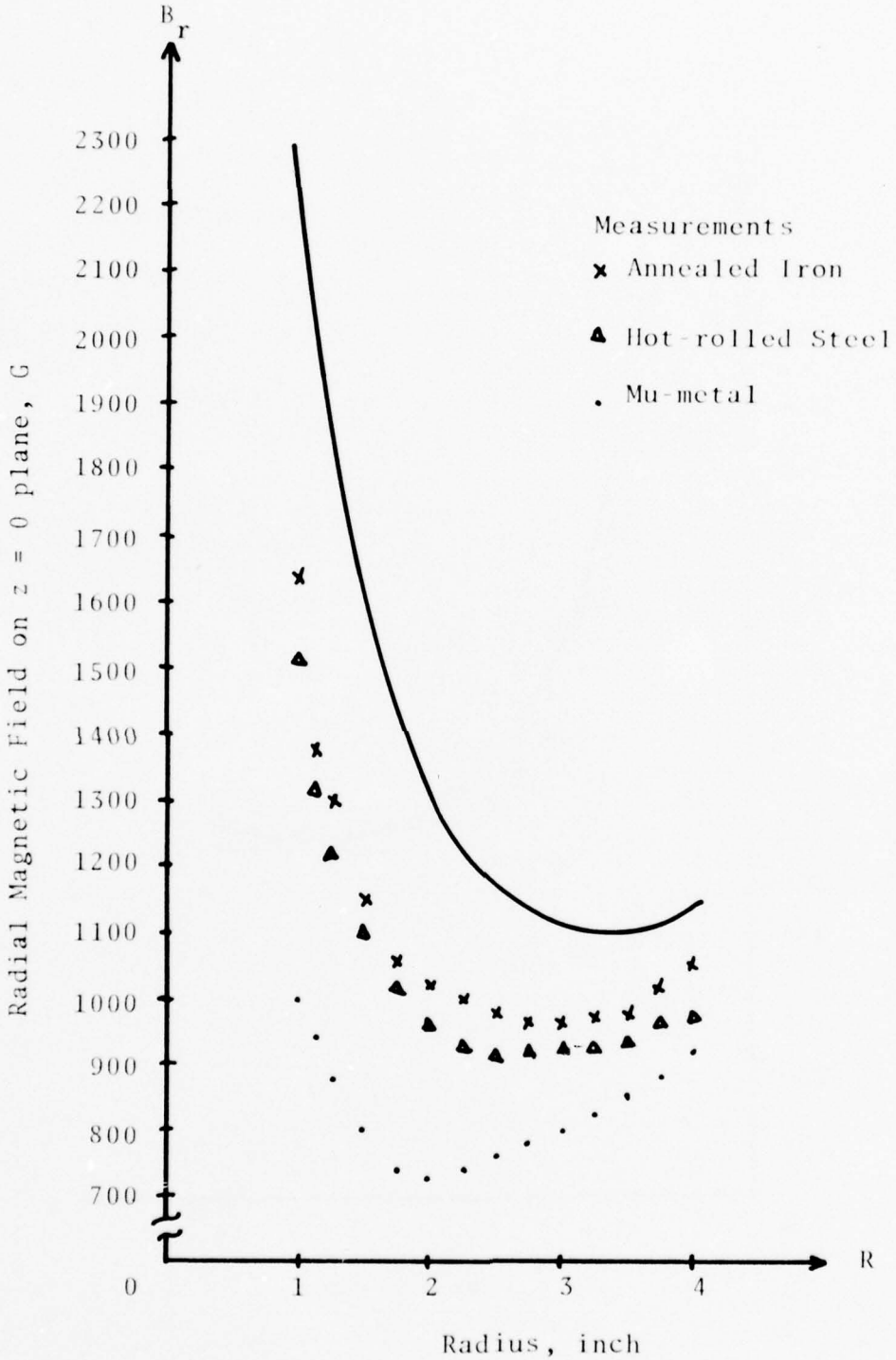

FIG. 17 MEASUREMENTS FOR CENTER POLE PIECES OF DIFFERENT MATERIALS. (SOLID LINE SHOWS THEORETICAL RESULTS; CURRENT LEVELS IN THE THREE SECTIONS OF COIL ARE 3.4 A, 3.8 A, 2.7 A)

of the center pole piece. For the current levels used in Fig. 15, an increase of diameter from 1.0 to 1.5 inch is sufficient to avoid saturation. However, it will be seen later in Section IV that the actual magnetic field of Fig. 14 obtained with current levels of 3.4 A, 3.8 A, 2.7 A will be strong enough to focus the electron beam of 1.2 A total beam current.

F. Cathode Curvature Calculation

As mentioned in Section II, the deformable mesh technique is particularly suitable for analyzing configurations with curved cathode or grids. In order to improve beam focusing, the field can be shaped correspondingly so that the emitting surface is approximately normal to the field lines as shown in Fig. 18. The radius of curvature of the cathode may be determined by the magnetic fields calculated or measured.

For a symmetrical focusing structure, only radial magnetic field components exist on the center line. Thus, it can be seen that $B_z(r,0) = 0$. Expand $B_z(r,z)$ in a Taylor series about the $z = 0$ plane as

$$B_z(r,z) \cong B_z(r,0) + z\frac{\partial B_z(r,0)}{\partial z} + \ldots \qquad (22)$$

Then $\partial B_z(r,0)/\partial z$ may be found from the condition $\nabla \cdot \bar{B} = 0$ in cylindrical coordinates:

$$\nabla \cdot \bar{B}(r,0) = \frac{1}{r}\frac{\partial}{\partial r}(rB_r) + \frac{\partial B_z}{\partial z} = 0 \quad . \qquad (23)$$

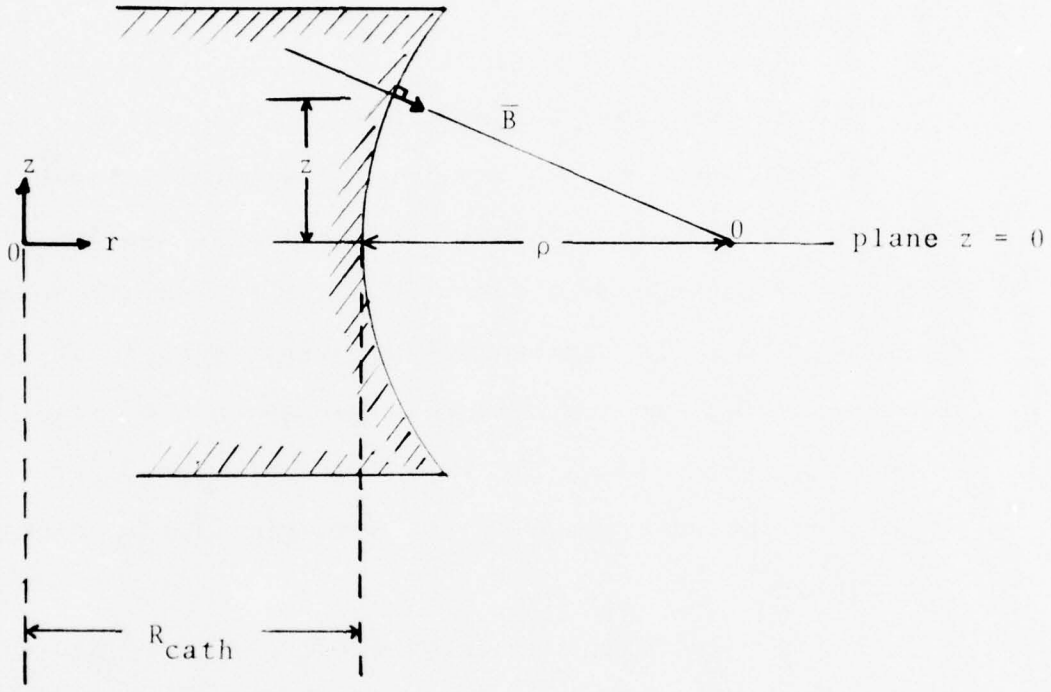

FIG. 18 CATHODE RADIUS OF CURVATURE CALCULATION.

Substituting Eq. 23 into Eq. 22 shows that

$$B_z \cong -\frac{z}{r}\left[\frac{\partial}{\partial r}(rB_r)\right]\Bigg|_{z=0} \quad . \tag{24}$$

From Fig. 18, the radius of curvature of cathode, ρ, is given by

$$\frac{\rho}{z} = \frac{B_r}{B_z}$$

or

$$\rho = -\frac{(rB_r)}{\partial/\partial r(rB_r)}\Bigg|_{z=0} \quad . \tag{25}$$

Here B_r is the value measured on the axis $z = 0$ at the radial position of the cathode.

From the measured results given in Sections III.D and E, the cathode radius of curvature calculated from Eq. 25 is usually quite large (about 5.0 inches) and consequently a flat cathode will be adequate.

G. Conclusions

In this section, an electromagnet design computer program was described and applied to manipulate the radial magnetic fields in an effort to approximate an ideal RBTWT field shape. The measurements agree very well with the theoretical results for low currents and low magnetic fields. For high current levels, saturation of the center pole piece restricts the increase of magnetic field. A magnetic material with higher saturation or a larger cross-sectional area must be used for the center pole piece if a higher magnetic field is necessary. The cathode radius of curvature has been calculated from the magnetic field measured and found to be large enough to permit

use of a flat surface. The results will be used in the following sections.

SECTION IV. DESIGN OF ELECTRON GUN

A. Introduction

In this section, a radial beam electron gun design through computer simulation will be presented. First of all, it is necessary to determine the initial parameters of the beam. Prior to fabrication of the gun, the shapes and positions of the electrodes, cathode and anode have to be chosen and optimized. The magnetic fields obtained in Section III for different current levels in the three sections of coil will be evaluated and a final current level will be selected for operation of the experimental gun.

The objective specifications for the experimental tube are as follows:

Frequency	0.5 to 1.0 GHz
Beam voltage	1,000 V
Beam current	1.2 A
Beam power	1.2 kW
Cathode current density	0.7 to 2.5 A/cm^2
Cathode radius	1.0 in. (2.54 cm)
Length of drift space (from cathode surface to collector surface)	3.0 in. (7.62 cm)
Spacing between ceramic substrate	0.05 in. (0.127 cm)

In the following sections, the design procedures will be presented. The effects of geometric parameters will be discussed. Figure 19 shows the definitions of these parameters. The voltages at cathode, electrode and anode are specified as V_c, V_e and V_a, respectively.

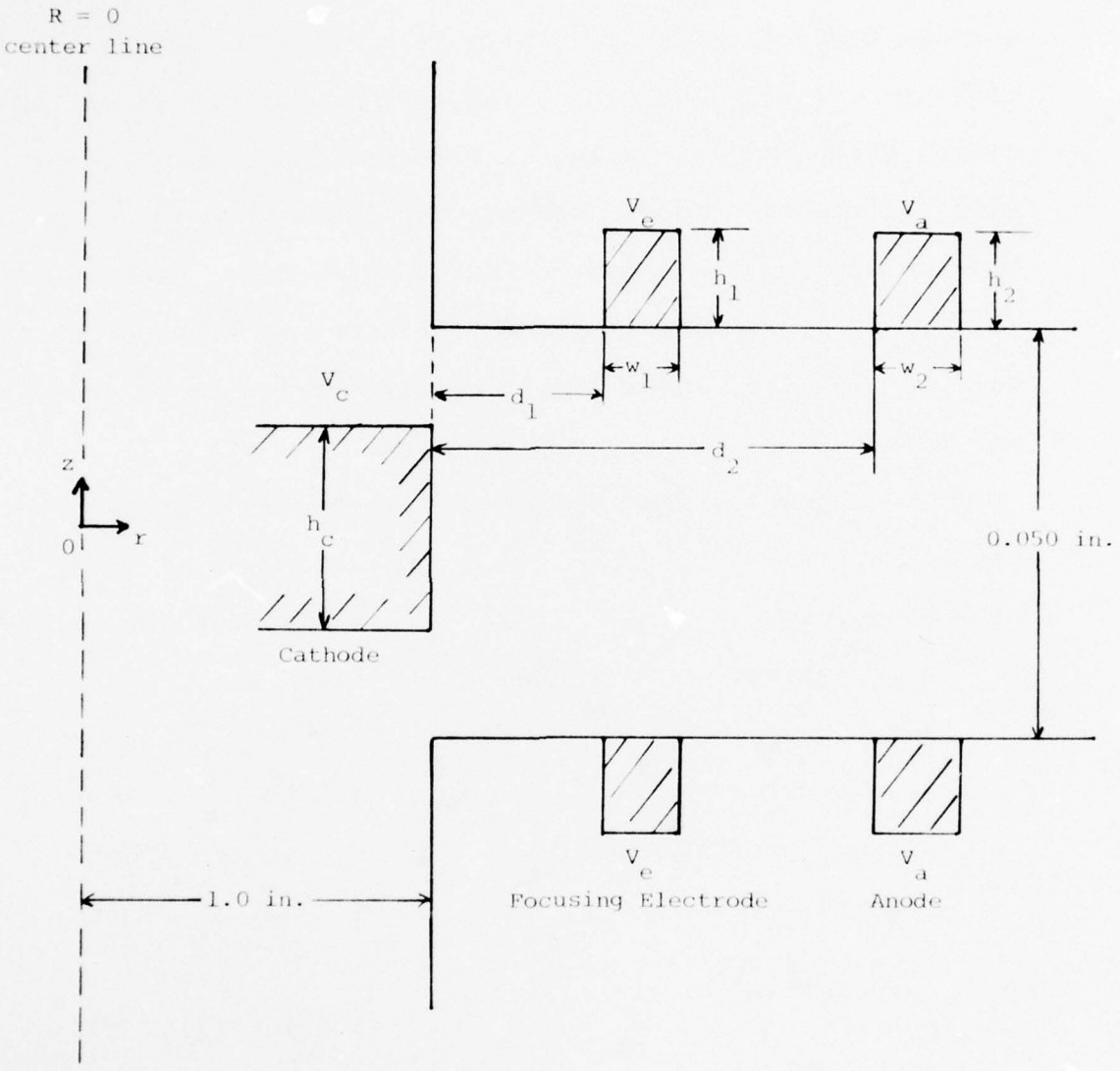

FIG. 19 GEOMETRIC PARAMETERS OF ELECTRON GUN.

The experimental tube actually built was based on the final design outlined in this section.

B. Beam-Filling Factor and Cathode Shape

The first parameter to be determined in the electron gun design is the beam-filling factor. A very thin beam is desirable to give good transmission, while a thick beam improves RF interaction. Past experience with O-type guns suggests a nominal beam-filling factor of about 0.5 or a beam thickness of 0.025 in. for a circuit spacing of 0.050 in. The shape and height of the cathode are the two primary parameters which affect the beam-filling factor.

Figures 20 through 22 show the electron trajectories for a curved cathode with height of 0.040 in., a flat cathode with height of 0.040 in. and a flat cathode with height of 0.025 in. The magnetic field is 1,925 G at the cathode surface and decreases ideally as $1/\sqrt{R}$ as shown in Fig. 23. Only the top half of the gun is shown here since the bottom half is just a mirror image of the top half.

Mesh plots corresponding to Figs. 20 and 22 are shown in Figs. 24a and b. Other parameters used in these calculations are: for cathode, $V_c = 0$ V; for focusing electrode, $d_1 = 0.0075$ in., $w_1 = 0.01$ in., $h_1 = 0.01$ in. and $V_e = 0$ V; for anode, $d_2 = 0.1$ in., $w_2 = 0.01$ in., $h_2 = 0.01$ in. and $V_a = 1{,}000$ V.

As mentioned in Section III.F, a flat cathode is suitable for the present magnetic focusing structure. A comparison of Figs. 20 and 21 makes this even more evident. Figure 22

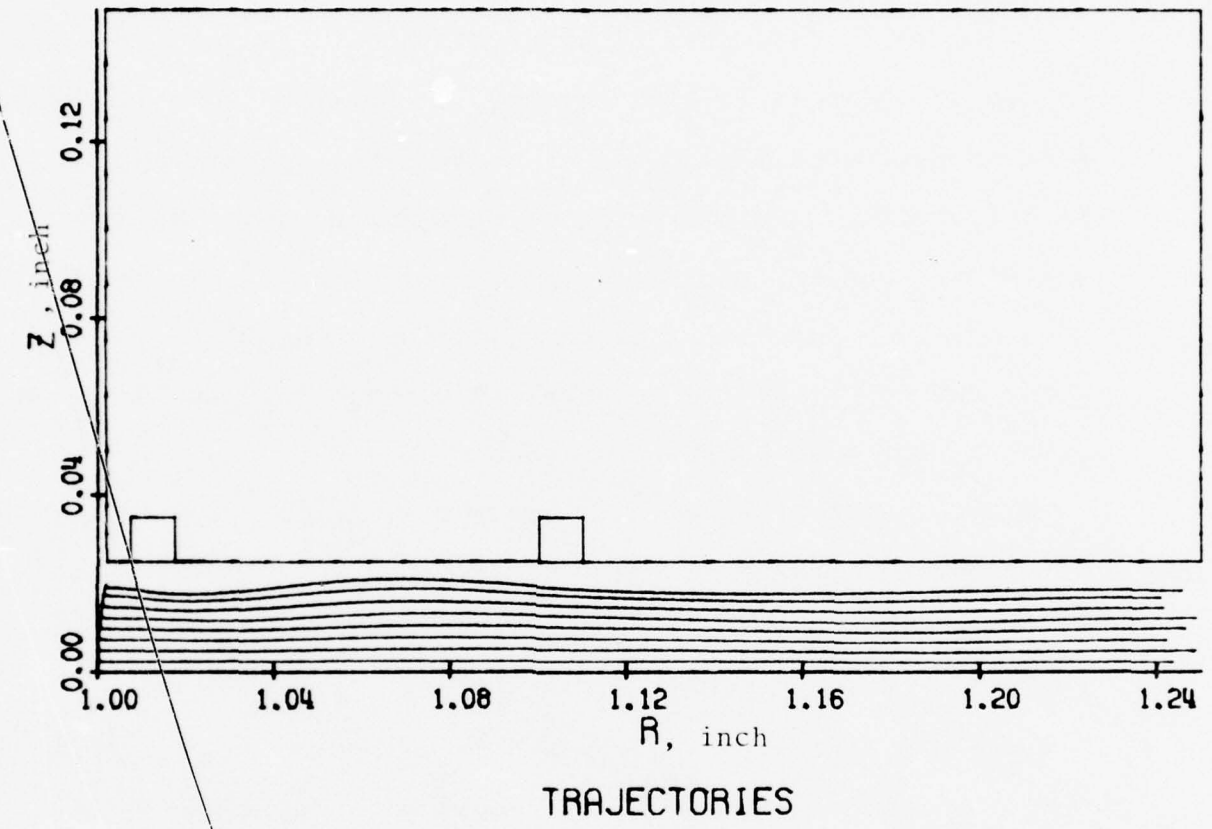

FIG. 20 TRAJECTORIES PLOT FOR A CATHODE WITH HEIGHT h_c = 0.040 IN., RADIUS OF CURVATURE = 0.1 IN.

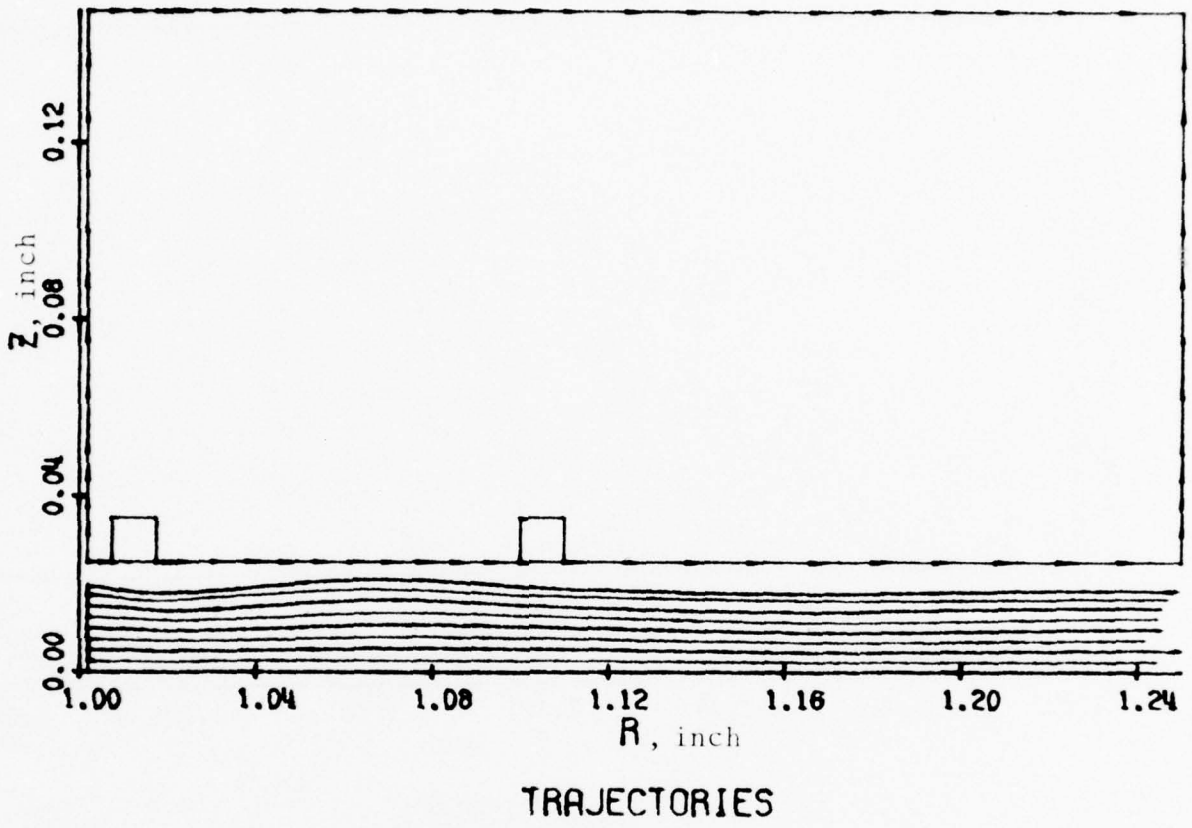

FIG. 21 TRAJECTORIES PLOT FOR A FLAT CATHODE WITH HEIGHT h_c = 0.040 IN.

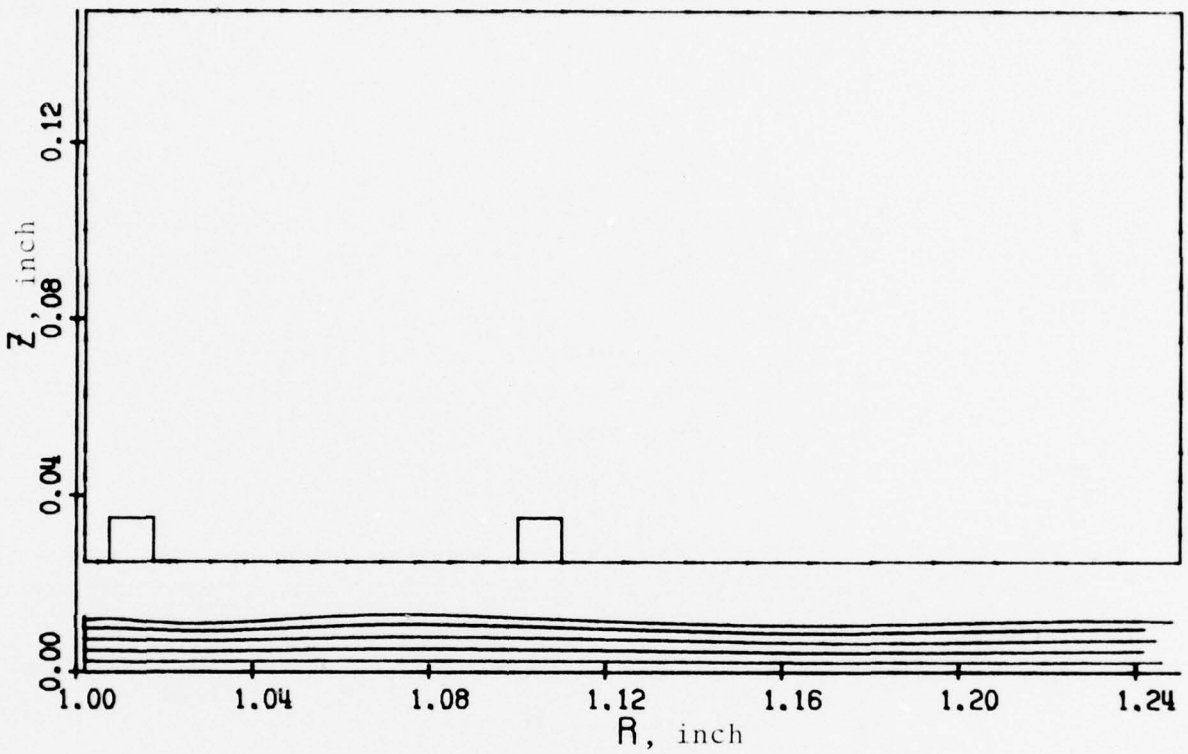

FIG. 22 TRAJECTORIES PLOT FOR A FLAT CATHODE OF HEIGHT h_c = 0.025 IN.

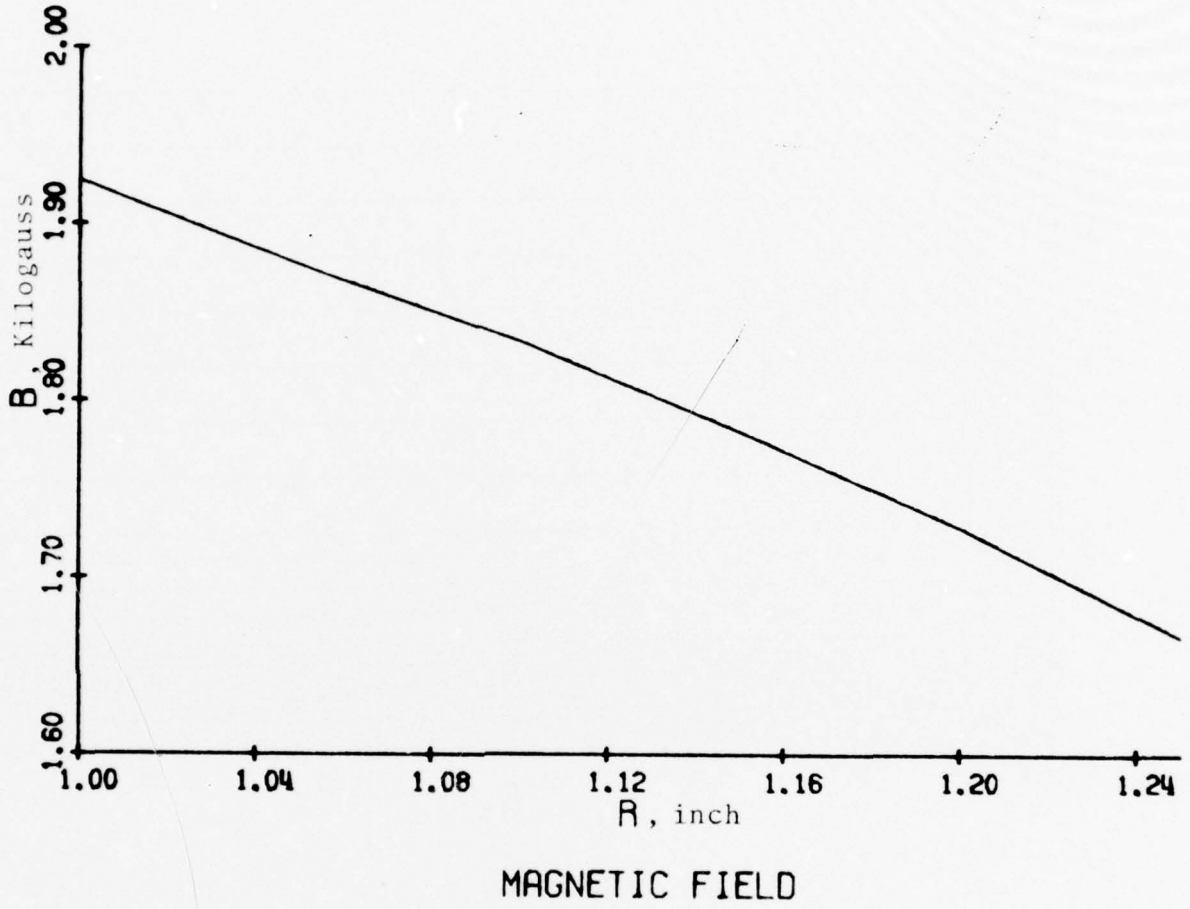

FIG. 23 MAGNETIC FIELD USED FOR THE CALCULATIONS IN FIGS. 20 THROUGH 22.

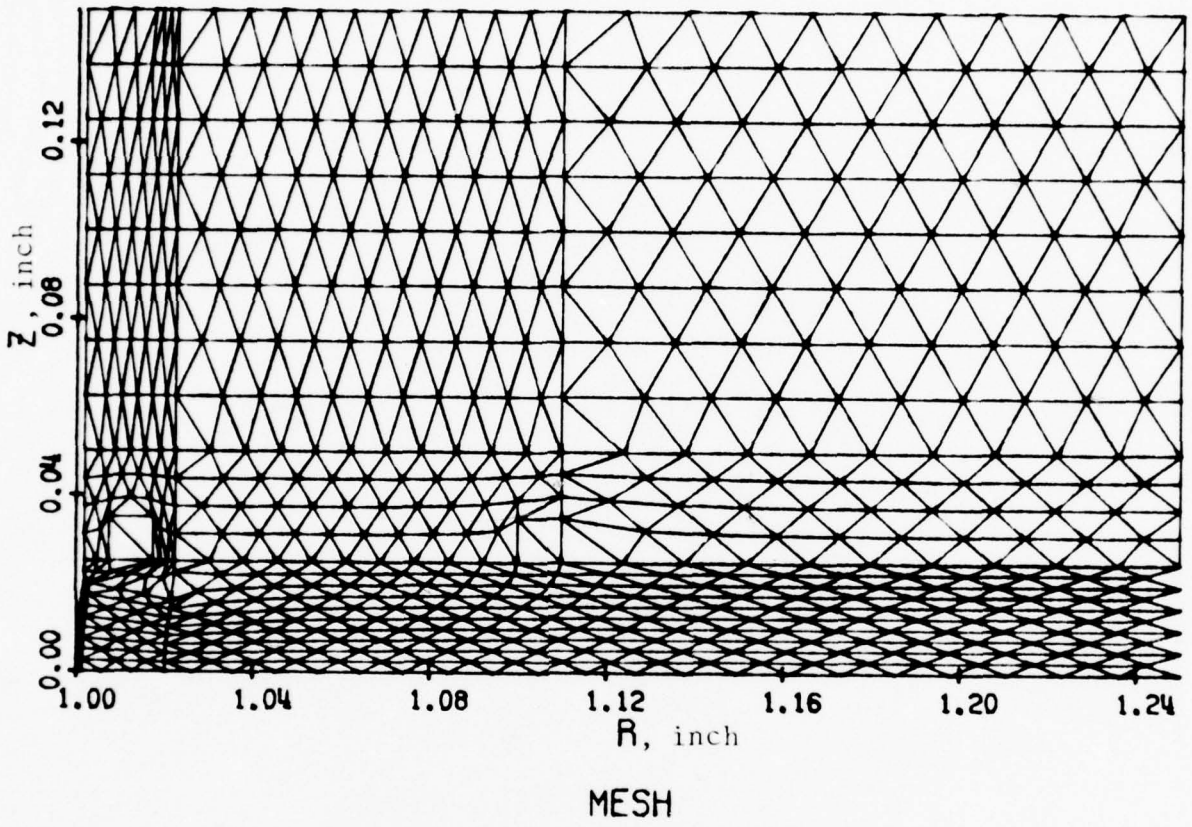

FIG. 24a MESH PLOT OF FIG. 20.

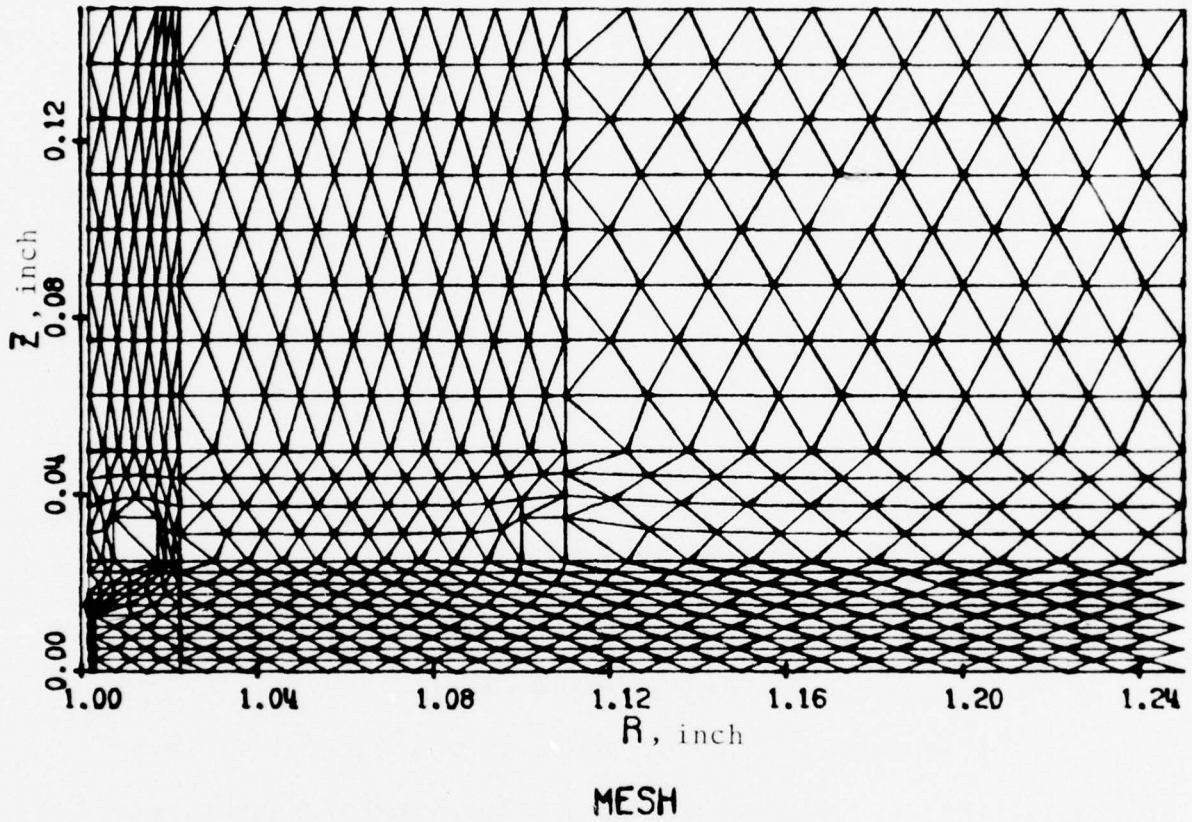

FIG. 24b MESH PLOT OF FIG. 22.

shows that a beam-filling factor of 0.5 may be achieved simply by using a flat cathode with height of 0.025 in.

C. Voltage and Position of the Focusing Electrode

Once the cathode size and shape have been chosen, the positions of the electrodes will be adjusted to obtain the required beam current. For the case where the anode is maintained at 1,000 V and placed 0.1 in. from the cathode (i.e., in Fig. 19, V_a = 1,000 V, d_2 = 0.1 in., w_2 = 0.01 in. and h_2 = 0.01 in.), the cathode current density and total current are shown in Figs. 25 through 28. In these figures, the position of the focusing electrode is varied. The other parameters are: cathode, unshaped, h_c = 0.025 in., V_c = 0 V; electrode, w_1 = 0.01 in, h_1 = 0.01 in. and V_e = 0 V. The magnetic field is not important since it has little or no effect on the cathode current density.

It is interesting to note that the current is very sensitive to the position of the focusing electrode. As the electrode moves closer to the cathode, the current increases sharply as expected. The design without a focusing electrode results in a very high current as seen in Fig. 28. With no electrode to shield the effects of the anode, the electric field at the cathode is very high.

Obviously, the position of the focusing electrode has to be precisely machined in order to control the required beam current.

The beam current is also very sensitive to the voltage of the focusing electrode. With the voltages and geometries

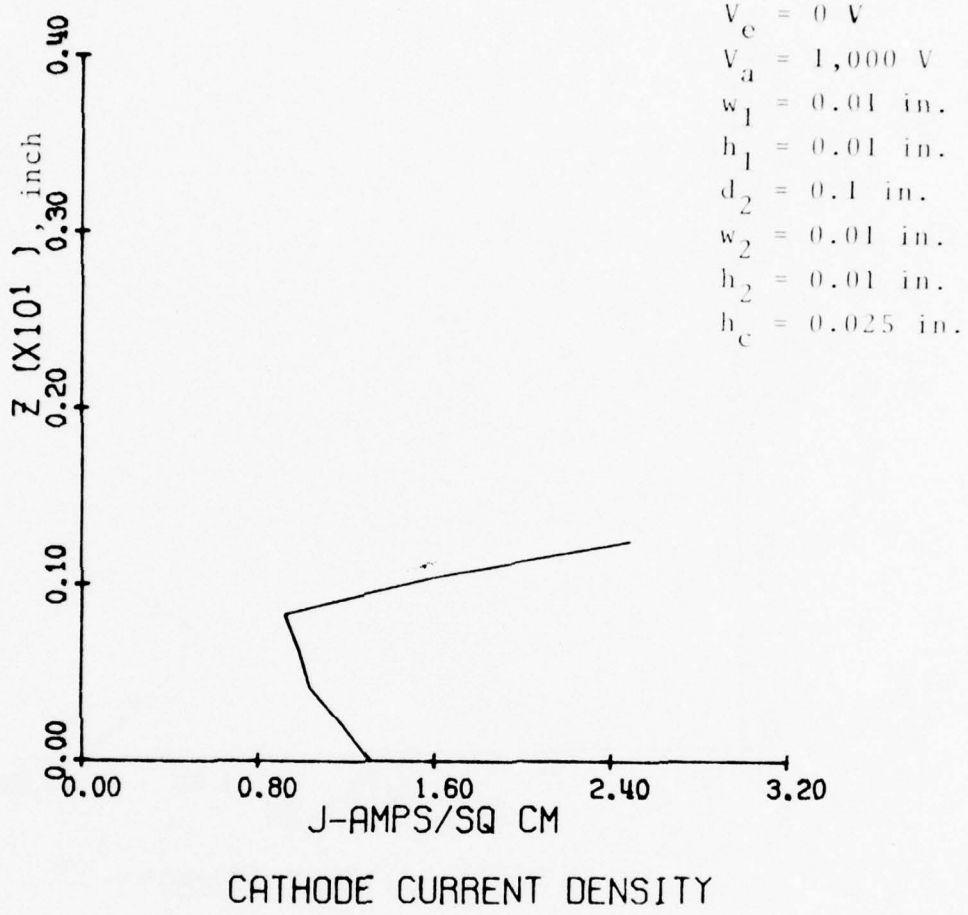

FIG. 25 CATHODE CURRENT DENSITY AS A FUNCTION OF Z FOR d_1 = 0.01 IN.

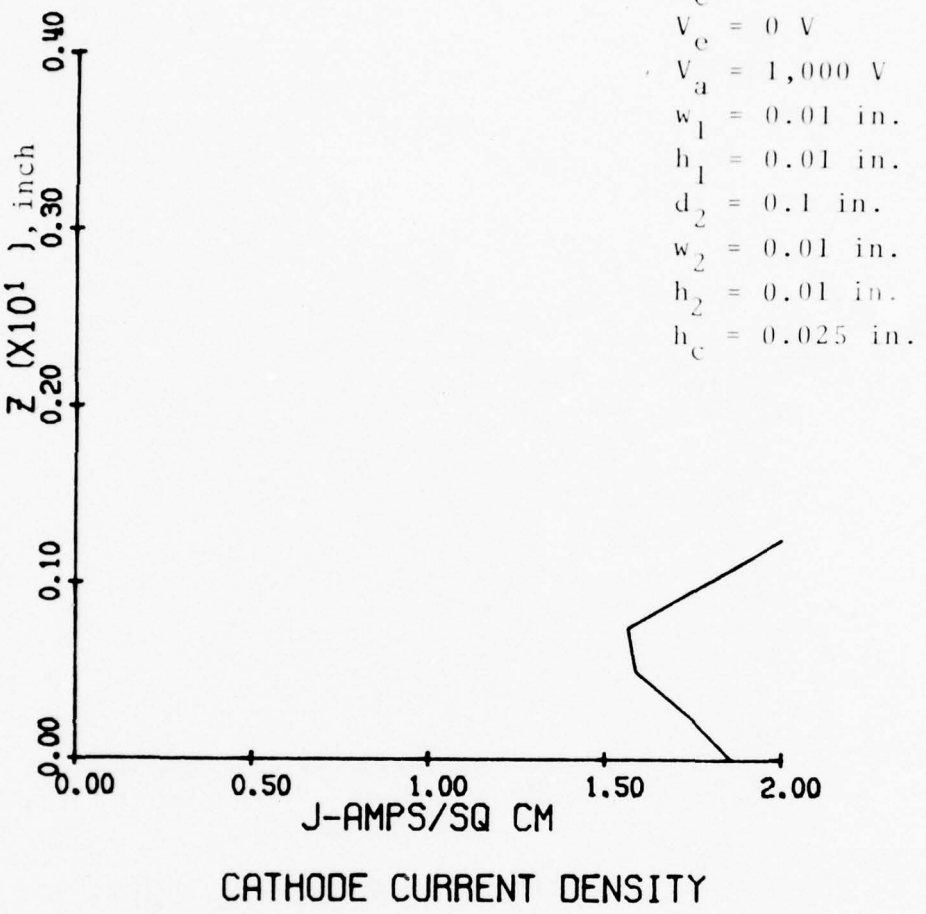

Total Current = 1.74 A
Perveance = 55 μpervs

FIG. 26 CATHODE CURRENT DENSITY AS A FUNCTION OF Z FOR d_1 = 0.0075 IN.

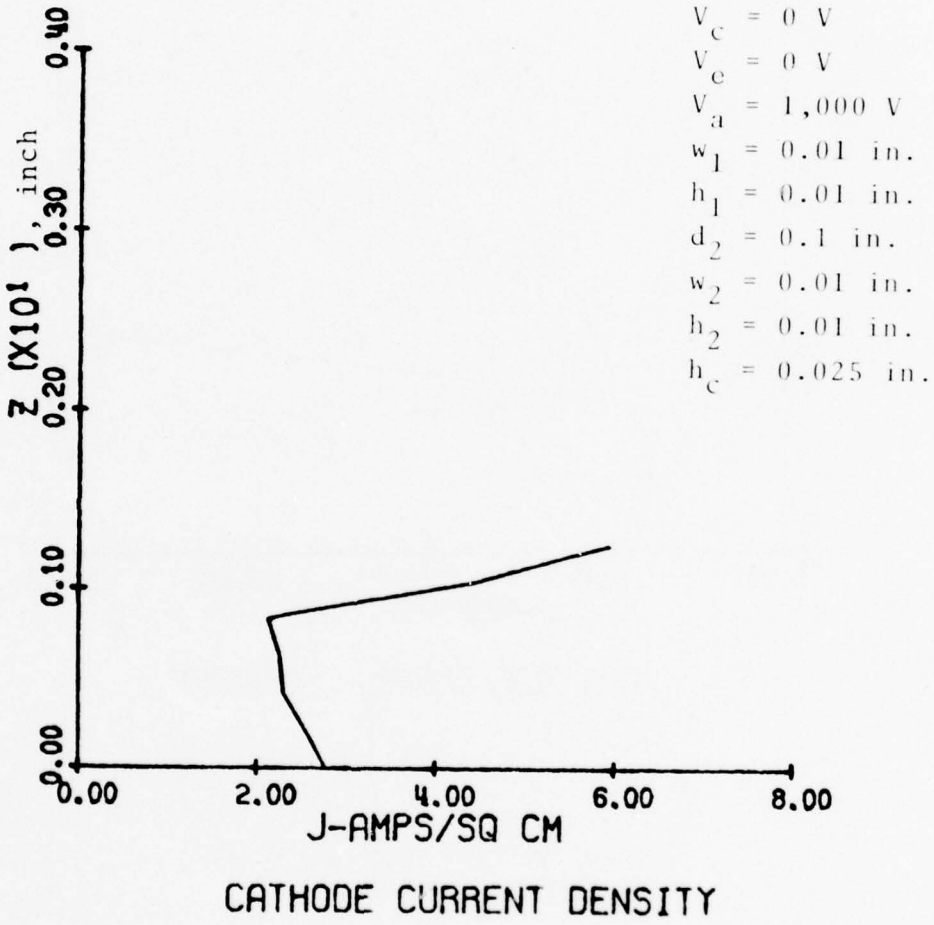

FIG. 27 CATHODE CURRENT DENSITY AS A FUNCTION OF Z FOR d_1 = 0 IN.

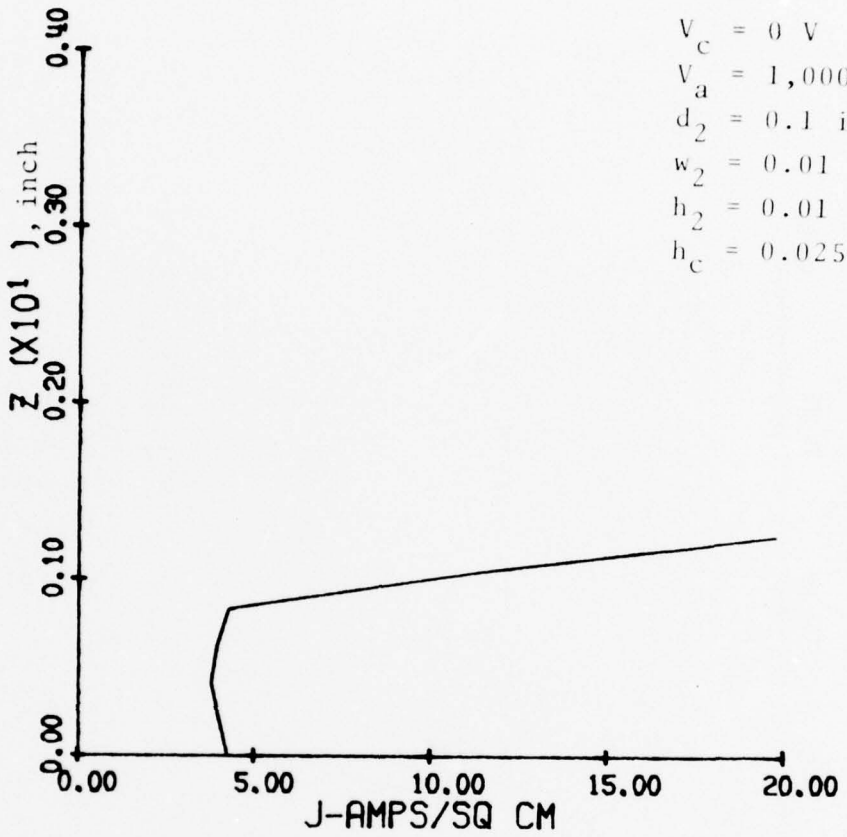

Total Current = 6.58 A
Perveance = 208 μpervs

FIG. 28 CATHODE CURRENT DENSITY AS A FUNCTION OF Z (NO ELECTRODE IN THIS CALCULATION).

of cathode and anode left unchanged and the electrode placed at d_1 = 0.01 in., cathode current density plots corresponding to electrode voltages of 50 V and -50 V are shown in Figs. 29 and 30 for comparison.

D. Voltage and Position of the Anode

From Child's law, it is evident that the cathode current will rise as the anode voltage is increased or as the anode is moved toward the cathode. Figures 31 through 34 confirm this. In Figs. 31 and 32, the parameters used are: for cathode, flat with height h_c = 0.025 in. and V_c = 0 V; for electrode, d_1 = 0 in., w_1 = 0.01 in., h_1 = 0.01 in. and V_e = 0 V; for anode, d_2 = 0.1 in. for Fig. 31 and 0.16 in. for Fig. 32, w_2 = 0.01 in., h_2 = 0.01 in. and V_a = 1,000 V. In Figs. 33 and 34 the following parameters are used: for cathode, flat with height h_c = 0.025 in. and V_c = 0 V; for electrode, d_1 = 0.01 in., w_1 = 0.01 in., h_1 = 0.01 in. and V_e = 0 V; for anode, d_2 = 0.1 in., w_2 = 0.01 in., h_2 = 0.01 in. and V_a = 900 V in Fig. 33 and 1,100 V in Fig. 34.

E. Gun Design I

From the discussions in Sections IV.B through IV.D, a final design for an electron gun with required current density and total beam current may be selected as follows:

for cathode flat surface,

h_c = 0.025 in.,

V_c = 0 V,

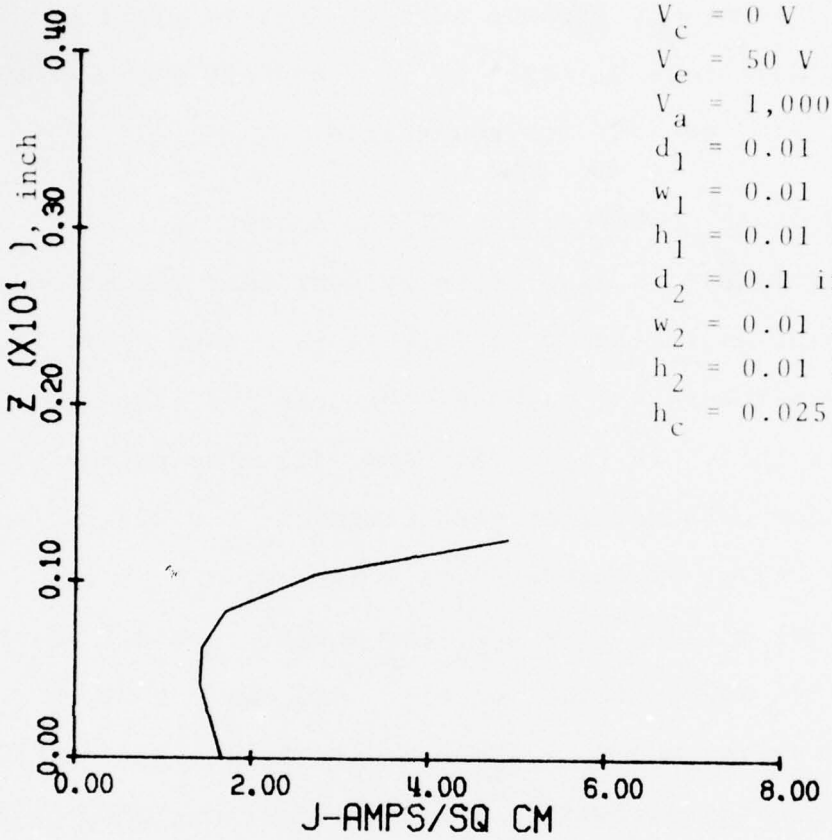

Total Current = 2.03 A
Perveance = 64 μpervs

FIG. 29 CATHODE CURRENT DENSITY AS A FUNCTION OF Z FOR V_e = 50 V.

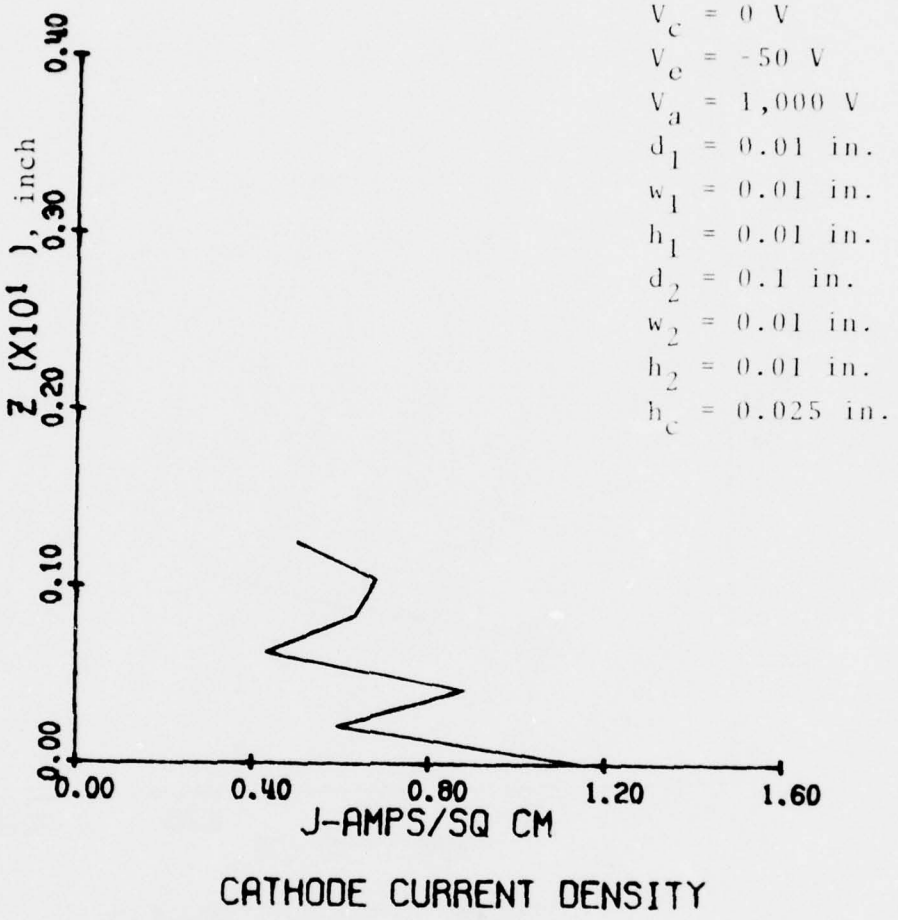

Total Current = 0.68 A
Perveance = 21.5 μpervs

FIG. 30 CATHODE CURRENT DENSITY AS A FUNCTION OF Z FOR V_e = -50 V.

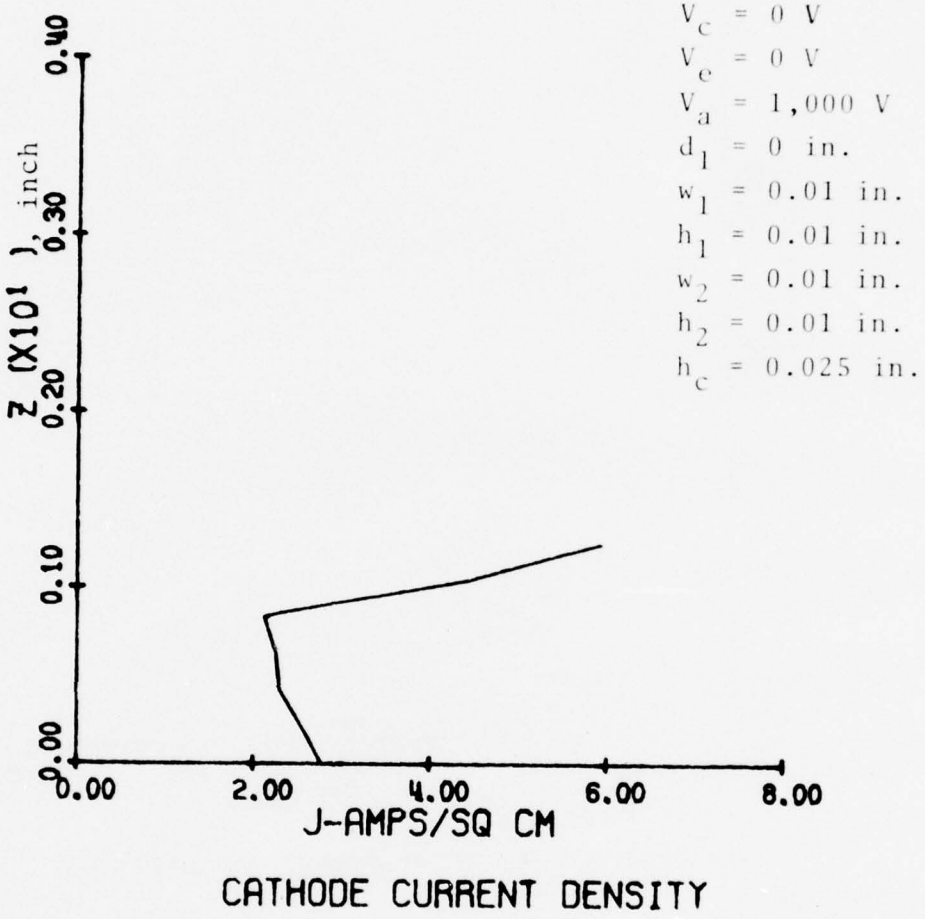

Total Current = 3.03 A
Perveance = 96 μpervs

FIG. 31 CATHODE CURRENT DENSITY AS A FUNCTION OF Z FOR d_2 = 0.1 IN.

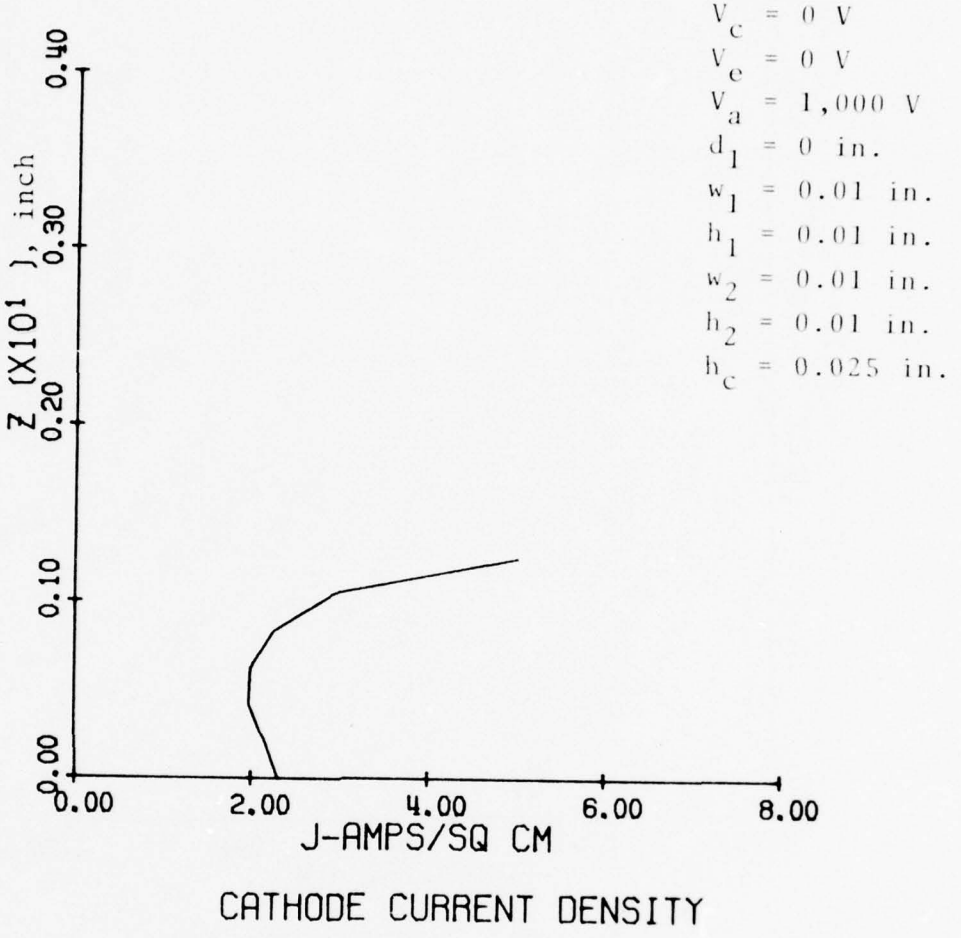

Total Current = 2.54 A
Perveance = 80 μpervs

FIG. 32 CATHODE CURRENT DENSITY AS A FUNCTION OF Z FOR d_2 = 0.16 IN.

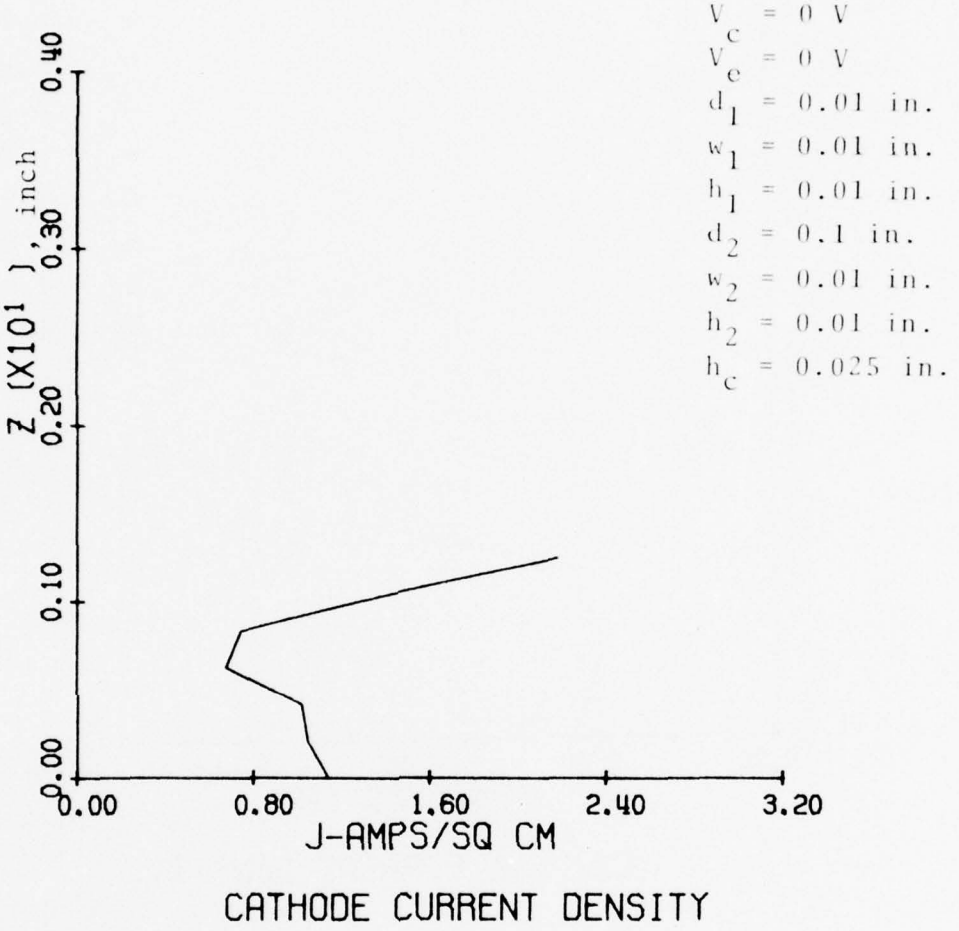

FIG. 33 CATHODE CURRENT DENSITY AS A FUNCTION OF Z FOR V_a = 900 V.

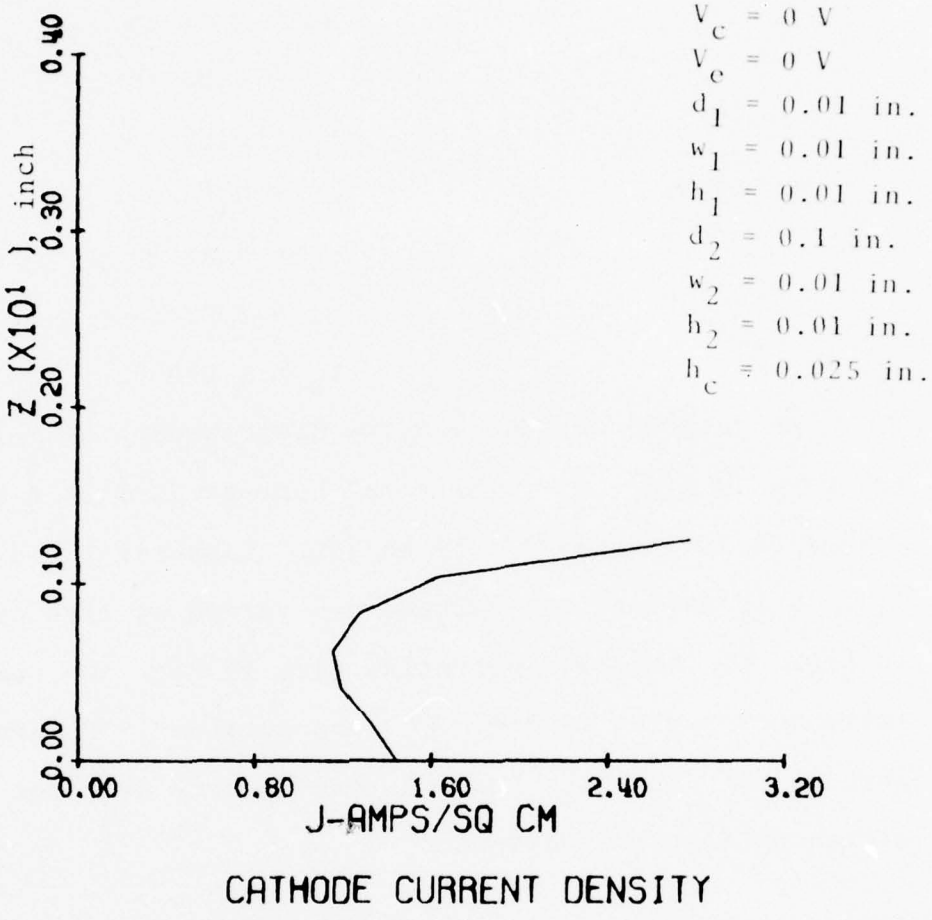

FIG. 34 CATHODE CURRENT DENSITY AS A FUNCTION OF Z FOR V_a = 1,100 V.

for focusing electrode $d_1 = 0.01$ in.,

$w_1 = 0.01$ in.,

$h_1 = 0.01$ in.,

$V_e = 0$ V,

for anode $d_2 = 0.1$ in.,

$w_2 = 0.01$ in.,

$h_2 = 0.01$ in.,

$V_a = 1{,}000$ V.

The cathode current density distribution of this design is shown in Fig. 25. The total current is 1.28 A and the perveance is 40 μpervs. If an ideal magnetic field of 2,000 G is used at the cathode and varied as $1/\sqrt{R}$ as shown in Fig. 35, the equipotential plot in Fig. 36 and the trajectories plot in Fig. 37 are obtained. Figures 38 through 40 show the beam current density at three different distances from the cathode.

F. Beam Focusing and Magnetic Field

As described in Section III, the radial magnetic fields along the center line were measured for various current levels in the three-section coils. The particular current levels most suitable for final tube operation were determined through computer simulation.

Theoretically, a high magnetic field varying as $1/\sqrt{R}$ is desirable for focusing the beam. Using the specifications of Gun Design I as described in the last section, the trajectories of electrons for different applied magnetic fields are shown in Figs. 41 through 44. It is found that the

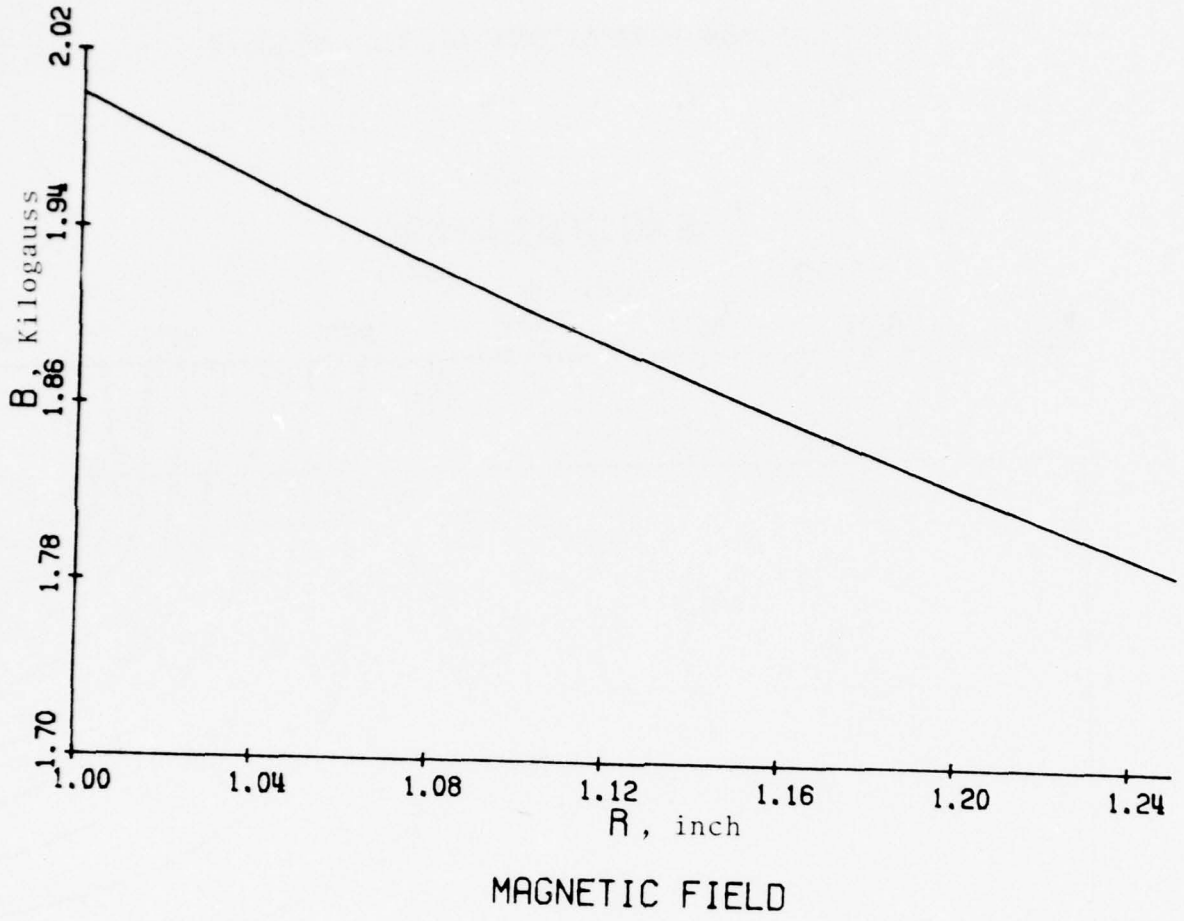

FIG. 35 IDEAL RBTWT MAGNETIC FIELD AS A FUNCTION OF R.

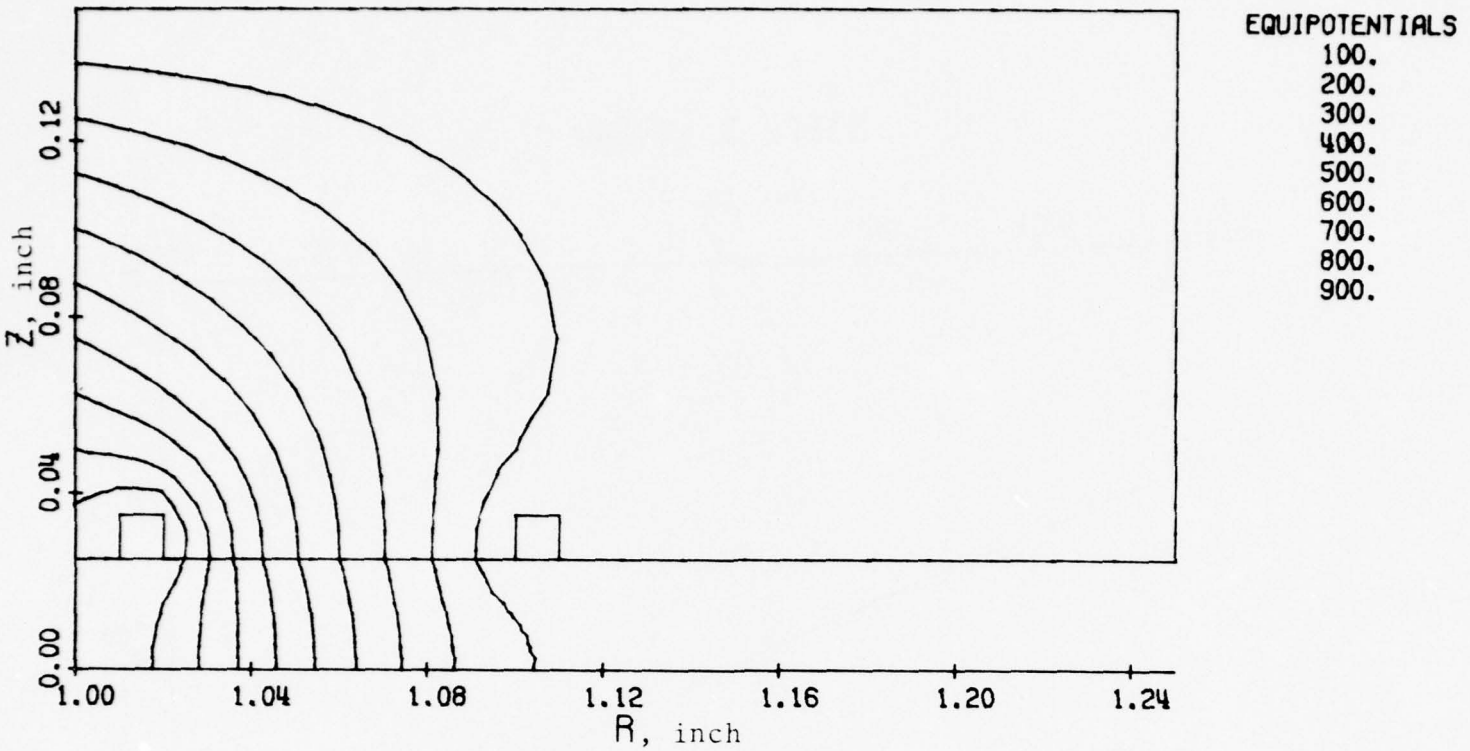

FIG. 36 EQUIPOTENTIAL PLOT FOR GUN DESIGN I.

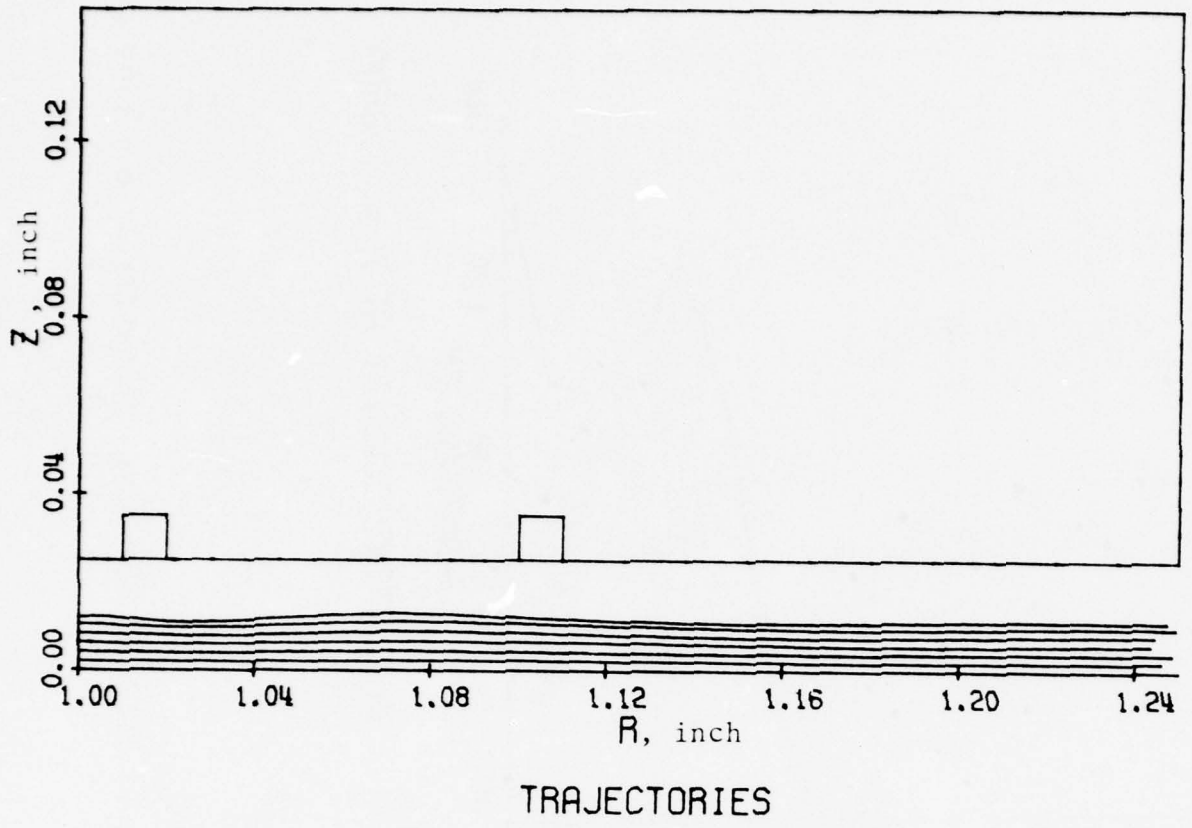

FIG. 37 TRAJECTORIES PLOT FOR GUN DESIGN I.

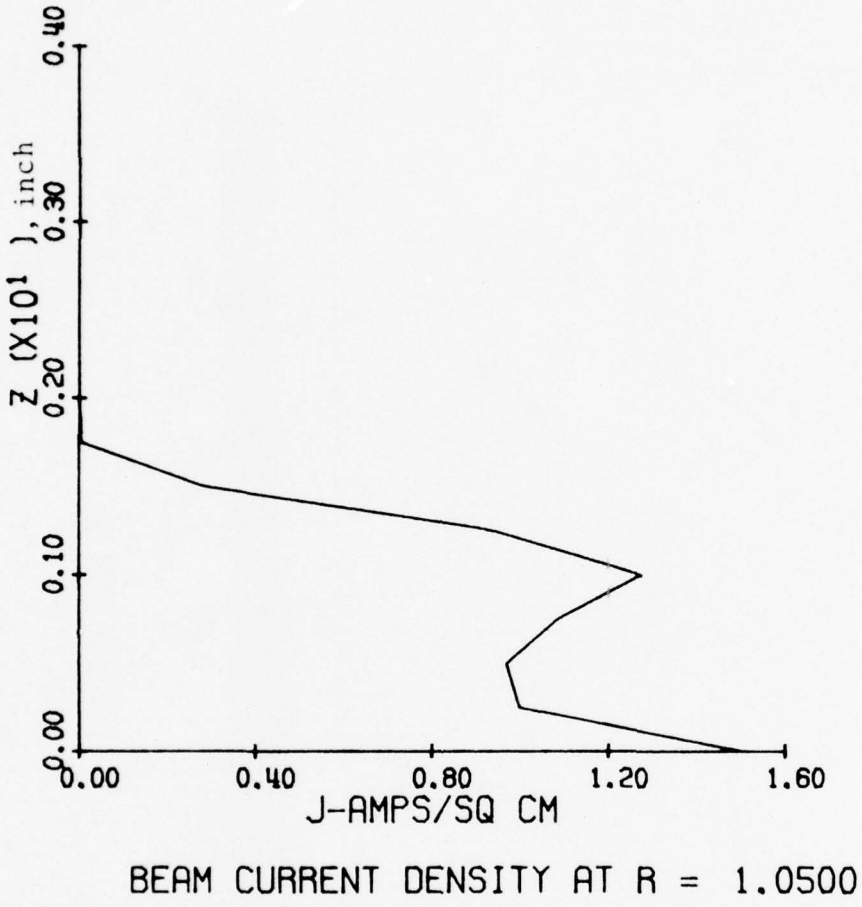

FIG. 38 CROSS-SECTION BEAM CURRENT DENSITY AT R = 1.05 IN.

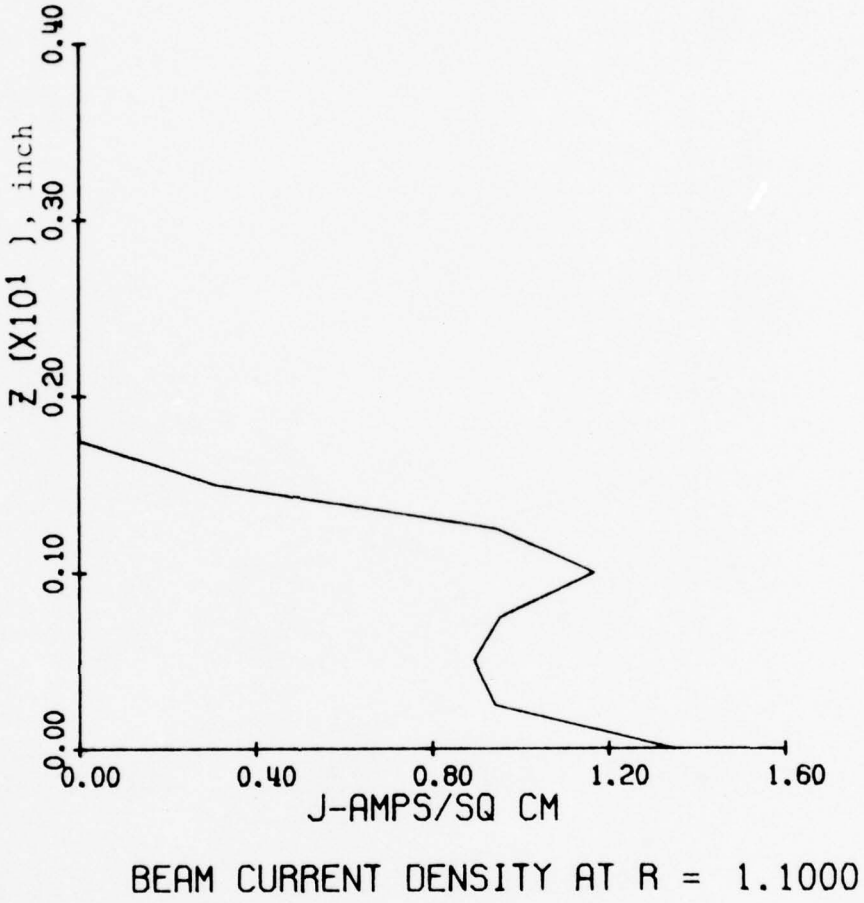

FIG. 39 CROSS-SECTION BEAM CURRENT DENSITY AT R = 1.1 IN.

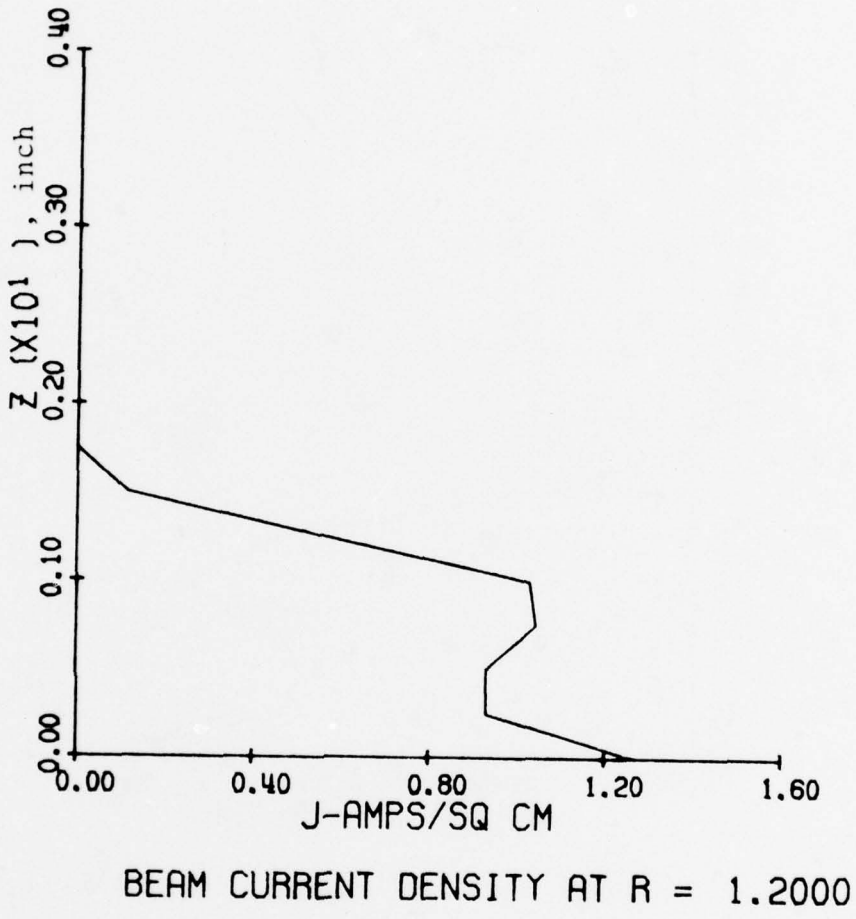

FIG. 40 CROSS-SECTION BEAM CURRENT DENSITY AT R = 1.2 IN.

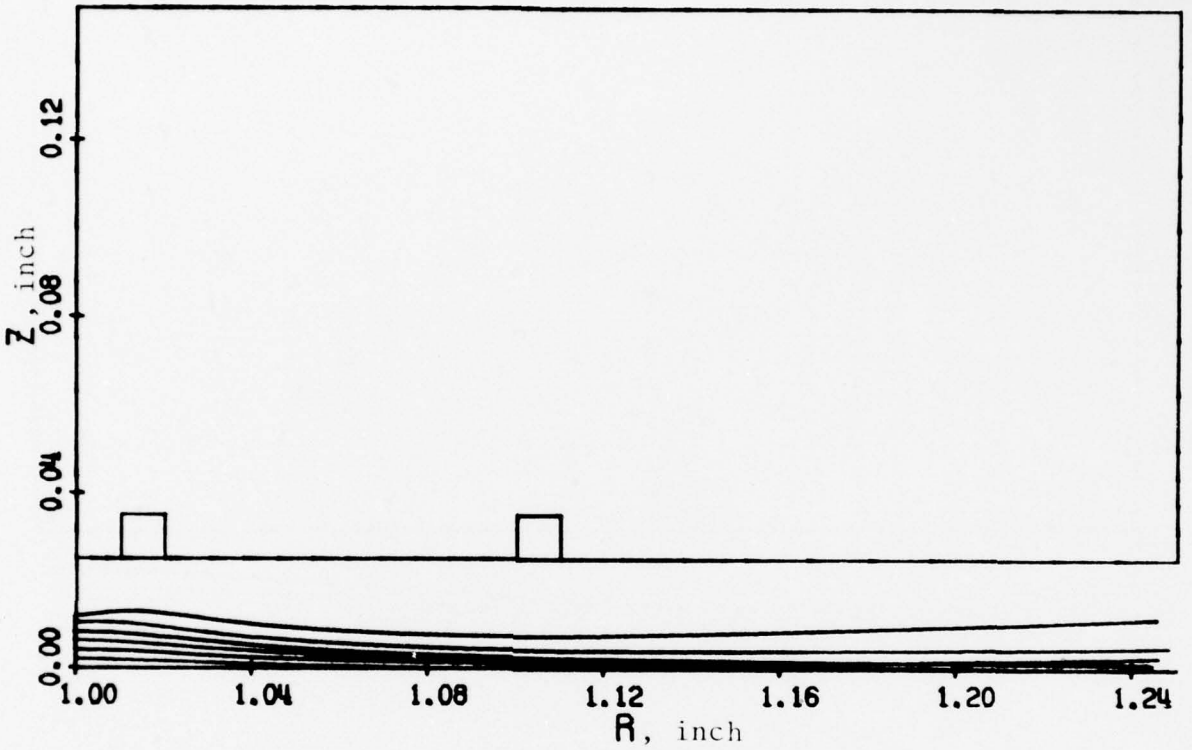

FIG. 41 BEAM TRAJECTORIES PLOT WITH NO MAGNETIC FIELD APPLIED TO THE GUN.

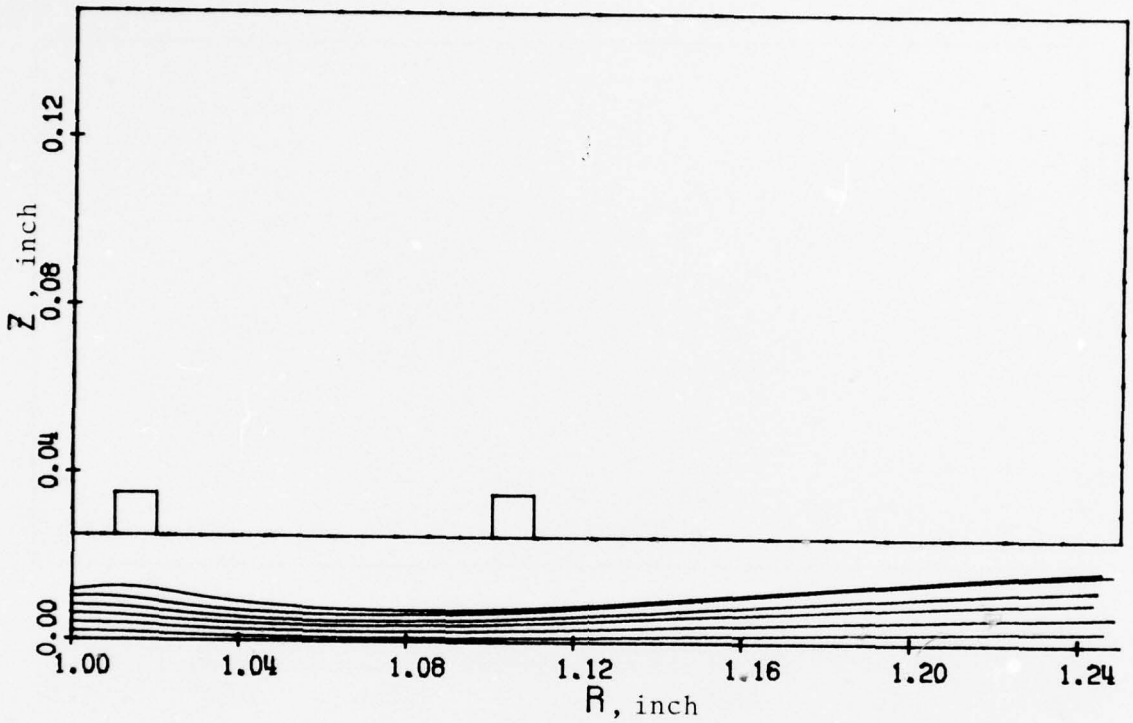

FIG. 42 BEAM TRAJECTORIES PLOT WITH MAGNETIC FIELD OF 500 G AT CATHODE.

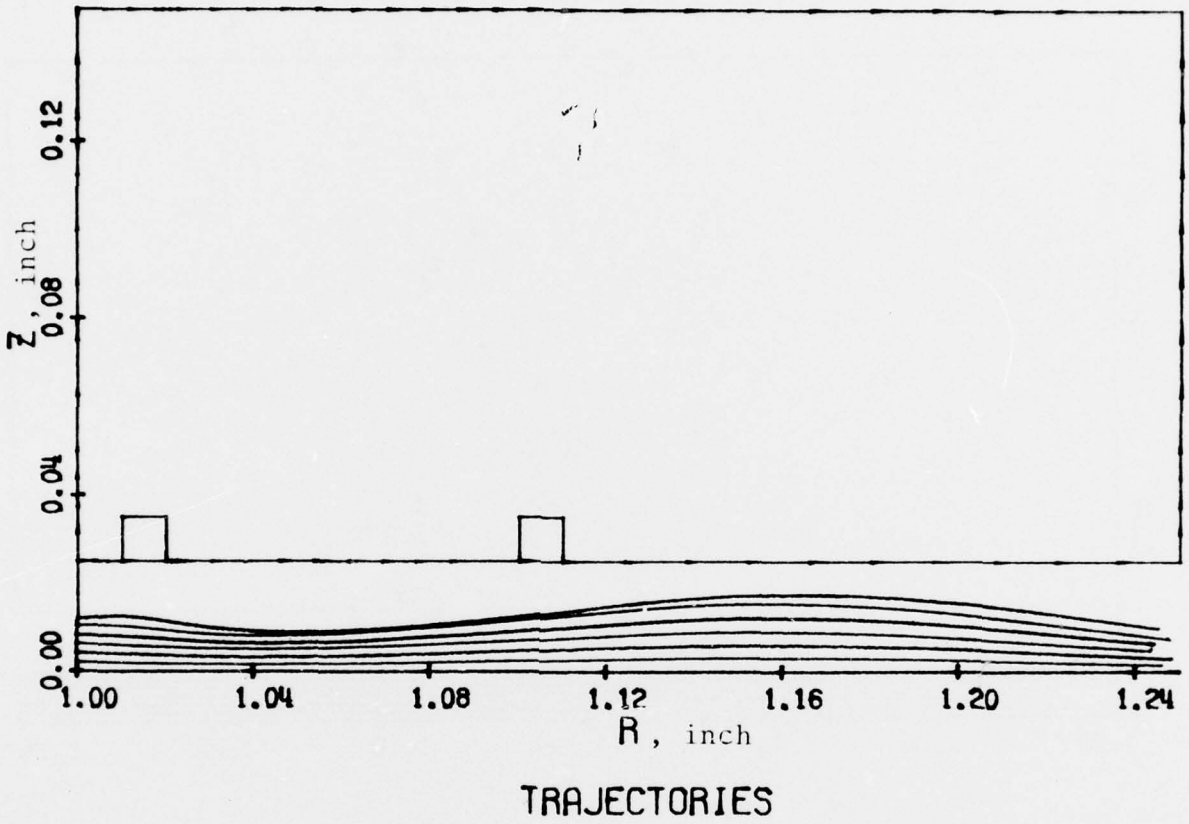

FIG. 43 BEAM TRAJECTORIES PLOT WITH MAGNETIC FIELD OF 1,000 G AT CATHODE.

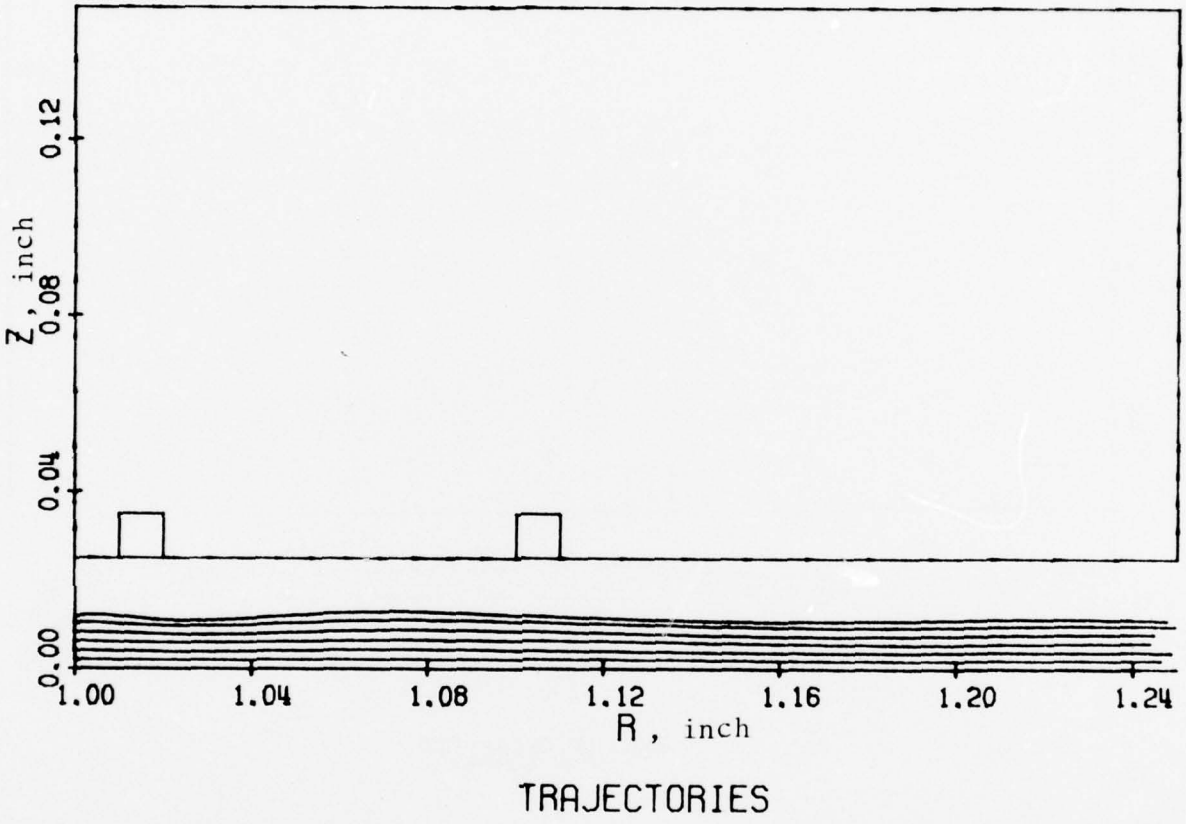

FIG. 44 BEAM TRAJECTORIES PLOT WITH MAGNETIC FIELD OF 2,000 G AT CATHODE.

peak of fluctuation of the beam shifts to the right (i.e., away from the cathode) as the magnetic field decreases. The reason is due to the change of the cyclotron frequency which is proportional to the magnetic field. No magnetic field is applied in Fig. 41. The magnetic fields used in Figs. 42, 43 and 44 are 500, 1,000 and 2,000 G at the cathode, respectively, and vary as $1/\sqrt{R}$. It is seen that a well focused beam is achieved in Fig. 44.

In practice, it is difficult to design the coils to give precisely a chosen field shape. Furthermore, the saturation of the center pole piece lowers the magnetic field in the cathode region. In order to confirm whether any of the magnetic fields actually obtained were sufficient to focus the beam, it was decided to conduct a thorough computer analysis extending all the way from the cathode to the collector. Figures 45 a and b show the computer results for the complete trajectories. The magnetic field values actually measured were used as input. The magnetic field used for Fig. 45a is that produced by current levels of 1.7 A, 1.9 A, 1.35 A in the coils and is plotted in Fig. 10. The field for Fig. 45b is shown in Fig. 14 and was obtained with current levels of 3.4 A, 3.8 A, 2.7 A. It is interesting to note that the beam converges as it approaches the collector.

On the basis of these plots, it was concluded that the magnetic field generated by the current levels of 3.4 A, 3.8 A, 2.7 A in the three sections of coil is enough to focus the beam.

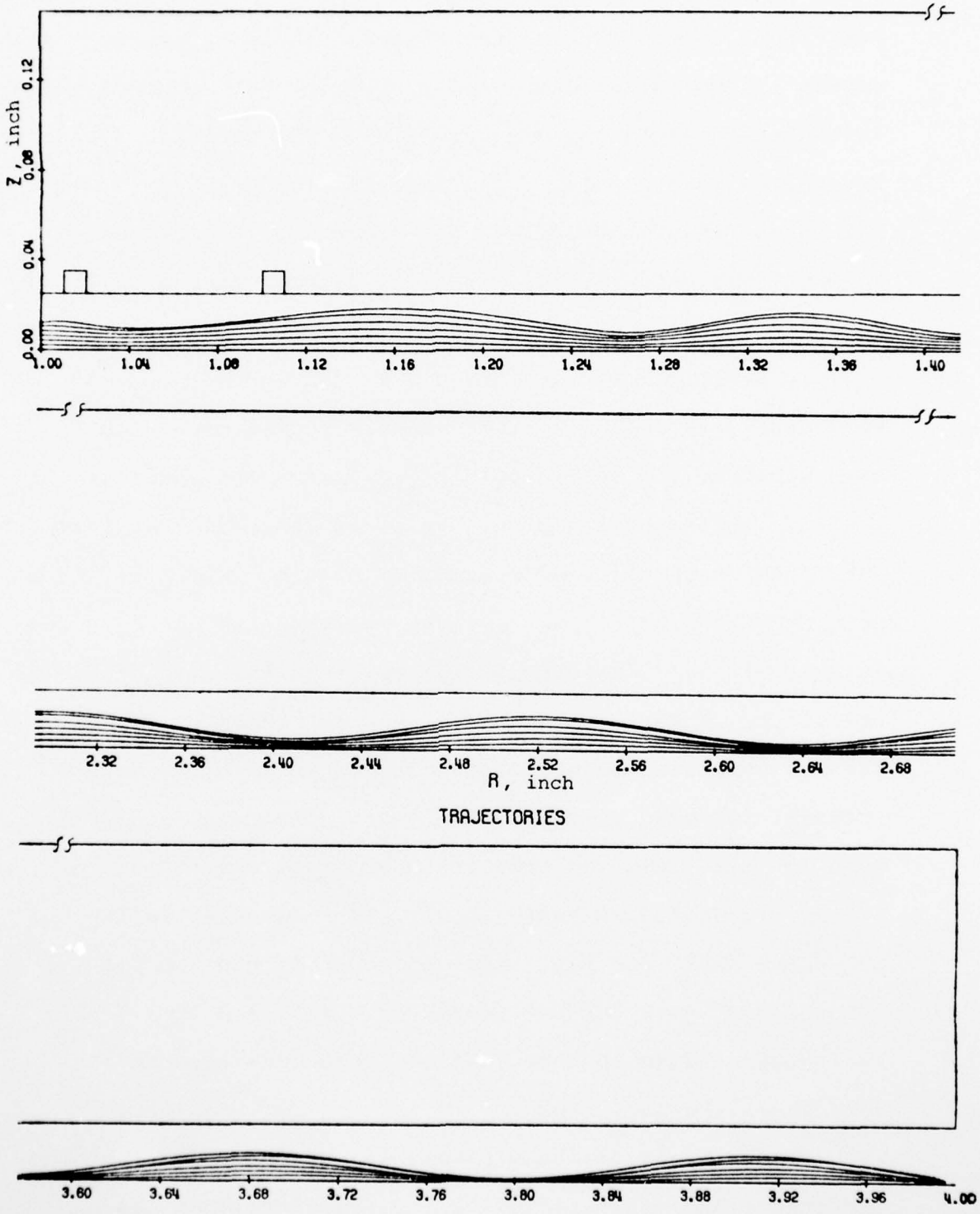

FIG. 45a BEAM TRAJECTORIES PLOT FOR A MAGNETIC FIELD WITH CURRENT LEVELS IN THREE SECTIONS OF COIL AS 1.7 A, 1.9 A, 1.35 A.

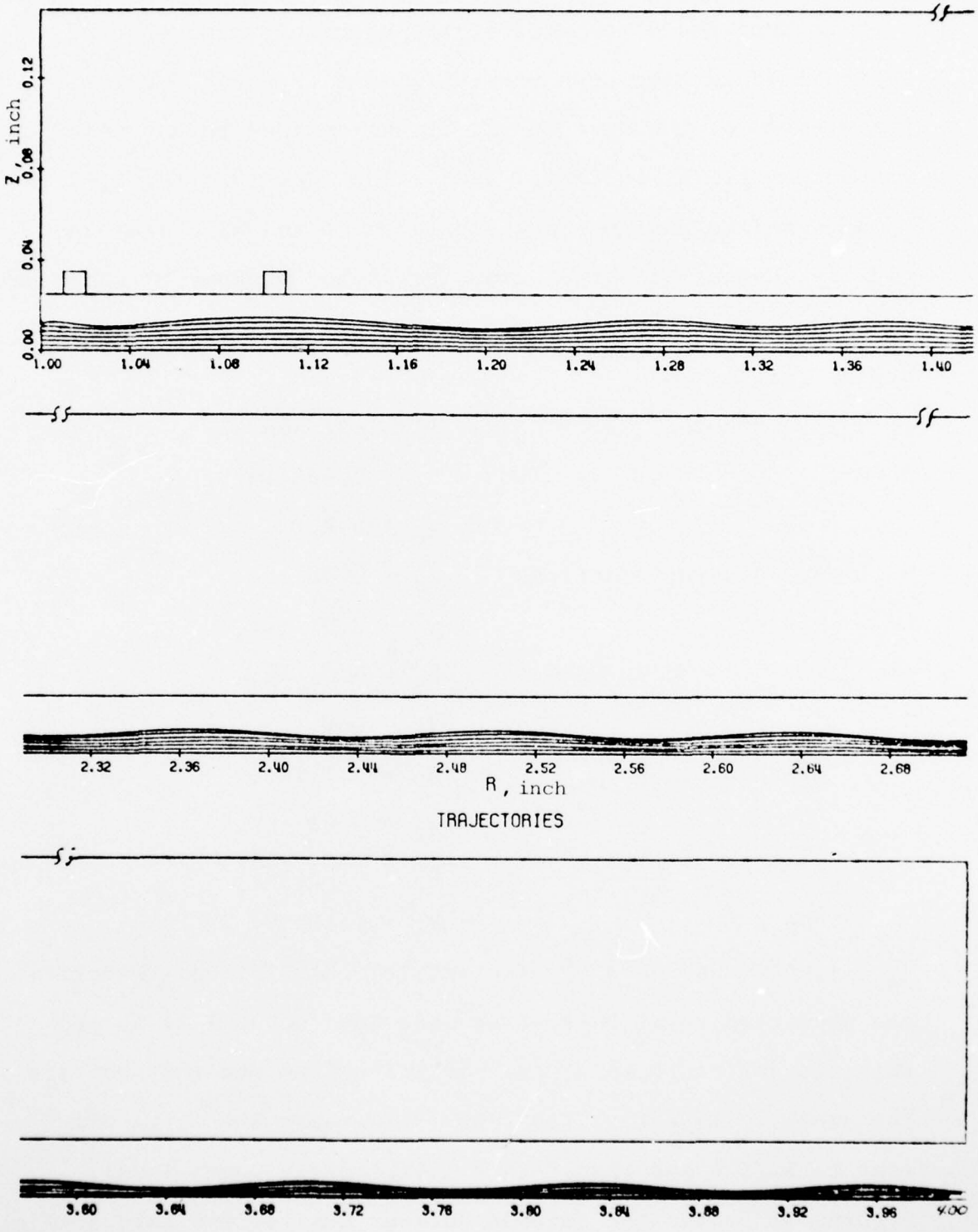

FIG. 45b BEAM TRAJECTORIES PLOT FOR A MAGNETIC FIELD WITH CURRENT LEVELS IN THREE SECTIONS OF COIL AS 3.4 A, 3.8 A, 2.7 A.

G. Gun Design II

Because the wires used in the electrode and anode of Design I would have been very difficult to embed firmly in the grooves of the dielectric, it was decided to use thin molybdenum strips in their place. The fact that the effects of such a late design change could be so readily determined clearly demonstrates the value, power and economy of computer-aided design techniques. The parameters for this new design are as follows:

for cathode	flat surface,
	h_c = 0.025 in.,
	V_c = 0 V,
for focusing electrode	d_1 = 0.01 in.,
	w_1 = 0.01 in.,
	h_1 = 0.04 in.,
	V_e = 0 V,
for anode	d_2 = 0.1 in.,
	w_2 = 0.01 in.,
	h_2 = 0.04 in.,
	V_a = 1,100 V.

V_a = 1,000 V was used for the initial calculation. However, the predicted total current was too low (about 1 A) to produce the desired beam power. It was determined that raising the anode voltage to 1,100 V would increase the total current to 1.15 A and result in a satisfactory power level. Figure 46 shows the cathode current density for this design.

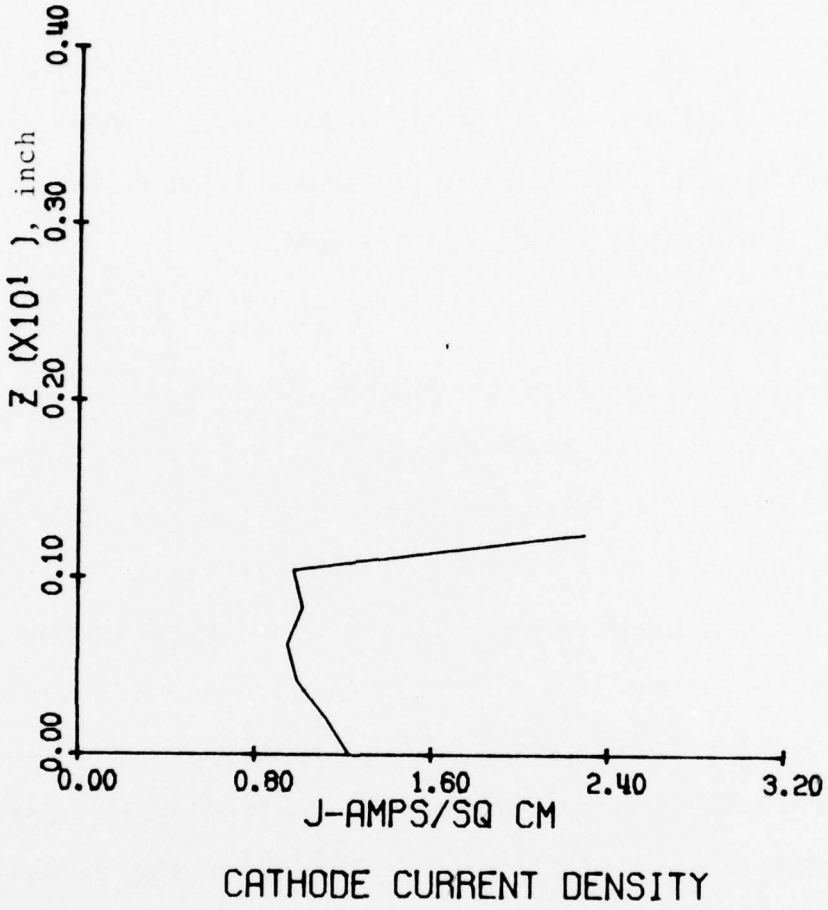

Total Current = 1.15 A
Perveance = 36 μpervs

FIG. 46 CATHODE CURRENT DENSITY AS A FUNCTION OF Z FOR A STRIP ELECTRODE AND ANODE.

The trajectories out to R = 1.25 in. using the magnetic field of Fig. 14 with current levels of 3.4 A, 3.8 A, 2.7 A are shown in Fig. 47. We would expect the trajectories beyond R = 1.25 in. to be similar to those of Fig. 45b because the same coil current levels were applied and the two beam currents are nearly the same.

H. Conclusions

A radial beam electron gun has been designed for operation at a power of approximately 1.2 kW. The effects upon the beam current of various geometries and voltages of cathode, anode and electrodes were investigated. It was found that the beam current is very sensitive to the position and voltage of the focusing electrode and is somewhat less sensitive to the position and voltage of the anode. Therefore, the beam current may be controlled by appropriate adjustments to the voltage and position of the focusing electrode and anode. The magnetic field has no effect on the beam current but, of course, is essential to the focusing of the beam.

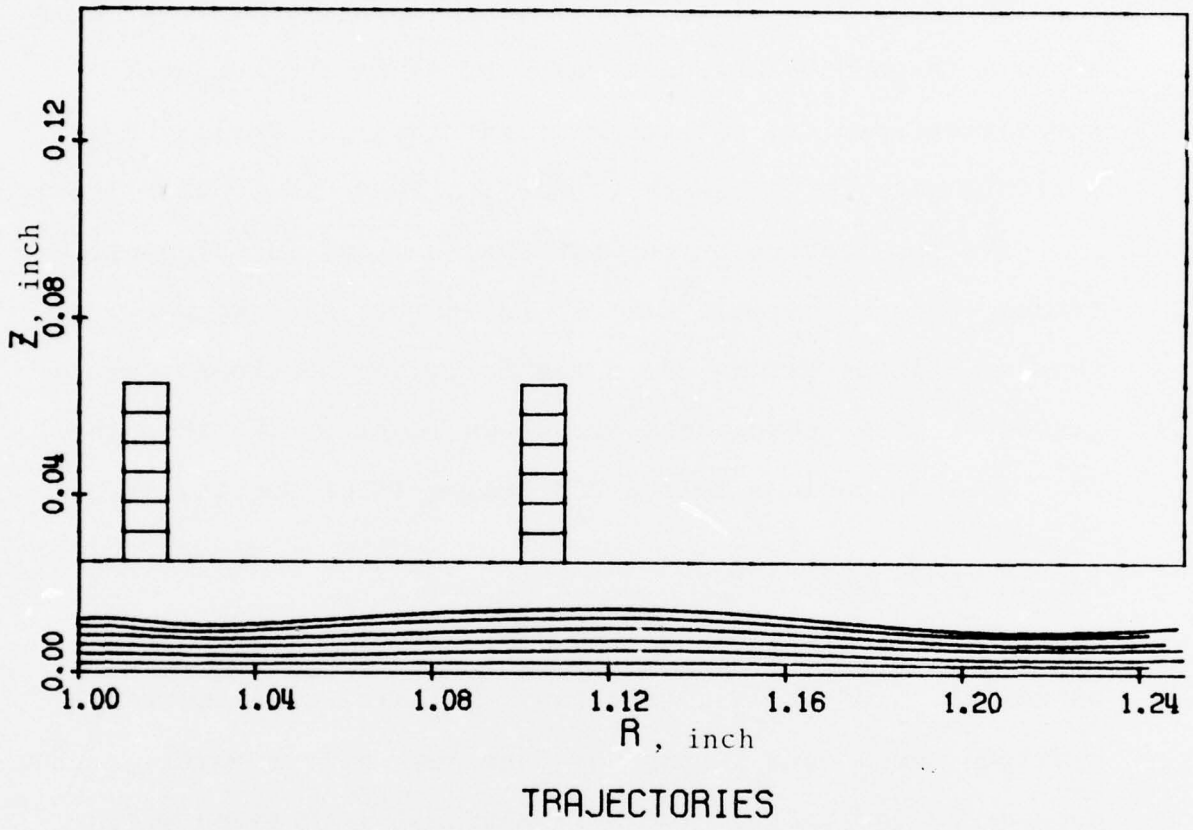

FIG. 47 TRAJECTORIES PLOT FOR A STRIP ELECTRODE AND ANODE.

SECTION V. FABRICATION OF RADIAL-BEAM ELECTRON GUN

A. Introduction

The objective of the experimental program is to produce a gun with good beam transmission based on the computer simulation results. It is important that the design be as flexible as possible so that modifications can be made easily.

The fabrication of the cathode, heater, focusing electrodes, anodes, ceramic plates, collectors and vacuum chamber will be discussed in the following sections. Photographs of these components are shown in Figs. 48 through 52. All dimensions follow Gun Design II of Section IV.

B. Cathode and Heater

The cathode was made from a nickel ring coated with an admixture of barium, strontium and calcium carbonates.[11,12] Hydrogen and vacuum firing was done just before coating. The cathode is indirectly heated by means of a tungsten wire coil and is capable of providing a current of up to 3 A/cm^2 with a two percent duty cycle at an operating temperature of 850°C to 900°C. However, during cathode activation, it is necessary to raise the temperature of the cathode to approximately 1,100°C for short periods (up to 30 seconds) at intervals of several minutes in order to assure complete

---

11. W. H. Kohl, Materials and Techniques for Electron Tubes, Reinhold Publishing Corp., NY; 1960.
12. F. Rosebury, Handbook of Electron Tube and Vacuum Techniques, Addison-Wesley Publishing Co., Reading, MA; 1965.

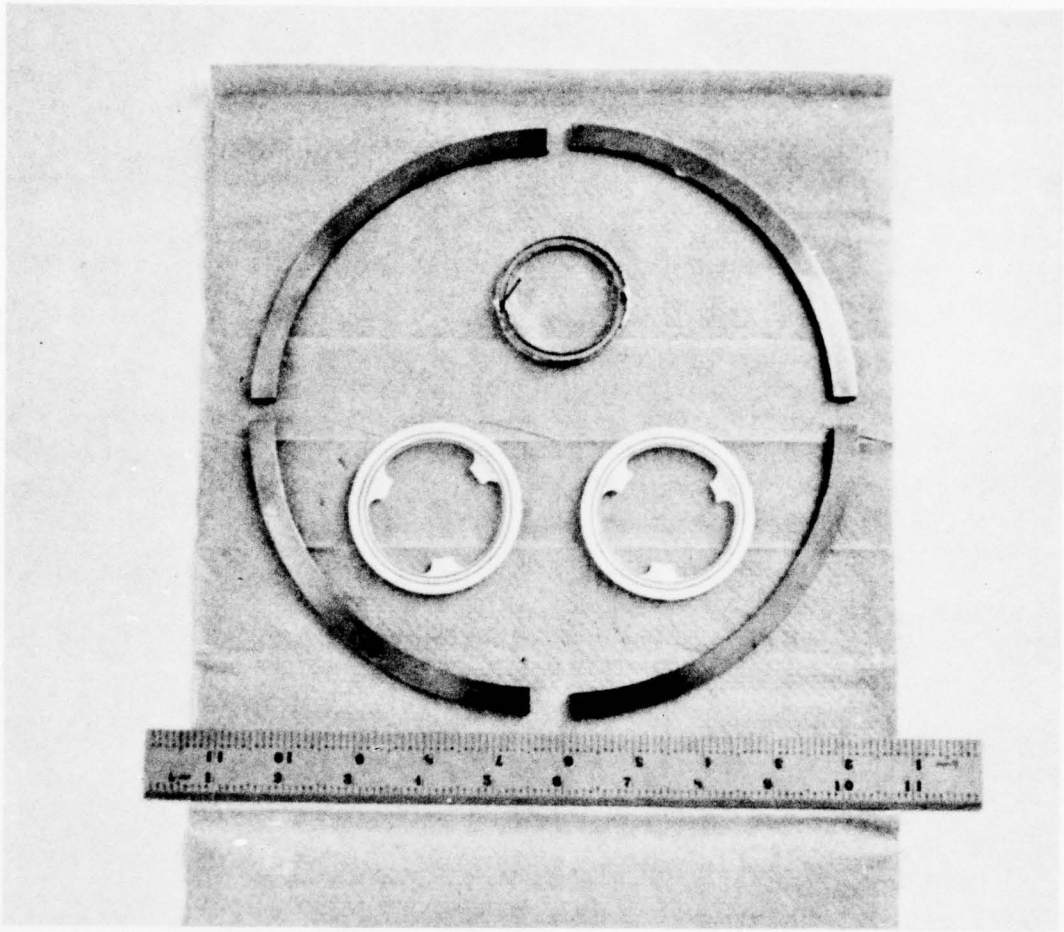

FIG. 48 PHOTOGRAPH OF A CATHODE WITH HEATER, TWO INNER CERAMIC RINGS AND A FOUR-SEGMENT COLLECTOR. EACH CERAMIC RING CONTAINS A FOCUSING ELECTRODE AND AN ANODE.

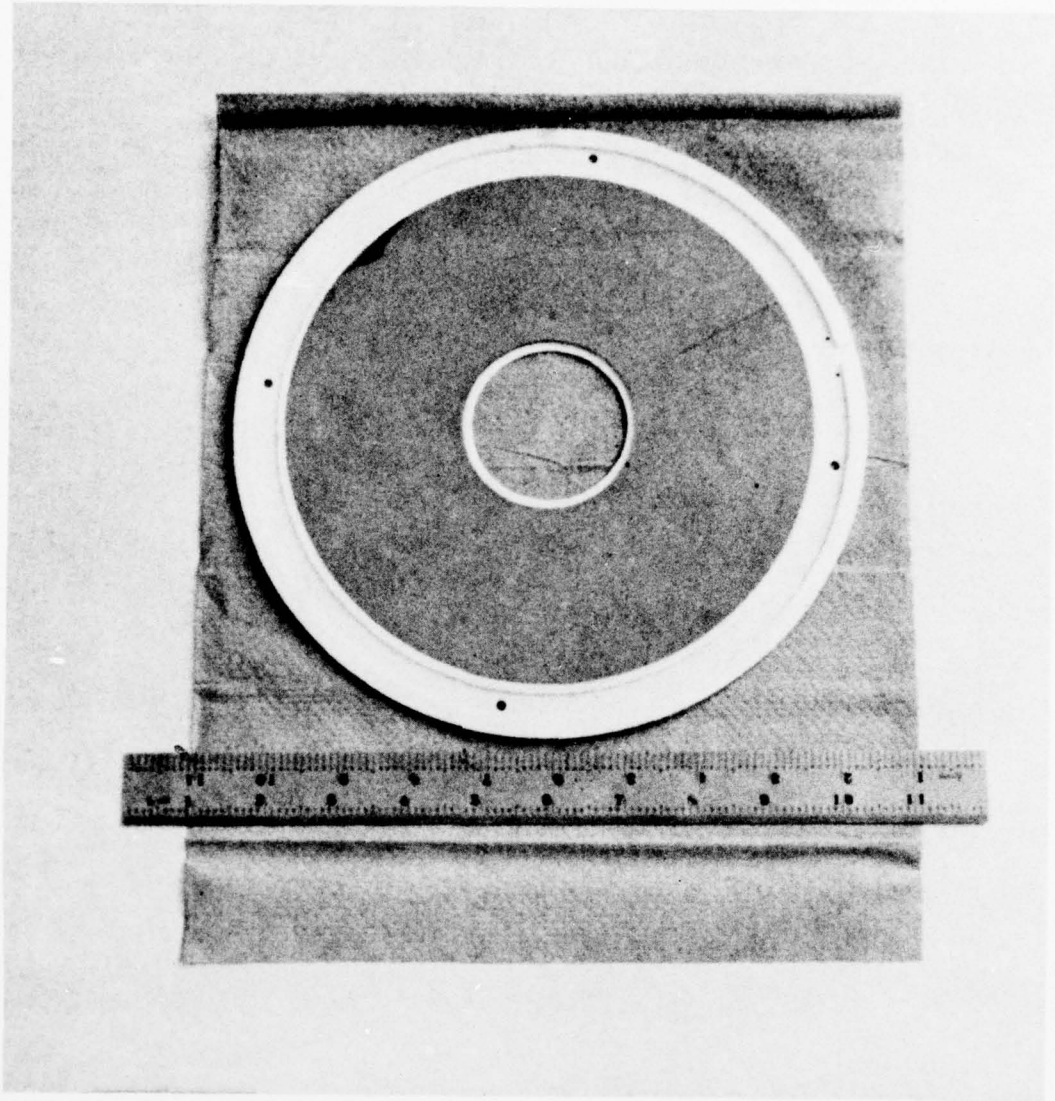

FIG. 49 CERAMIC PLATE WITH ONE SURFACE COATED WITH A CONDUCTING LAYER TO SIMULATE THE DC EFFECTS OF SPIRAL RF CIRCUIT.

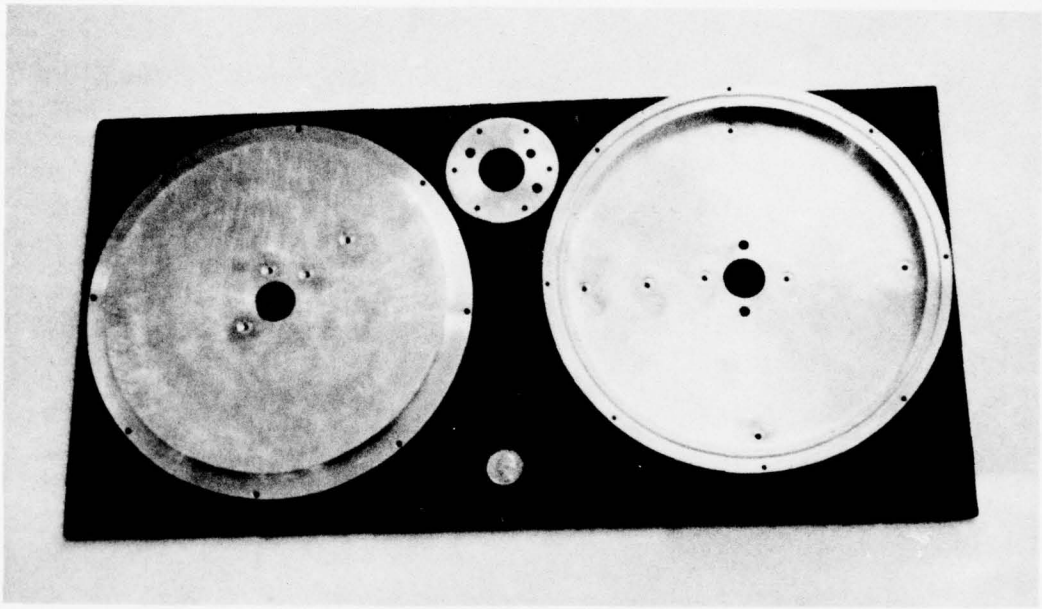

FIG. 50 TWO DISK-SHAPED ALUMINUM PIECES FOR VACUUM CHAMBER ASSEMBLY.

AD-A041 212 SHARED APPLICATIONS INC ANN ARBOR MICH F/G 9/1
RADIAL BEAM TWT ELECTRON BEAM ANALYSIS.(U)
MAY 77 K CHANG, J E ROWE
UNCLASSIFIED DAAB07-76-C-1360
ECOM-76-1360-F NL

2 OF 2
AD
A041212

END

DATE
FILMED
7-77

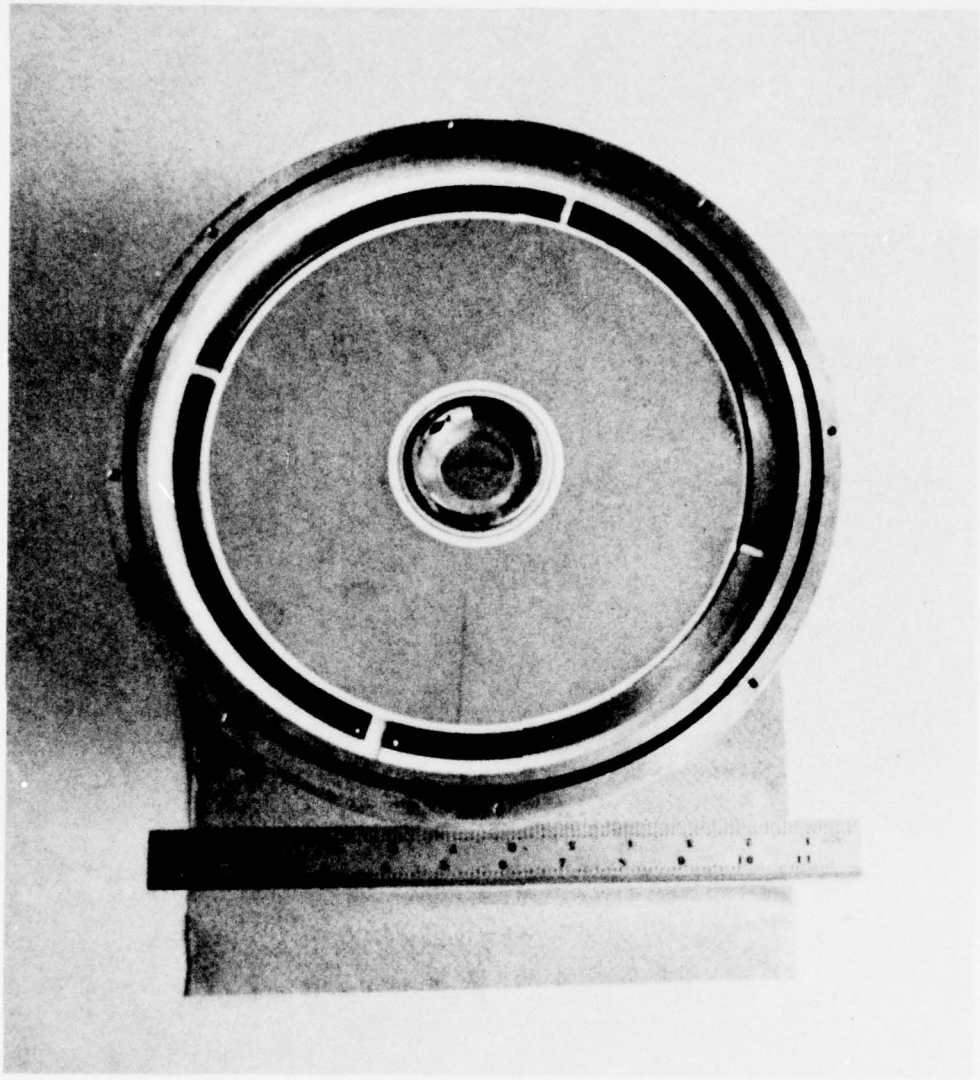

FIG. 51 VIEW OF ELECTRON GUN WITH ALL ITS COMPONENTS IN ALIGNMENT. A SYMMETRICAL CERAMIC PLATE WILL REST ON TOP THE COLLECTOR AND CATHODE.

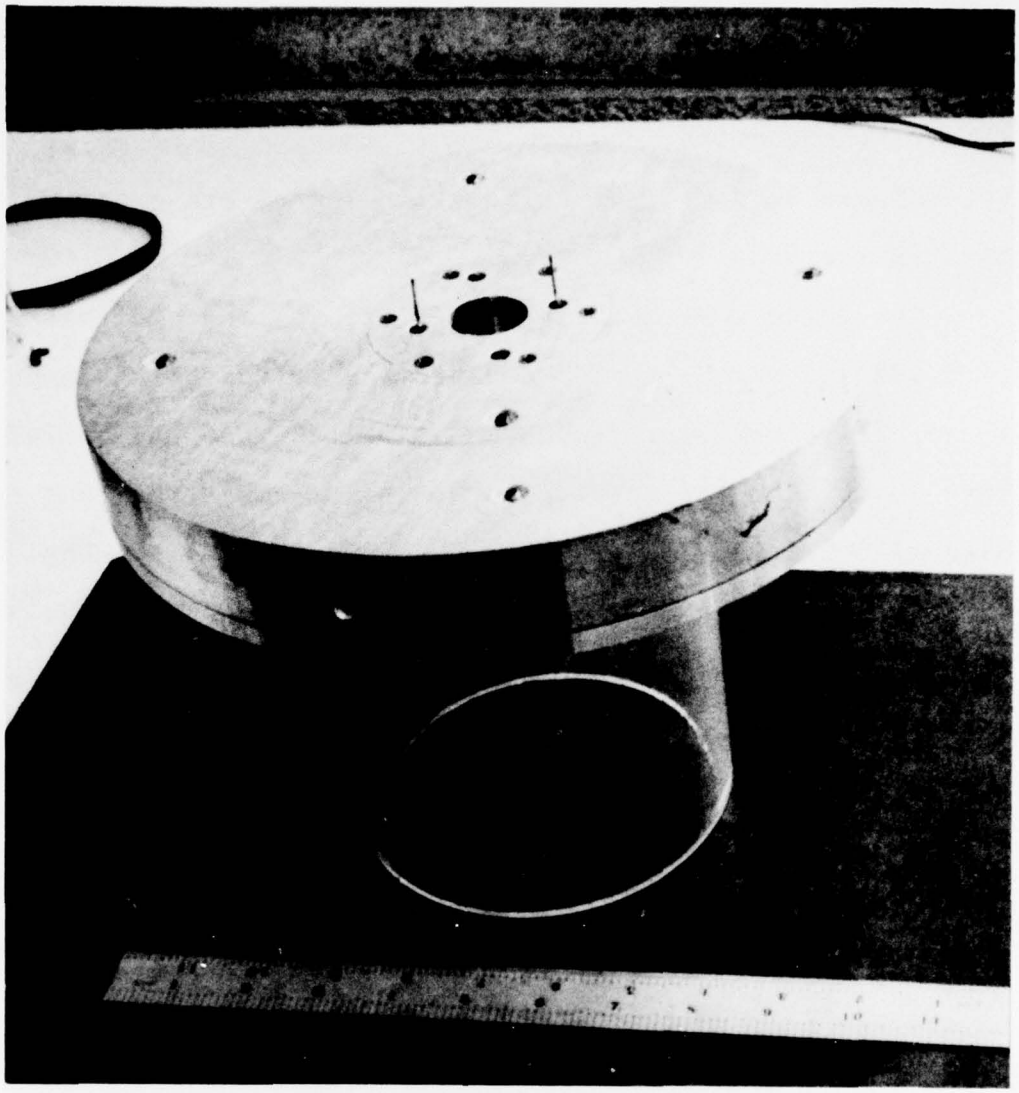

FIG. 52 ASSEMBLED VACUUM CHAMBER CONTAINING ELECTRON GUN. ALSO SHOWN ARE THE FEEDTHROUGHS AND THE HEATER LEAD POSTS.

conversion.[12] The maximum chemical change from carbonate to oxide occurs in the neighborhood of 900°C; the 1,100°C temperature is applied in order to assure complete conversion of the coating, especially at the ends or edges of the cathode surface, where radiation losses are greater than in the middle.

The cathode has a height of 0.025 in. and a diameter of 1.972 in. which expands to 2.00 in. at operating temperature. A rectangular trough was machined into the nickel ring supporting the cathode (see Fig. 53) and the tungsten wire of 0.011 in. diameter was embedded inside it. The cathode-heater assembly was sandwiched between two annular pieces of ceramic (see photograph of ceramic rings in Fig. 48) as shown in Fig. 53. Since the nickel base might expand by 0.014 in. in radius at operating temperature, space was left to accommodate expansion without cracking the ceramic. A tantalum foil was placed over the heater trough of the nickel ring to minimize radiation heat loss to the ceramic. Some tantalum strips were wedged between the nickel ring and the ceramic supports to hold the ring in its concentric position prior to cathode activation and testing. As the cathode expands, the tantalum foil compresses together leaving room for expansion.

In order to confine heat to the cathode and minimize leakage to the ceramic plates, only a small part of the ceramic ring was allowed to contact the cathode-heater assembly. This was accomplished by machining three legs in each of the ceramic support rings.

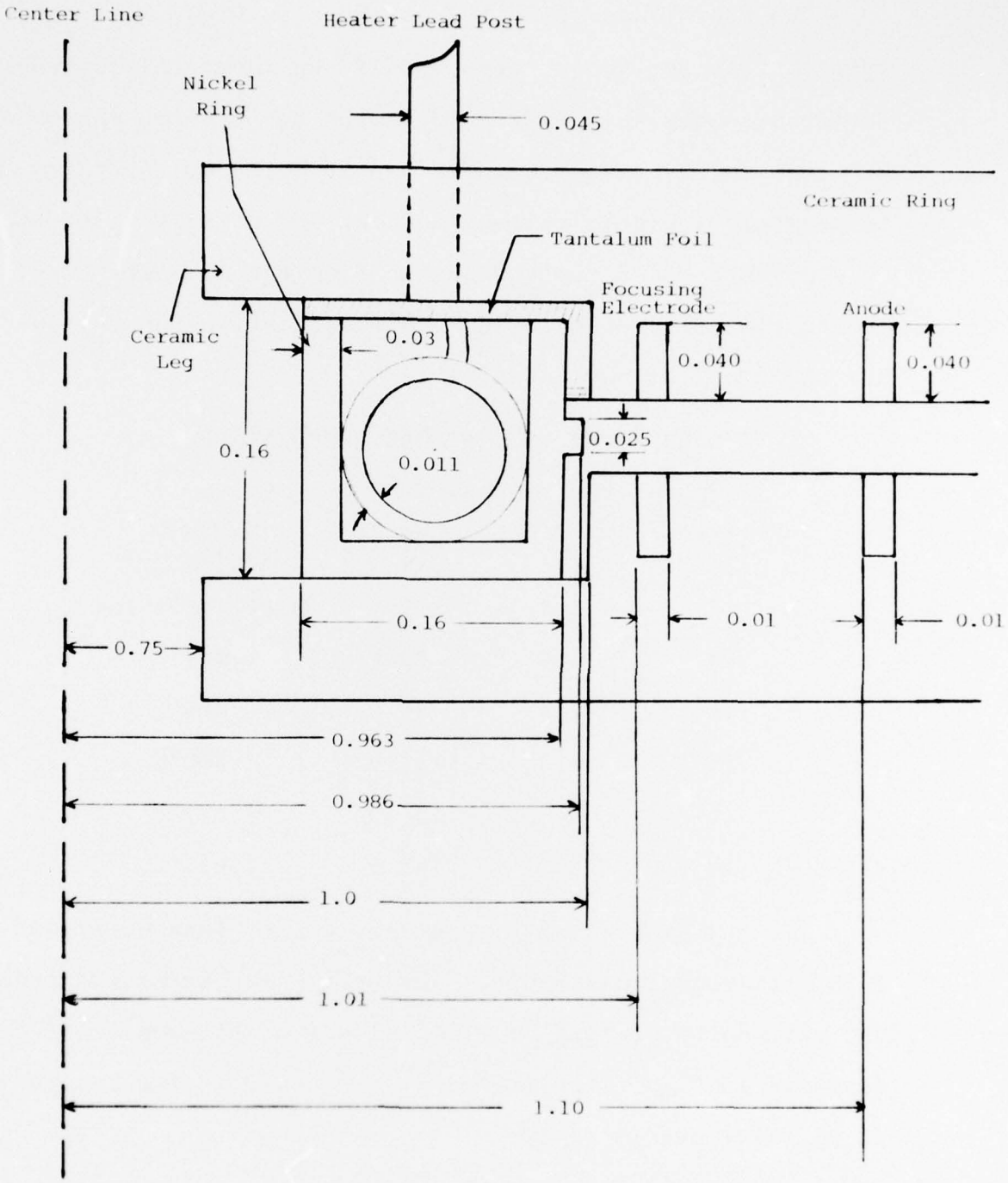

FIG. 53 CATHODE, HEATER AND CERAMIC RINGS. (NOT TO SCALE, ALL DIMENSIONS IN INCHES)

The heater was connected as shown in Fig. 54. Before installation in the prototype RBTWT, an identical cathode-heater assembly was tested and proven to have the capability of producing a cathode temperature of 1,115°C. At this temperature a heater voltage and current of 17 V and 8.8 A (i.e., about 150 W) were required from the ac power supply. The test results of cathode temperature versus heater power are shown as follows:

HEATER POWER VS. CATHODE TEMPERATURE

Heater Power Supply			
Voltage (V)	Current (A)	Power (W)	Cathode Temperature
5	3.8	19.0	Dull Radiation
10	7.0	70.0	805°C
12	7.4	88.8	915°C
15	8.2	123.0	1,000°C
16	8.5	136.0	1,075°C
17	8.8	149.6	1,115°C

The resistance measured at the heater lead posts was 0.25 Ω at room temperature. The heater was insulated from the cathode by coating it with a layer of Alundum. As depicted in Fig. 54, the heater was wound in two sections in parallel electrically.

C. Focusing Electrode and Anode

As mentioned earlier in Section IV, the round wire type electrodes would have been difficult to hold in position inside the ceramic ring. Therefore a ribbon-type wire was

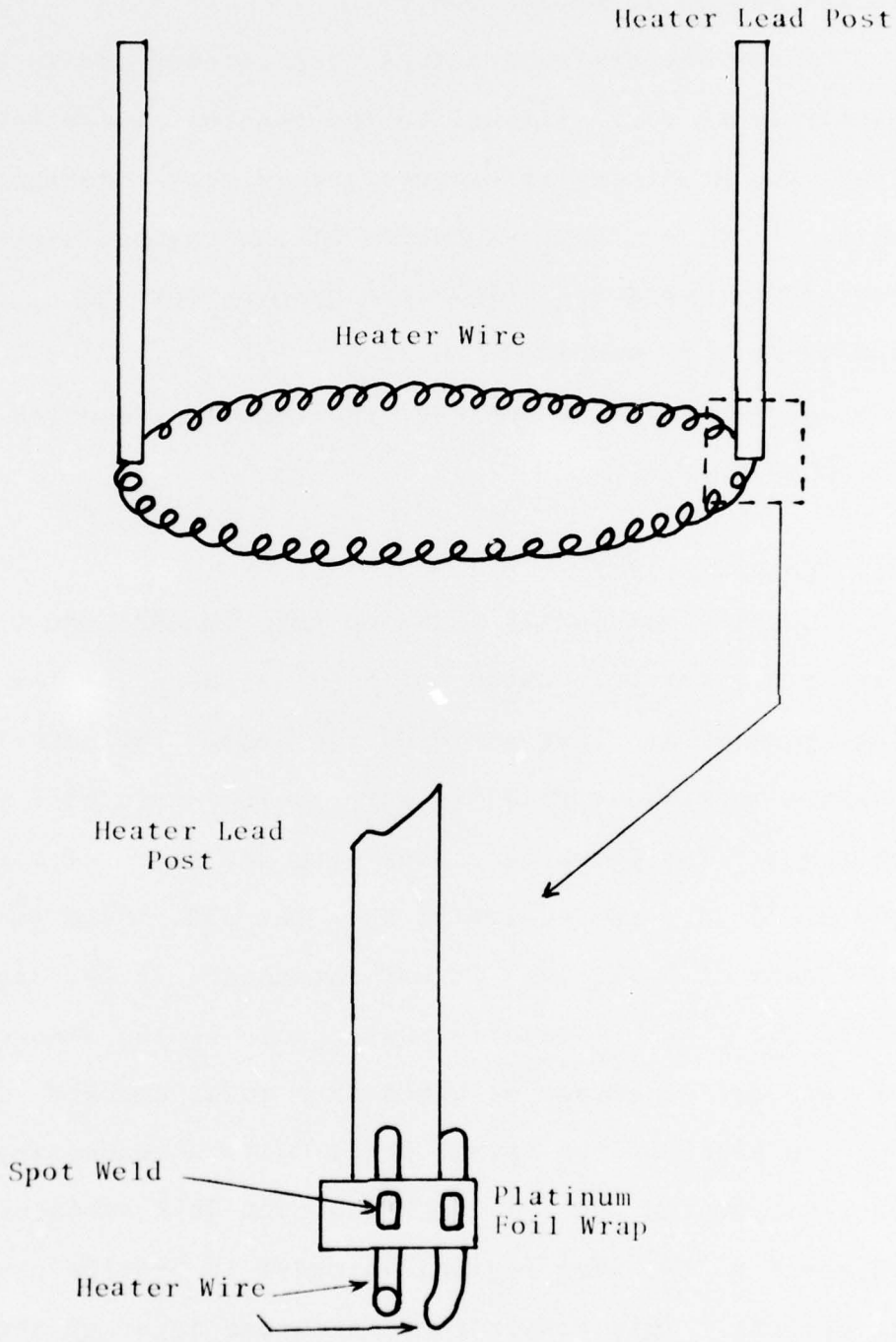

FIG. 54 SKETCH OF HEATER SHOWING TWO TUNGSTEN WIRES CONNECTED IN PARALLEL.

used as shown in Fig. 53. The computer results are shown in Gun Design II of Section IV.

Since the distance between the cathode and focusing electrode is very critical to the control of the beam current, the machining tolerance plays a very important role here. Also, the heat expansion of the cathode nickel base had to be considered before the grooves for the electrode and anode were machined.

A photograph of the electrode-anode assemblies is shown in Fig. 48.

D. Ceramic Plates

Corning machinable glass-ceramic (MACOR Code 9658) with a dielectric constant of 5.92 was used for the insulating substrate that enclosed the beam. The material is readily machinable with ordinary tools and is easily polished. Two pairs of plates with diameters of 9.1 in. and 2.924 in., respectively, were cut and ground to a thickness of 0.125 in. It was intended that the small plate (or ring) be readily replaceable if the dimensions of cathode, electrode or anode have to be changed.

In place of the spiral RF circuit, a conducting surface was coated on the large-diameter disk surfaces, adjacent to the beam region, in order to provide proper dc effects. This consisted of a chrome layer of about 1,000 Å, deposited by evaporation techniques, followed by a 70,000 Å gold layer deposited by electroplating.

Figure 49 shows the large-diameter ceramic plate and its conducting surface.

E. Collector

The collector consists of four machined copper ring segments extending around the circumference of the drift region. As shown in Fig. 55, the collector has a groove of width 0.050 in. (the spacing between the ceramic layers) and a depth of 0.275 in. A gap separated the collector from the enclosing chamber, providing electrical isolation from all other tube components so that (1) the collector potential could be depressed and (2) the collector current could be measured separately from the currents due to previous beam interception. Each of the four angular segments was electrically isolated. This was to enable a straightforward measurement of the angular symmetry of the radial beam by comparison of the currents collected in the segments. One slot between two of the segments was enlarged slightly to allow connection to the vacuum pump and probe access for possible future measurements. The collector and cathode rings maintain the 0.050 in. spacing between the two ceramic plates.

Three precautions were taken to minimize secondary emission at the collector due to beam bombardment:

1. The inside of the collector groove was coated with a colloidal suspension of graphite in water (Aquadag). The resulting carbon layer would reduce the secondary-emission coefficient from 1.3 to about 0.5.

2. The end of the groove was machined and angled to deflect secondaries.

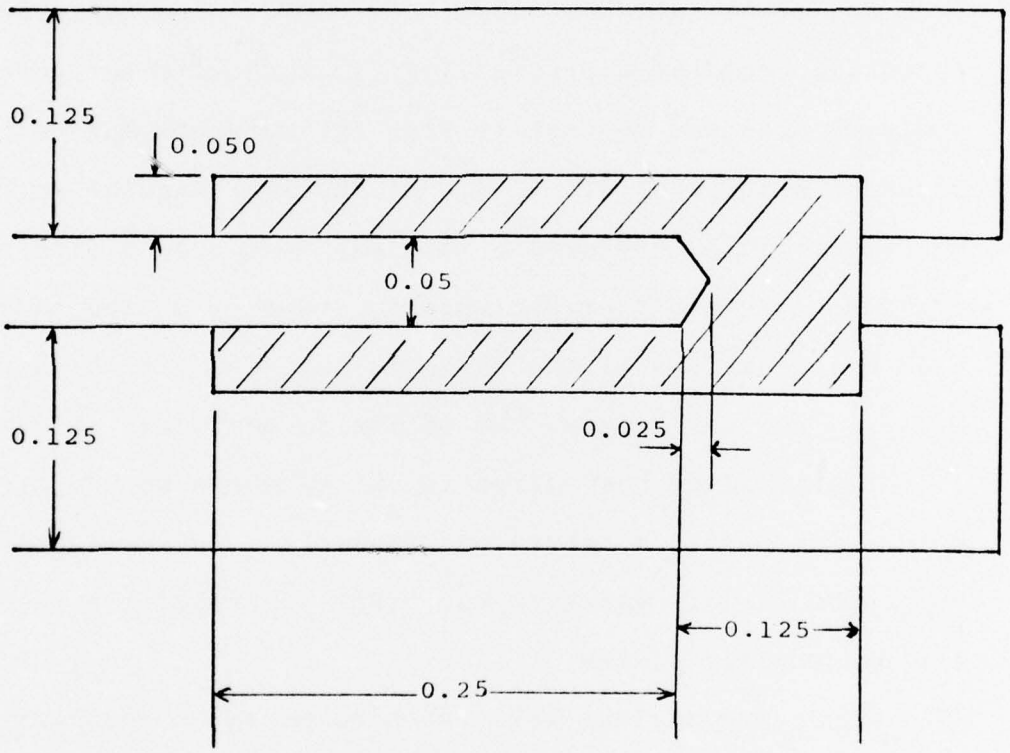

FIG. 55 CROSS SECTION OF A COLLECTOR RING INSIDE THE CERAMIC PLATES. (NOT TO SCALE, ALL DIMENSIONS IN INCHES)

3. The collector groove was made five times deeper than its width in order to trap most secondary electrons.

The collector is shown in Figs. 48 and 51.

F. Vacuum Chamber

The vacuum chamber contains the electron gun assembly and was fabricated from two 10.35 in. diameter aluminum disks, one 1.25 in. thick and the other 0.625 in. thick. As in Fig. 56, a 9.1 in. diameter, 0.625 in. hollow was machined in the thicker of the pieces, thus producing a trough to contain the electron gun.

A rectangular groove was machined around the edge of one piece to hold the Viton O-ring which provided the vacuum seal. This type of seal was selected for this prototype RBTWT to permit rapid access to the electron gun for modification purposes.

The center pole piece was inserted through one-inch diameter holes in the center of each half of the vacuum chamber. Again, the vacuum seal was accomplished with Viton O-rings installed around the center pole piece.

A small hole was machined at one end of the vacuum chamber precisely at the collector ring level to accept the flanged connection to a conventional vacuum pump. The same aperture would allow the device to be connected to a beam analyzer.

Sealed feedthroughs were installed on the wall of the vacuum chamber for the connections to the various electrodes and heater.

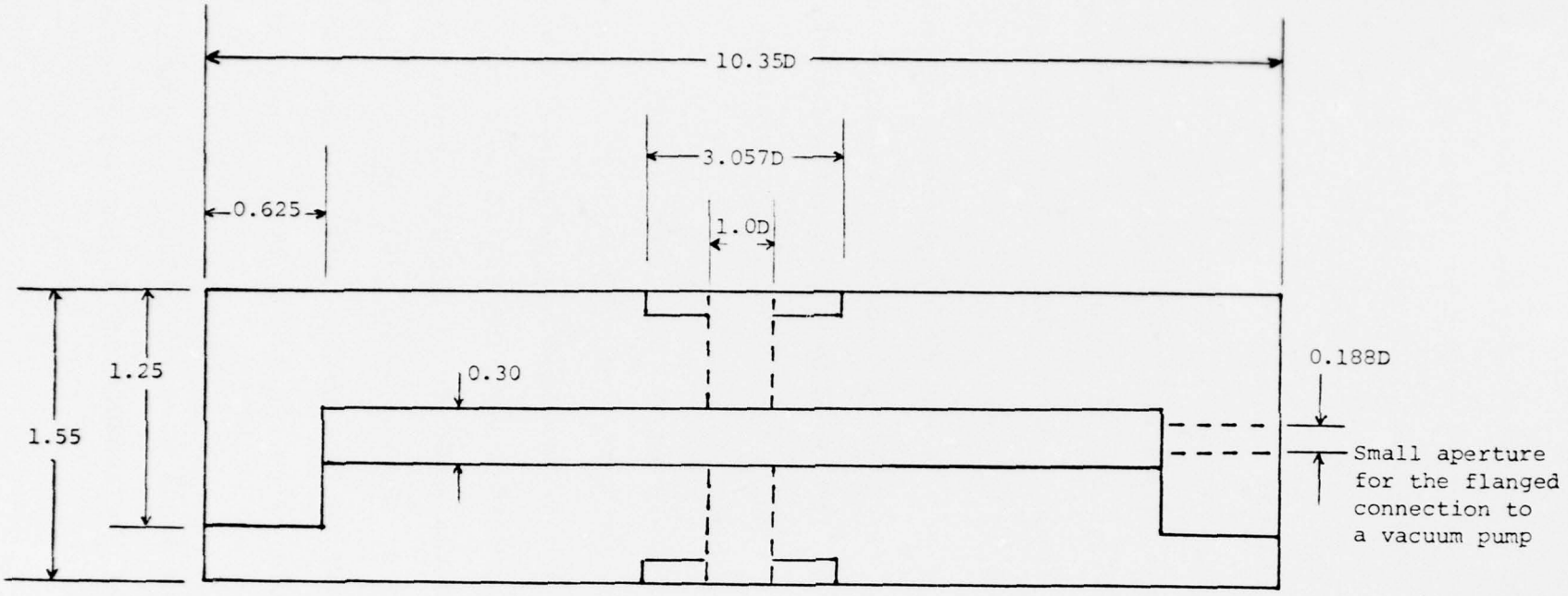

FIG. 56 VACUUM CHAMBER. (NOT TO SCALE, ALL DIMENSIONS IN INCHES)

A photograph of the vacuum chamber can be found in Figs. 50 or 52.

SECTION VI. TEST OF EXPERIMENTAL TUBE

A. Experimental Setup

The vacuum chamber containing the electron gun was first tested to determine vacuum tightness before it was mounted inside the magnetic focusing structure. For the series of static tests, the experimental tube was mounted on a vacuum pumping system. When the proper vacuum had been achieved (less than 10^{-8} Torr), the cathode was activated (as indicated by a sudden pressure increase at a cathode temperature of approximately 900°C). The various electrodes were connected to their respective power supplies after the activation process had been completed.

All measurements were to be taken with the tube operating in a pulsed mode to minimize the heat-dissipation requirements. The currents in the anode, the simulated RF circuit planes and each of the four collector segments were closely monitored by measuring the voltage across low-value resistors placed between each electrode and ground. Oscilloscopes were used to measure the currents for pulsed-mode operation. Since it would have been difficult to ensure electrical isolation between the heater and cathode at high voltage levels, one of the heater leads was connected to the cathode. An isolated ac power supply was used to energize the heater and a high-voltage pulse generator was used to apply the voltage pulses between the grounded electrodes and the isolated cathode-heater assembly.

The pulse generator has the capability of providing 0.1 percent to 2 percent duty cycle pulses over a range of 0 V to 2 KV.

The test setup is shown in Fig. 57 and a photograph is given in Fig. 58.

B. Discussion of the Problems

The experiment failed to provide significant results due to the following problems:

1. One of the heater wires was broken; thus, only half of the cathode was activated and operated.

2. Nickel particles evaporated from the cathode and deposited on the ceramic surface between the cathode and anode. This thin film of nickel constituted a current path between the cathode and anode when a negative high voltage was applied to the cathode.

3. Leaks developed in the vacuum equipment after the cathode had been activated.

The first problem occurred shortly after the heater had been energized. The other problems occurred several hours later during an extended pump-down for the purpose of degassing the tube. Unfortunately, corrective action and testing was not possible within the scope of the contract.

C. Recommended Solutions to the Problems

Although time and budget did not allow continuation of the experimental measurements, some modifications have been devised to eliminate the problems encountered.

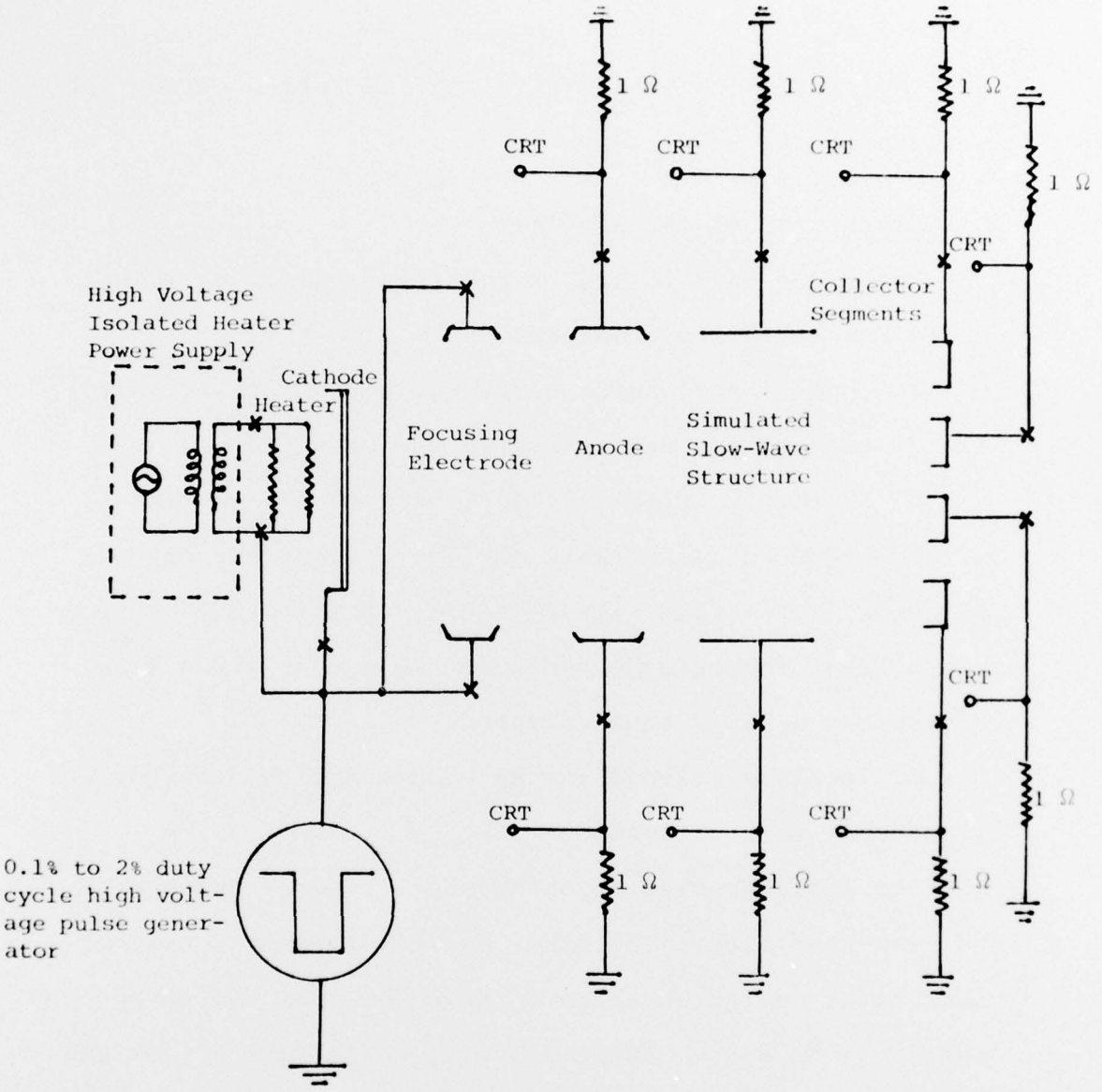

X - indicates feedthrough

FIG. 57 ELECTRICAL CONFIGURATION FOR EXPERIMENTAL MEASUREMENTS.

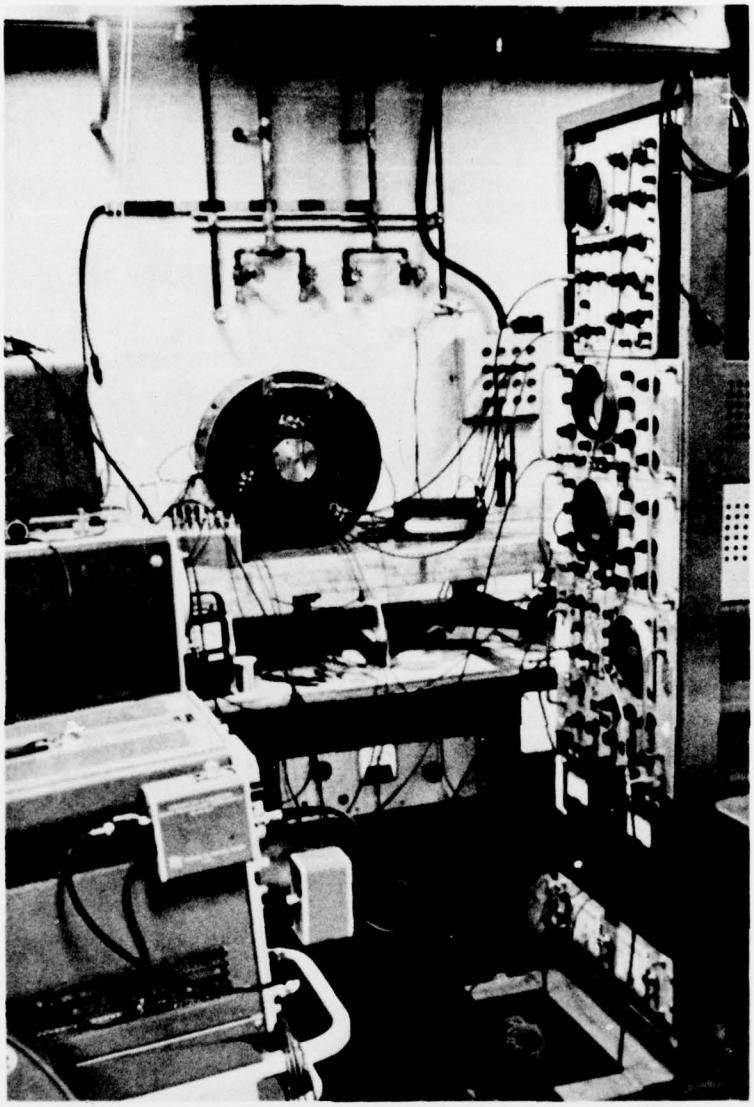

FIG. 58 PHOTOGRAPH OF EXPERIMENTAL SETUP.

A larger diameter heater wire should be used. Examination of the failed heater showed some necking-down had occurred at the point of connection to the heater lead. It is believed this led to the subsequent failure. Most of the leakage appeared to be in the vacuum connections external to the tube and are easily eliminated. However, all feedthroughs, connections and joints should receive a coating of sealant as added protection against leakage at high operating temperatures.

It is difficult to prevent the deposit of nickel particles on the ceramic surface around the cathode area. However, machining several grooves in the ceramic ring around the cathode would insert discontinuities in the thin film connection between the cathode and anode. Figure 59 shows this technique with two grooves.

D. Conclusions

Although the initial test did not provide useful experimental results, a great deal of valuable experience was gained during the fabrication and measurement procedures. It is believed that the modifications described above would allow successful completion of the test. This, in turn, would provide verification of the computer predictions.

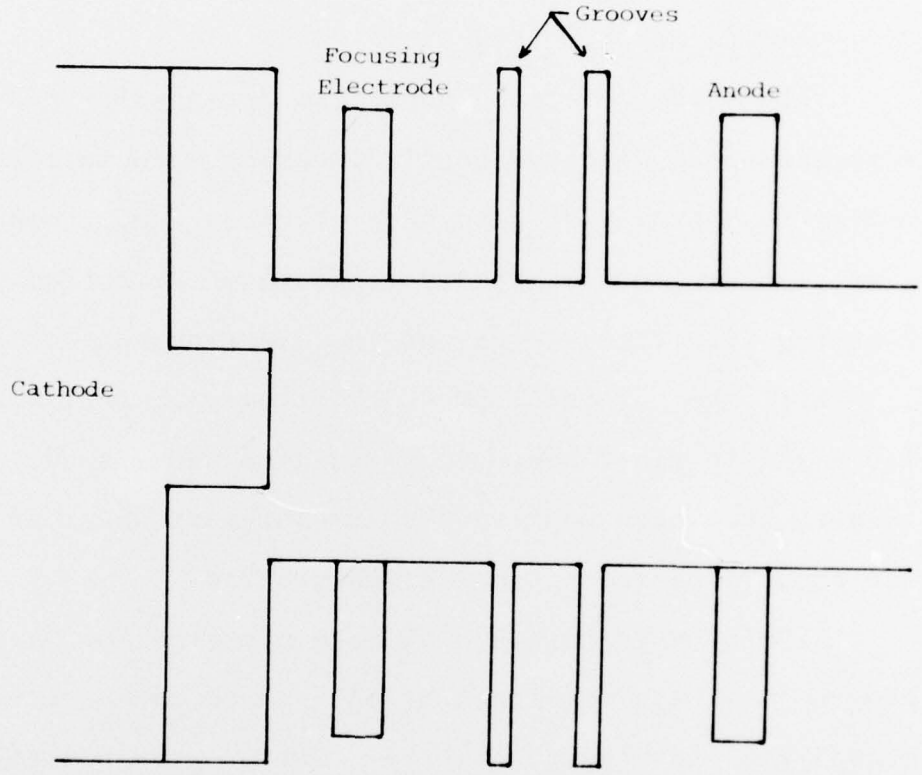

FIG. 59 GROOVES IN THE CERAMIC DISKS BETWEEN ANODE AND CATHODE TO MASK NICKEL DEPOSITION.

SECTION VII. CONCLUSIONS AND RECOMMENDATIONS FOR FUTURE STUDY

A. Introduction

The work reported in the preceding sections is reviewed briefly here and the results are summarized. Some recommendations for future study are outlined.

B. Summary of this Study

This study developed practical designs for prototype versions of an electromagnetic focusing structure and a radial beam traveling-wave tube electron gun. Computer simulations were used to develop both the electromagnetic focusing structure design and the electron gun design.

With the Deformable Mesh Electromagnet Design Program, the magnetic field has been calculated and shaped. The results have been confirmed by measurement and supplied as the input data to the gun design program.

A Deformable Mesh Radial Beam Electron Gun Design Program has been developed by SAI and served as a fundamental tool for the gun design. The program was utilized to analyze practical electrode shapes and determine optimum positions. The effects of cathode geometries and various electrode voltages on the beam current have also been investigated. It was found that the beam current is very sensitive to the position and voltage of the focusing electrode.

A final design with a well focused beam has been recommended and an experimental tube built. The limited contract

period did not allow sufficient time to carry out a successful experiment.

C. Recommendations for Future Study

There are several interesting areas where it is felt that further theoretical and experimental study would be beneficial in the development of the RBTWT.

The most important of these is the development of a large-signal analysis program which treats both uniform and nonuniform magnetic field distributions. The analysis developed by Kooyers and Shaw[4] has limited application since it treats only one particular type of beam flow which is in a uniform magnetic field.

Another area of interest is a study of the feasibility of using permanent magnets for the RBTWT focusing structure in order to reduce weight. A Deformable Mesh Permanent Magnet Design Program similar to that described in Section III should be developed for this purpose.

Finally, an electrostatically focused beam may be worthy of investigation, especially for higher operating frequencies. At higher frequencies, the physical length of the drift region can be reduced drastically. Therefore, even without the magnetic field, the electron beam may be able to reach the collector before being intercepted. This is further evident from Fig. 41 which shows that the electron beam is not intercepted in a short distance even without the focusing magnetic field. Computer analyses should be conducted to determine the feasibility of electrostatic electron gun development for high frequency tubes.

REFERENCES

1. V. S. Savel'yev and G. I. Kushenko, "Experimental Investigation of a TWT with a Radial Electron Stream," Radio Eng. and Electronic Phys., vol. 15, No. 12, pp. 2267-2272; 1970.

2. V. I. Molyavko, et al., "Interaction Between a Radially Divergent Electron Beam and a Slow Electromagnetic Wave," Radio Eng. and Electronic Phys., vol. 16, No. 8, pp. 1330-1335; 1971.

3. J. L. Putz and A. W. Scott, "Development of a Planar Equiangular Spiral Amplifier," Report ECOM 73-0148-F, U. S. Army Electronics Command, Fort Monmouth, NJ; September 1974.

4. G. P. Kooyers and E. K. Shaw, "Radial Beam TWT Large Signal Analysis," Final Report ECOM 74-0377-F, U. S. Army Electronics Command, Fort Monmouth, NJ; November 1975.

5. P. T. Kirstein and J. S. Hornsby, "An Investigation Into the Use of Iterative Methods for the Analysis of Axially Symmetric and Sheet Beam Electrode Shapes with an Emitting Surface," IEEE Trans. on Electron Devices, vol. ED-11, No. 5, pp. 196-204; May 1964.

6. V. Hamza and G. S. Kino, "The Accuracy of Numerical Solutions for Electron Gun Design," IEEE Trans. on Electron Devices, vol. ED-14, No. 4, pp. 195-201; April 1967.

7. V. Hamza, "Convergence and Accuracy Criteria of Iteration Methods for the Analysis of Axially Symmetric and Sheet Beam Electrode Shapes with an Emitting Surface," IEEE Trans. on Electron Devices, vol. ED-13, No. 5, pp. 485-493; May 1966.

8. J. E. Boers, "Computer Simulation of Space-Charge Flows," Tech. Report No. RADC-TR-68-175, Rome Air Development Center, Air Force Systems Command, Griffiss Air Force Base, NY; April 1968.

9. R. B. True, "Space-Charge-Limited Beam Forming Systems Analyzed by the Method of Self-Consistent Fields with a Solution of Poisson's Equation on a Deformable Relaxation Mesh," Ph.D. Thesis, University of Connecticut; 1972.

10. A. M. Winslow, "Numerical Solution of the Quasilinear Poisson Equation in a Nonuniform Triangle Mesh," J. Computational Phys., vol. 2, pp. 149-172; 1967.

11. W. H. Kohl, Materials and Techniques for Electron Tubes, Reinhold Publishing Corp., New York; 1960.

12. F. Rosebury, Handbook of Electron Tube and Vacuum Techniques, Addison-Wesley Publishing Co., Reading, MA; 1965.

LIST OF SYMBOLS

Symbol	
$\bar{A}$	Vector potential of magnetic field
A_θ	θ-component of vector potential $\bar{A}$
$a_{i+(1/2)}$	Quadrilateral area for triangle i+(1/2)
$\bar{B}$	Magnetic induction
B_r	r-component of vector $\bar{B}$
B_z	z-component of vector $\bar{B}$
d_1	Distance between cathode surface and focusing electrode
d_2	Distance between cathode surface and anode
$\bar{E}$	Electric field
E_r	r-component of vector $\bar{E}$
E_z	z-component of vector $\bar{E}$
G_o	Residual in solving the Poisson's equation
h_1	Height of the focusing electrode
h_2	Height of the anode
h_c	Height of the cathode
i	Index of node in coordinate map
J	Cathode current density
j	Index of node in coordinate map
k	Defined as $4/9\ \varepsilon_o\sqrt{2\eta}$
n	Number of relaxation steps
P	Location of an electron
P_i	Mesh node neighboring P_o
P_{i+1}	Mesh node neighboring P_o
P_{i-1}	Mesh node neighboring P_o
P_o	Mesh node being relaxed

$\|\|R\|\|$	Euclidean norm
R_{cath}	Radius of cathode ring
$\dot{r}$	First derivative of r with respect to time
$\ddot{r}$	Second derivative of r with respect to time
$r(R)$	Coordinate in cylindrical system
r_i	r-coordinates of six surrounding nodes around node o
r_{i+1}	r-coordinate of point P_{i+1}
r_{i-1}	r-coordinate of point P_{i-1}
r_o	r-coordinate of the node o being relaxed
r_p	r-coordinate of point P
r_o^n	r-coordinate of the node being relaxed after nth relaxation
S	Source term in Poisson's equation
V	Potential
V_a	Voltage at anode
V_b	Voltage of electron beam
V_c	Voltage at cathode
V_e	Voltage at focusing electrode
V_i	Potential at node i
V_p	Potential at point p
V_o^n	Potential at node o after nth relaxation
W_i	Weighting factor between neighboring points P_o and P_i in solving the Poisson's equation
w_1	Width of the focusing electrode
w_2	Width of the anode

$\dot{z}$	First derivative of z with respect to time
$\ddot{z}$	Second derivative of z with respect to time
$z(Z)$	Coordinate in cylindrical system
z_i	z-coordinate of six surrounding nodes around node 0
z_o	z-coordinate of node o being relaxed
z_o^n	z-coordinate of the node being relaxed after nth relaxation
z_p	z-coordinate of point P
α	Overrelaxation parameter for mesh generation
α_o	Overrelaxation parameter in solving the Poisson's equation
ε_o	Permittivity of free space
ε_r	Relative dielectric constant
η	Electron charge-to-mass ratio
θ	Coordinate in cylindrical system
$\dot{\theta}$	First derivative of θ with respect to time
θ^+	Angle between P_oP_{i+1} and P_iP_{i+1}
θ^-	Angle between P_oP_{i-1} and P_iP_{i-1}
μ	Permeability in magnetic material
ξ_i	Residual vector
ρ	Radius of curvature of cathode
$\rho_{i+(1/2)}$	Space-charge density over triangle i+(1/2)
ω_c	Magnetic cyclotron frequency
ω_p	Beam plasma frequency

DISTRIBUTION LIST

12 Defense Documentation Center
Attn: DDC-TCA
Cameron Station (Bldg 5)
Alexandria, VA 22314

1 Code R123, Tech Library
DCA Defense Comm Engrg Ctr
1860 Wiehle Ave
Reston, VA 22090

1 Defense Communications Agency
Technical Library Center
Code 205 (P. A. Tolovi)
Washington, DC 20305

1 Office of Naval Research
Code 427
Arlington, VA 22217

1 Director
Naval Research Laboratory
Attn: Code 2627
Washington, DC 20375

1 Commander
Naval Electronics Laboratory Center
Attn: Library
San Diego, CA 92152

1 Rome Air Development Center
Attn: Documents Library (TILD)
Griffiss AFB, NY 13441

2 Cdr, US Army Missile Command
Redstone Scientific Info Center
Attn: Chief, Document Section
Redstone Arsenal, AL 35809

1 Commander
US Army Missile Command
Attn: DRSMI-RE (Mr. Pittman)
Redstone Arsenal, AL 35809

1 Director, Ballistic Missile Defense
Advanced Technology Center
Attn: ATC-R, PO Box 1500
Huntsville, AL 35807

1 Commander
HQ Fort Huachuca
Attn: Technical Reference Div
Fort Huachuca, AZ 85613

1 Deputy for Science and Technology
Office, Asst Sec Army (R&D)
Washington, DC 20310

1 Cdr, Harry Diamond Laboratories
Attn: Library
2800 Powder Mill Road
Adelphi, MD 20783

1 Harry Diamond Laboratories, Dept of Army
Attn: DRXDO-RCB (Dr. J. Nemarich)
2800 Powder Mill Road
Adelphi, MD 20783

2 Commander
US Army Satellite Communications Agcy
Attn: DRCPM-SC-3
Fort Monmouth, NJ 07703

1 Cdr, US Army Research Office
Attn: DRXRO-IP
PO Box 12211
Research Triangle Park, NC 27709

1 Cdr, US Army Research Office
Attn: DRXRO-PH (Dr. J. Lontz)
PO Box 12211
Research Triangle Park, NC 27709

1 Chief
Ofc of Missile Electronic Warfare
Electronic Warfare Lab, ECOM
White Sands Missile Range, NM 88002

Commander
US Army Electronics Command
Fort Monmouth, NJ 07703

1 DRSEL-TL-B (I. Reingold)
1 DRSEL-TL-DT
67 DRSEL-TL-BM (A. Gottfried)
1 DRSEL-TL-BM (Ofc of Record)
2 DRSEL-MS-TI
1 DRSEL-GG-TD

2 MIT - Lincoln Laboratory
Attn: Library (R A-082)
PO Box 73
Lexington, MA 02173

1 NASA Scientific & Tech Info Facility
Baltimore/Washington Intl Airport
PO Box 8757, MD 21240

2 Advisory Group on Electron Devices
201 Varick Street, 9th Floor
New York, NY 10014

1 Watkins Johnson Company
3333 Hillview Ave
Attn: Dr. D. Bates
Palo Alto, CA 94304

1 Varian Associates
611 Hansen Way
Attn: Mr. B. Silver
Palo Alto, CA 94303

1 Litton Industries
Electron Tube Division
960 Industrial Road
Attn: Mr. W. Linn
San Carlos, CA 94070

1 Northrop Corporation
175 West Oakton Street
Attn: Dr. O. Doehler
Des Plaines, IL 60016

1 Raytheon Company
Microwave and Power Tube Div.
Foundry Ave
Attn: Larry Clampitt
Waltham, MA 02154

1 ITT Electron Tube Division
PO Box 100
Attn: Mr. R. Wertman
Easton, PA 18042

1 Teledyne-MEC
3165 Porter Drive
Attn: Mr. N. Pond
Palo Alto, CA 94304

1 Microwave Associates, Inc.
Attn: Dr. J. Saloom
Burlington, MA 01803

1 Hughes Aircraft Company
Electron Dynamics Division
3100 West Lomita Blvd
Attn: Dr. A. Lavik
Torrance, CA 90509